SATELLITE CONSTRAINTS ON SOURCE-SPECIFIC NITROGEN OXIDE EMISSIONS AND ISOPRENE CHEMISTRY IN THE SOUTHEAST UNITED STATES: EVALUATIONS AND IMPLICATIONS FOR BACKGROUND OZONE

A Dissertation
Presented to
The Academic Faculty

by

Qiyang Yan

In Partial Fulfillment
of the Requirements for the Degree
Doctor of Philosophy in the
School of Earth and Atmospheric Sciences

Georgia Institute of Technology
August 2021

SATELLITE CONSTRAINTS ON SOURCE-SPECIFIC NITROGEN OXIDE EMISSIONS AND ISOPRENE CHEMISTRY IN THE SOUTHEAST UNITED STATES: EVALUATION AND IMPLICATIONS FOR BACKGROUND OZONE ESTIMATION

Approved by:

Dr. Yuhang Wang, Advisor
School of Earth and Atmospheric Sciences
Georgia Institute of Technology

Dr. Rodney Weber
School of Earth and Atmospheric Sciences
Georgia Institute of Technology

Dr. Greg Huey
School of Earth and Atmospheric Sciences
Georgia Institute of Technology

Dr. Folkert Boersma
Wageningen University
Royal Netherlands Meteorological Institute

Dr. Nga Lee Ng
School of Earth and Atmospheric Sciences
School of Chemical and Biomolecular Engineering
Georgia Institute of Technology

Date Approved: July 21, 2021

To my parents, Apollo and my friends

ACKNOWLEDGEMENTS

Foremost, I would like to express my sincere thanks to my advisor, Dr. Yuhang Wang, for the continuous support of my Ph.D. study and research, and for his patient guidance. His enthusiasm and rigorous attitude to science deeply inspired me. I also appreciate my Ph.D. thesis committee members: Dr. Greg Huey, Dr. Nga Lee Ng, Dr. Rodney Weber, and Dr. Folkert Boersma for their review of my thesis and helpful suggestions.

I am grateful to all the current members and alumni of Dr. Yuhang Wang's group for their devotion to the development of REAM, help on my study and daily life, and the happiness and vitality they bring to this group. I enjoy working with Dr. Yufei Zou, Dr. Ziming Ke, Dr. Yongjia Song, Dr. Ye Cheng, Dr. Ruixiong Zhang, Dr. Jianfeng Li, Dr. Aoxing Zhang, Dr. Hang Qu, Kezhen Chong, Shengjun Xi and Fanghe Zhao. Thanks also go to science teams of the OMI, the SOAS and SENEX observations, which are the important foundation of my studies. Special thanks to Dr. Folkert Boersma for reception and guidance during my KNMI visit.

My gratitude also goes to all my cherished friends for their kind help and all the happy time I shared with them throughout this Ph.D. journey of my life. Finally, I would sincerely appreciate the unconditional love and support from my parents and all other family members.

TABLE OF CONTENTS

LIST OF TABLES

LIST OF FIGURES

LIST OF SYMBOLS AND ABBREVIATIONS

Symbols

$C_5H_9NO_4$	β-isomer isoprene hydroxy nitrate
CO	carbon monoxide
CO_{anthro}	carbon monoxide produced from anthropogenic emissions
CO_{back}	carbon monoxide produced from background
CO_{bio}	carbon monoxide produced from biogenic emissions
E	Emissions
E_A	nitrogen oxides emissions of aircraft
E_E	nitrogen oxides emissions of electric generating unit
E_I	nitrogen oxides emissions of industry
E_L	nitrogen oxides emissions of lightning
E_{NON}	nitrogen oxides emissions of nonroad
E_{OG}	nitrogen oxides emissions of Oil & Gas
E_{ON}	nitrogen oxides emissions of onroad
E_S	nitrogen oxides emissions of soil
ETHLN	ethanal nitrate
HCHO/CH_2O	formaldehyde
$HCHO_{anthro}$	formaldehyde produced from anthropogenic emissions
$HCHO_{back}$	formaldehyde produced from background
$HCHO_{bio}$	formaldehyde produced from biogenic emissions
HNO_3	nitric acid
HO_2	hydroperoxyl radical

INs	isoprene nitrates
K_{zz}	eddy diffusivity coefficients
MACR	methacrolein
MACRN	methacrolein nitrate
MVK	methylvinylketone
MVKN	methylvinylketone nitrate
N_2O_5	dinitrogen pentoxide
NO	nitric oxide
NO_2	nitrogen dioxide
NO_3	nitrate radical
NO_x	nitrogen oxides
NO_y	active nitrogen compounds
NO_z	non-NO_x active nitrogen compounds
O_3	ozone
$O_{3anthro}$	ozone produced from anthropogenic emissions
O_{3back}	ozone produced from background
O_{3bio}	ozone produced from biogenic emissions
OH	hydroxyl radical
PAN	peroxyacetyl nitrates
pINs	particle-phase isoprene nitrates
PROPNN	propanone nitrate
γ	aerosol uptake coefficients
τ	lifetime
Ω	vertical column densities
Ω_{sat}	Satellite nitrogen dioxide vertical column densities

Ω_{E_A}	Modeled nitrogen dioxide vertical column densities of aircraft
Ω_{E_E}	Modeled nitrogen dioxide vertical column densities of electric generating unit
Ω_{E_I}	Modeled nitrogen dioxide vertical column densities of industry
Ω_{E_L}	Modeled nitrogen dioxide vertical column densities of nonroad
$\Omega_{E_{NON}}$	Modeled nitrogen dioxide vertical column densities of nonroad
$\Omega_{E_{OG}}$	Modeled nitrogen dioxide vertical column densities of Oil & Gas
$\Omega_{E_{ON}}$	Modeled nitrogen dioxide vertical column densities of onroad
Ω_{E_S}	Modeled nitrogen dioxide vertical column densities of soil

Abbreviations

AMF	Air mass factor
AQS	Air Quality System
ARA	Atmospheric Research and Analysis
BDSNP	The Berkley Dalhousie Soil NO Parameterization
BVOCs	biogenic volatile organic compounds
CEMs	continuous emission monitors
CFSR	Climate Forecast System Reanalysis
CG	cloud-to-ground lightning
CIMS	chemical ionization mass spectrometry
CIT-ToF-CIMS	Caltech CF_3O^- Time-of-Flight Chemical Ionization Mass Spectrometer
CONUS	contiguous United States
CTM	Chemical transport model

CTR	Centreville site, Alabama
DI	Daily Inversion
DISCOVER-AQ	Deriving Information on Surface conditions from Column and Vertically Resolved Observations Relevant to Air Quality
DRI	Daily Retrieval-Inversion
EGU	electric generating unit
EPA	Environmental Protection Agency
FIGAERO	filter inlet for gases and aerosols
GC-MS	gas chromatography coupled with mass spectrometry
GOME	Global Ozone Monitoring Instrument
GOME-2	Global Ozone Monitoring Instrument-2
HR-ToF-CIMS	high-resolution chemical ionization time-of-flight mass spectrometer
IC	intra-cloud lightning
JJA	June, July, and August
KNMI	Royal Dutch Meteorological Institute
MB	Mean bias
MDA8	Maximum daily 8-hour average ozone mixing ratio
ME	Mean error
MEGAN	the Model of Emissions of Gases and Aerosols from Nature
MI	Monthly inversion
Mini-CIM	a mini Caltech isoprene mechanism
MOBILE6	Mobile Source Emission Factor Model
MOVES	Motor Vehicle Emissions Simulator
NA	North America
NAAQS	National Ambient Air Quality Standards

NAQFC	the National Air Quality Forecast Capability
NARSTO	The North American Research Strategy for Tropospheric Ozone
NEI	National Emission Inventory
NLDN	National Lightning Detection Network
NMB	normalized mean bias
NME	normalized mean error
NOAA	the National Oceanic and Atmospheric Administration
OMI	Ozone Monitoring Instrument
OPE	ozone production efficiency
PRB	Policy Relevant Background
PROPHET	PHotochemistry, Emissions, and Transport summer 1998 measurements
PTR-ToF-MS	proton-transfer-reaction time-of flight mass spectrometer
QA4ECV	Quality Assurance for Essential Climate Variables
REAM	Regional chEmical trAnsport Model
RMSE	root mean square error
RTM	radiative transfer models
SAS	the Southeast Atmosphere Study
SCD	slant column density
SCIAMACHY	SCanning Imaging Absorption spectroMeter for Atmospheric CHartographY
SEARCH	the SouthEastern Aerosol Research and Characterization
SENEX	Southeast Nexus
SMOKE	Sparse Matrix Operator Kernel Emission
SOA	Secondary organic aerosol
SOAS	Southern Oxidants and Aerosols Study

SSREAM	a source-specific Regional chEmical trAnsport Model
TM5	the Tracer Model, version 5
TROPOMI	TROPospheric Monitoring Instrument
USB	U.S. background
VCD	vertical column density
WRF	the Weather Research and Forecasting model
3SDRI	a 3-stage daily retrieval-inversion

SUMMARY

Nitrogen oxides (NO_x = NO + NO_2) originating from combustion, lightning and soil, are the main drivers of the tropospheric ozone formation and important precursors of secondary organic aerosols, with consequences for human health and climate. Isoprene, the most important biogenic volatile organic compounds (BVOCs) globally, accounts for about half of the BVOC emissions (~ 500 Tg yr^{-1}). Its rapid oxidation in the presence of NO_x is a main driver of the atmospheric chemistry. Detailed and accurate estimations of NO_x emissions and better understanding of isoprene chemistry are essential for the development of emission and air pollution control policies. This dissertation employs regional modeling and various observation analysis to extensively evaluate the NO_x emissions from varied anthropogenic and biogenic sources, explore the nighttime decay of isoprene and isoprene chemical mechanism at a rural site, and investigate the implications for the background ozone in the Southeast United States.

Inverse-modeling of NO_x emissions using information from both model simulations and satellite observations can improve the uncertainties in traditional bottom-up emission inventories. Previous studies mainly focus on the estimations of total NO_x emissions with several attempts to partition the anthropogenic emission from natural NO_x sources without constraining lightning NO_x. To understand the detailed NO_x emissions, we construct a source-specific Regional chEmical trAnsport Model (REAM) model and developed a 3-stage daily retrieval-inversion (3SDRI) method to inversely derive the NO_x emissions from onroad, nonroad, electric generating unit (EGU), industry, Oil & Gas, aircraft, soil and lightning sources using the OMI measurements in summer 2011 over the

West, Central and East contiguous United States (CONUS). We find that the assimilated total posterior NO_x emissions are 5.02 Tg N/a in total consistent with 5.00 Tg N/a of the prior NAQFC emissions, while improved simulations of NO_2 columns compared to OMI observations after using the 3SDRI method indicate biases in the source distributions of NO_x emissions. Analysis of the modeling results show that the prior emissions tend to underestimate natural NO_x emissions and overestimate anthropogenic sources, especially onroad emissions, over the CONUS. Natural emissions have large impacts on NO_2 columns and are predicted to comprise 30%-60% of the tropospheric NO_2 columns in summer 2011. The nonlinear relationships between vertical NO_2 columns and NO_x emissions for specific emission sources are consistent at different emission levels. We also find that the updated source-specific NO_x emission distributions have small impacts on the MDA8 ozone with 1-3 ppb decrease over the West and Central and the general increase over the East. These findings implicate better estimations of the source-specific NO_x emission distributions largely improve the modeled NO_2 columns and have a relatively small impact on MDA8 ozone simulations.

Isoprene emission is highly light- and temperature-dependent with almost no emission at night. Generally, isoprene follows a marked diurnal pattern of a steady increase throughout the morning and decrease in the afternoon due to reduced emissions and rapid oxidation of OH. Many field studies observed an accumulation of isoprene in the early evening with a decline after sunset in the high NO_x impact environment and credited this nocturnal decline of isoprene to nitrate radicals (NO_3) oxidation. Isoprene observed at the 2013 SOAS Centreville site (CTR) in Alabama, which is a rural site with substantial isoprene emissions and minor impact from anthropogenic pollution, show continuous

nighttime decay. The diurnal profile of isoprene is a function of emissions, chemistry, advection, and vertical mixing. We use the REAM to investigate the nocturnal decline of isoprene and oxidation products of isoprene to make implications on current isoprene chemistry mechanism in the model. Using the 3-D REAM, we reasonably reproduce the diurnal profile of isoprene evaluated by the SOAS measurements and investigate the contribution of chemical (OH, O_3 an NO_3 oxidation) and transport processes (advection, vertical mixing) to the isoprene levels at night. We find that about half of the nighttime isoprene are lost by transport at Centreville and increase isoprene levels downwind Centreville. Ozonolysis dominates nighttime chemical processes, consuming 24.4% of isoprene overnight, over OH and NO_3 oxidation, while NO_3 oxidation merely accounts for 12.2% of total nighttime isoprene loss, comparable to OH oxidation. The ratio of first oxidation products of isoprene, MVK and MACR, further supports the nighttime transport impact. The missing peaks of modeled MVK and MACR in the late afternoon, coinciding with the missing peaks in the diurnal profiles of isoprene nitrates (ISOPN1 and MVKN+MACRN), indicate that the unclarified isoprene oxidation processes in the model mechanism during the transition period from OH-driven to O_3-driven isoprene mechanism. Modeled pINs generally reproduce the diurnal variation of the SOAS Centreville observations but have issues with late afternoon peak and early morning peak, in part related to homogeneous uptake coefficients and bulk lifetime assumed in the model. Better model mechanism of isoprene oxidation from OH-driven to O_3-driven transition period and elucidation of formation and loss of pINs are needed in the model.

Isoprene emissions contribute largely to ozone levels in the Southeast United States. The observed robust linear relationships of O_3-CO-HCHO have been found during

DISCOVER-AQ 2011 experiment, providing a fast-response estimator of surface ozone based on CO and HCHO concentrations in the Southeast. Background ozone is not affected by emissions of ozone precursors in a region and is transported from distant troposphere or the stratosphere. It is an important factor to be considered in regional ozone control policies. We applied the O_3-CO-HCHO relationships to term the clean-background ozone as the portion of ozone that does not have chemical signatures, namely show ozone production from anthropogenic or natural emissions of ozone precursors. We conduct the tagged-tracer REAM simulations and make extensive use of the aircraft (SENEX) and surface (SOAS) observations in the summer 2013 to investigate the background ozone contributions in the Southeast. We also compare to previous background ozone estimation approaches, including O_3-NO_z, zero-emission and 5^{th} percentile method. The most consistent of background ozone in the O_3-CO-HCHO method using observation and model data has been found, but about 4-50% lower than the other methods. Using this new O_3-CO-HCHO method, we find that the summertime background ozone at the surface is in the range of 10-15 ppbv in the inland areas of the Southeast, lower than previous studies. This background ozone tends to increase from urban centers to rural regions and from the surface to higher altitude due to changing ozone lifetime driven by surface emissions and dry deposition to the surface. The better quantitative estimates of background ozone using the O_3-CO-HCHO method provide further incentives to control anthropogenic emissions in ozone nonattainment areas of the Southeast.

CHAPTER 1. INTRODUCTION

1.1 Statement of the Problem

Tropospheric ozone is harmful to human health and vegetation (Logan et al., 1981; Wang and Jacob, 1998; Wang et al., 1998; Lelieveld and Dentener, 2000). As a secondary pollutant, tropospheric ozone production involves reactions between precursors NO_x and volatile organic compounds (VOC). Due to continuous anthropogenic emission reduction in the past decade, ozone concentrations decrease significantly in the U.S. and many urban areas are transitioning to NO_x-sensitive chemical regimes (Tong et al., 2015; Jin et al. 2017). In 2015, the Environmental Protection Agency (EPA) improved the air quality standard of O_3 from 75 ppb in 2008 to 70 ppb to provide requisite protection of public health and welfare (EPA 2015) in the United States. Under such stringent standard, a good understanding of emission sources, chemistry and physics involving O_3 production and background ozone contributions provide important piece of information to promote efficient emission control strategies.

In this dissertation, I focus on three relevant aspects: (1) source-specific NO_x emissions in the West, Central and East United States, (2) isoprene chemistry at a rural site and (3) background ozone levels in the Southeast United States using the 3-D REAM and various observation data. In the first topic, I investigate the accuracy of regional source-specific emission estimations, with a focus on differentiate anthropogenic and biogenic contributions to NO_x emissions. Then, I explore the chemical and physical processes of nocturnal isoprene and isoprene oxidation products to explore the accuracy of current

isoprene chemical mechanism. In the last topic, I evaluate the estimation of the background ozone, which provides some insights to the development of air pollution control policies.

1.1.1 Source-specific NO_x emissions

Nitrogen oxides play a key role in the photochemical production of tropospheric ozone and formation of SOA (Travis et al., 2016; Xu et al., 2015), directly associated with impacts on the respiratory system (World Health Organization, 2005). In the past decade, NO_x emission has been decreased by more than 40% in the United States (Duncan et al. 2010; Tong et al. 2015; Krotkov et al. 2016). Many urban areas in the U.S. are transitioning to NO_x-sensitive chemical regimes (Tong et al., 2015; Jin et al. 2017). The National Emissions Inventory (NEI) provides a comprehensive and detailed estimates of NO_x emissions from all types of sources, which is released every three years based primarily upon data provided by State, Local, and Tribal air agencies by the U.S. EPA (EPA, 2015). These are the traditional bottom-up emission inventories, which rely on activity levels and emission factors estimated by province and sector and then aggregated to the national level, and therefore, are subject to large uncertainties (Streets et al., 2003). Previous studies show that 2011 NEI emission inventory is biased high by over 50%, especially in mobile sectors (Anderson et al. 2014; Canty et al. 2015; Liu et al. 2015; Travis et al. 2016).

As an alternative to traditional bottom-up emission inventories, satellite measurements of nitrogen dioxide (NO_2) from multiple instruments, including the Global Ozone Monitoring Experiment (GOME), Scanning Imaging Absorption Spectrometer for Atmospheric Chartography (SCIAMACHY), GOME-2, Ozone Monitoring Instrument (OMI) and TROPospheric Monitoring Instrument (TROPOMI), have been widely used to

derive a top-down NO_x emission inventories (Jaeglé et al., 2005; Stavrakou et al., 2008; Lin and McElroy, 2010; Lamsal et al., 2011; Castellanos and Boersma, 2012; Duncan et al., 2016; Lorente et al., 2019).

Inverse-modeling of NO_x emissions combines model simulations with satellite observations to reduce the uncertainties in traditional bottom-up emission inventories. Martin et al. (2003) first developed the monthly inversion method by assuming a linear relationship between bottom-up emissions and top-down NO_2 columns from GOME. Zhao and Wang (2009) improved this method by conducting inversion iteratively on a daily basis, which reduces the error from the nonlinear chemistry. Gu et al. (2014) further improved this method by including satellite retrieved NO_2 columns in inverse modeling. Biases introduced from inconsistency between NO_2 profiles in the retrieval and from the inverse modeling are removed in their method. Then, Gu et al. (2016) improved the inversion method by considering the chemical non-linearity and taking the local derivative of bottom-up emissions to the columns instead of directly taking the ratio of bottom-up emissions to the columns. However, all these methods only considered the total NO_x emissions.

Several studies have attempted to partition the anthropogenic NO_x emissions from natural sources, based on satellite retrievals without constraining lightning NO_x. Jaeglé et al. (2005) assumed that if the priori anthropogenic emission exceeds 90% of the total prior emission, the posterior emission without lightning is only anthropogenic. Otherwise, the difference between the posterior and prior emissions are from fire and soil sources. Using satellite observations of fire events, they could further distinguish fire and soil emissions. They partitioned the global NO_x sources and found that the errors of the posterior

anthropogenic emissions are reduced by factor of two. Similarly, Wang et al. (2007) tried to separate combustion emissions from soil NO_x over the eastern China. They assumed that the prior anthropogenic emissions have an error range of 40% to 60%. If the posterior emissions are within this range, adjustment will only be conducted to anthropogenic emissions. Otherwise, only soil NO_x emissions will be updated. Both methods ignored the impact of lightning NO_x. It is estimated that lightning NO_x could contribute 10-15% of total NO_x emissions globally (Schumann and Huntrieser, 2007). Pickering et al. (2016) attempted to use air mass factor (AMF) to partition lightning NO_x in the United States. The determination of background lightning NO_x and AMF of lightning is very sensitive to spatial and temporal variation. Understanding regional emission sources are hereby important. We construct a source-specific REAM (SSREAM) and conduct daily inversion on eight NO_x emission sectors to investigate the accuracy and contributions of each sector in the West, Central and East United States in CHAPTER 2.

1.1.2 Nocturnal decline of isoprene

Biogenic volatile organic compounds (BVOCs) are about eight times more emitted to the atmosphere compared to anthropogenic sources, significantly impacting atmospheric photochemistry (Guenther et al., 2012). Isoprene accounts for half of the total BVOCs emissions. Isoprene emission has a pronounced diurnal cycle, peaking at noon and declining to zero at night (Sharkey, 1995). Isoprene reacts rapidly with atmospheric oxidants during the day, especially the hydroxyl radical (OH), producing hydroxyperoxy radicals that can oxidize NO to NO_2 and hence drive O_3 production and nitrates formation (Sillman et al., 1990). At night, Nitrate radical (NO_3) is generated by NO_2 reacting with O_3, but undergoes rapid photolysis when sunlight comes in. The fast reaction between

isoprene and NO_3 (τ = 20 min at [NO_3] = 50 ppt) leads to the formation of various multifunctional nitrates (Atkinson et al., 2006). These isoprene nitrates can form secondary organic aerosols and serve as a reservoir of NO_x at night, which can be transported to downwind cities and release NO_x back when sunlight comes in, impacting on next day morning O_3 concentration. The dominant sources of surface NO_x are anthropogenic emissions (NEI 2014). The isoprene chemistry therefore is an important linkage between biogenic and anthropogenic emissions and have important consequences of ozone pollution (Trainer et al., 1987), transport and fates of nitrogen species (Horowitz et al., 2007; Mao et al., 2013; Xiong et al., 2015; Fisher et al., 2016) and formation of SOA (Xu et al., 2015; Lee et al., 2016).

Many field studies observed an accumulation of isoprene in the early evening with a decline after sunset and some production of organic nitrates at night (Starn et al., 1998; Hurst et al., 2001; Stroud et al., 2002). Previous studies credited this nighttime decay of isoprene to NO_3 oxidation in regions with high NO_x emission impacts (Starn et al., 1998; Brown et al., 2009; Millet et al., 2016). Most isoprene is oxidized during daytime by OH. Isoprene that is emitted in late afternoon, when OH concentrations are dropping, can persist into evening. Ozonolysis of isoprene is relatively slow (τ = 30 hr at [O_3] = 30 ppb) compared with NO_3 oxidation (τ = 20 min at [NO_3] = 50 ppt) at night (Atkinson et al., 2006). Nighttime OH radical concentrations are low. NO_3, on the other hand, can be abundant at night.

Other studies gave alternative explanations for nocturnal decay of isoprene if there is low NO_x impact over forest regions with high isoprene emissions (Makar et al., 1999; Hurst et al., 2001; Sillman et al., 2002). When emissions of isoprene are shut down after

sunset, high isoprene concentrations at surface could be vertically dispersed to higher levels (Makar et al., 1999). High nighttime OH were observed at the PROPHET site and explained a significant part of the observed decrease in isoprene at night (Hurst et al., 2001). Another possible explanation is that fresh air is gradually advected in when there is no newly emitted isoprene and cause a steady decrease of isoprene (Sillman et al., 2002).

Our study is conducted at Centreville, Alabama, a rural region during the 2013 SOAS campaign. We use the REAM to quantify the chemical and physical processes of nighttime isoprene at this site constrained by Southern Oxidants and Aerosols Study (SOAS) observations at Centreville. We explore the oxidation products of isoprene and gas and particle phase of isoprene nitrates and make implications on current modeled isoprene chemistry and SOA formation mechanism in CHAPTER 3.

1.1.3 Clean-Background ozone

The existence of a background level of ozone in the atmosphere is well established. Quantifying surface background ozone can serve to define a lower bound of O_3 concentrations with respect to reductions of anthropogenic emissions (Fiore et al., 2002). In 2015, EPA further lowers the NAAQS eight-hour averaged ozone from 75 ppb to a more stringent standard 70 ppb to better protect human welfare and ecosystem. The implementation of this new standard will emphasize of the importance of putting forward effective emission control strategy. In the past decade, the peak ozone values have been decreased in most of the United States due to the control of the anthropogenic emissions of NO_x and VOCs (Cooper et al., 2012; Simon et al., 2015). The regulations of local ozone levels are complicated by the existance of significant background ozone concentrations

(Jaffe et al., 2018). Better determination of background ozone makes important implications for the ozone rulemaking process and risk estimates (EPA, 2007a).

Background ozone estimates from observations of remote monitoring sites on "clean" days are for what Cooper et al. (2012) termed "baseline" ozone. It contains the part of the noncontrollable ozone from such as stratosphere-troposphere exchange, transport of nondomestic pollution, photochemical production from natural NO_x and VOC emissions, wildfires and lightning, but could also include upwind and recirculated ozone produced from U.S. anthropogenic emissions (Oltmans et al., 2008). The "baseline" ozone, therefore, is higher than the background ozone. Other studies tried to derive the background ozone based on the observed relationships of ozone and NO_z (defined as total reactive nitrogen (NO_y)-NO_x ($NO+NO_2$)), where the regression slopes are used to study ozone production efficiency (OPE). They defined a background ozone by extrapolating the O_3-NO_z linear regression line to the 0-value point of NO_z value (hereafter referred to as the O_3-NO_z method) (Hirsch et al., 1996; Altshuller and Lefohn, 1996; Ninneman et al., 2019). However, the background values estimated from O_3-NO_z method could be biased from mixing, fresh emissions and HNO_3 deposition (Fiore et al., 2002).

Fiore et al. (2003) first put forward the zero-emission method in the frame of model simulations to define a Policy Relevant Background (PRB) ozone (EPA 2006). Specifically, the PRB is surface ozone concentration in absence of anthropogenic emissions across the North America (NA). Similarly, some term U.S. background (USB) ozone as the ozone produced from countries outside the U.S. (Emery et al., 2012; Dolwick et al., 2015). It comprises contributions from anthropogenic emissions outside of NA/U.S. and natural sources, including biogenic NO_x, stratosphere-troposphere exchange, lightning,

etc. Higher model resolution and different regional and global models have been used in later studies to improve the simulation results (Zhang et al. 2011; Lin et al., 2012; Emery et al., 2012; Lefohn et al., 2014; Dolwick et al., 2015). The important underlying issue with the zero-emission method by setting NA/U.S. anthropogenic emissions to zero in model simulations is that the OPE has been changed, causing non-linear chemical contributions from different sectors and regions (Wu et al., 2009).

We follow Cheng's method (Cheng et al., 2018), which can take both the advantage of observations and model simulations to achieve a better estimation of background ozone. Here, we define a clean-background ozone as the portion of ozone that does not produced from anthropogenic emissions or anthropogenic interaction with biogenic emissions of ozone precursors. It is more objective and more easily intercomparable, which considers the chemical nonlinearity of ozone chemistry and excludes the influence from upwind city emission that would vary with time and location in the region. In this method, we utilize the robust linear regression relationships of observed O_3-HCHO, O_3-CO, and CO-HCHO in the Southeast United States to separate total ozone into three parts, anthropogenic, anthropogenic-biogenic (anthropogenic emission interacting with biogenic emissions) and background ozone (hereafter referred to as the O_3-CO-HCHO method) (Cheng et al, 2017; 2018). We show the results of background ozone inferred from SOAS and SENEX campaign and tagged-tracer REAM simulations, and intercomparisons with other methods in the CHAPTER 5.

1.2 Description of 3-D REAM

REAM is a 3-D regional model which has been evaluated in a number of tropospheric chemistry and transport studies in the United States and China (e.g., Choi et al., 2005, 2008a, b; Zeng et al., 2003; Zhao and Wang et al., 2009; Zhao et al., 2009, 2010; Liu et al., 2010, 2012a, 2012b;2014; Gu et al., 2013, 2014, 2016; Zhang et al., 2016, 2017; Li et al., 2019a, b; Qu et al., 2020). The REAM has a horizontal resolution is 36 × 36 km^2, with 30 vertical layers in the troposphere. The model is driven by assimilated meteorological fields from a Weather Research and Forecasting (WRF) simulation constrained by the Climate Forecast System Reanalysis products (https://cfs.ncep.noaa.gov/cfsr/). The chemistry mechanism is adopted from the GEOS-Chem (v12.8.0) with updated isoprene nitrate uptake on aerosols (Fisher et al., 2016; Bates et al., 2019). Anthropogenic emissions used in the model are from the 2011 National Emission Inventories. Biogenic emissions are calculated with the Model of Emissions of Gases and Aerosols from Nature (MEGAN) version 2.10 (Guenther et al., 2012). The lateral boundary conditions are taken from a 2° × 2.5° GEOS-Chem model (v11.01) simulation (Bey et al., 2001; Henderson et al., 2014).

1.3 Scope of this work

This dissertation (1) improves the estimation of NO_x emissions from six anthropogenic, soil and lightning sources over the Western, Central and Eastern United States; (2) investigates the nocturnal isoprene at Centreville during the 2013 SOAS campaign; and (3) identifies the background ozone levels using O_3-CO-HCHO relationships in the Southeast United States. The rest of this dissertation is organized as follows.

CHAPTER 2, "Satellite constraint source-specific nitrogen oxide emissions over the West, Central and East contiguous United States", constructs a source-specific REAM and applies the 3SDRI method to derive NO_x emissions from onroad, nonroad, electric generating unit (EGU), industry, Oil & Gas, aircraft, soil and lightning sectors constraint by OMI NO_2 measurements in June, July and August 2011. The total posterior emissions of NO_x over CONUS are estimated to be 5.02 Tg N/a in consistent with the total prior emissions of 5.00 Tg N/a. Better matches of NO_2 VCDs between satellite observations and model simulations using the 3SDRI method are achieved. This result implicates that EPA has a good estimation of total NO_x emissions, but the source distributions are biased. The nonlinear relationships between vertical NO_2 columns and NO_x emissions for specific emission sources are consistent at different emission levels. After applying the posterior emissions in the model, we find no significant changes of the simulated MDA8 ozone, indicating better distribution of NO_x emissions have small impacts on MDA8 ozone levels.

CHAPTER 3, "Nocturnal decay of isoprene during the 2013 Southern Oxidant and Aerosol Study (SOAS): evaluation and implications", investigates the physical and chemical processes of nocturnal isoprene at a rural site Centreville during the 2013 SOAS campaign. The observed averaged nighttime isoprene concentration during the campaign shows continuously decrease. Our model simulations show that the physical processes related to transport contribute more than half of the total loss, with approximately equal impacts from advection and vertical mixing. Ozonolysis dominates nighttime chemical processes over OH and NO_3 oxidation, consuming about 0.6 ppb of isoprene overnight, while NO_3 oxidation only accounts for 12.2% of nighttime isoprene loss. We examined the

oxidation products of isoprene and both the gas and particle phase isoprene nitrates. It provides important implications for the current modeled isoprene chemistry and SOA formation mechanism.

CHAPTER 4, "Lower than expected summertime clean-background ozone concentrations derived from ozone precursor relationships in the Southeast United States", estimates a clean-background ozone concentration of 10-15 ppbv in the Southeast United States using the O_3-CO-HCHO method based on the 2013 SOAS ground observations at Centreville, 2013 SENEX aircraft measurements and tagged-tracer REAM simulations. We find consistent background ozone levels using model and observation data. We also compare with methods adopted in previous studies, including O_3-NO_z, zero-emission and 5^{th} percentile method. Background ozone values using previous methods show 4-50% higher estimates compared to our O_3-CO-HCHO method. This background ozone tends to increase from urban centers to rural regions and from the surface to higher altitude due to changing ozone lifetime driven by surface emissions and dry deposition to the surface. It implicates the importance of further anthropogenic emissions control in ozone nonattainment areas of the Southeast.

CHAPTER 5, "Conclusion and Future Work", summarizes the findings in CHAPTER 2-4 and gives recommendations for future work.

CHAPTER 2. SATELLITE CONSTRAINTS ON SOURCE-SPECIFIC NITROGEN OXIDE EMISSIONS OVER THE WEST, CENTRAL AND EAST CONTIGUOUS UNITED STATES

2.1 Introduction

Nitrogen oxides (NO_x = NO + NO_2) is crucial for photochemical production of tropospheric ozone and secondary pollutants (Xu et al., 2015; Travis et al, 2016). Elevated ozone levels at surface pose threats to human health and ecosystem (Fowler et al., 2009; Monks et al., 2015). Transportation, industry, power plants, oil and gas (Oil & Gas), soil and lightning are major emission sources of NO_x. Transportation contributes the most anthropogenic NO_x emissions in the U.S, more than 50%, followed by power plants, industry and Oil & Gas (EPA 2015). Biogenic emissions, such as soil and lightning NO_x, are extremely uncertain and variant with time and location but are important in model simulations (Yienger et al., 1995; Allen et al., 2012; Vinken et al., 2014; Luo et al., 2017). In the past decade, NO_x emissions have been decreased by more than 40% in the U.S. as a result of emission regulations and technology improvements (Duncan et al., 2010; Russell et al., 2012; Tong et al., 015; Krotkov et al., 2016). Many urban areas are transitioning to NO_x-sensitive chemical regimes (Tong et al., 015; Krotkov et al., 2016; Jin et al., 2020). Understanding the contributions of different NO_x sources are fundamental to the development of cost-effective emission control policies and ozone regulations.

Satellite measurements of tropospheric NO_2 from different instruments, such as Global Ozone Monitoring Experiment (GOME), Scanning Imaging Absorption

Spectrometer for Atmospheric Chartography (SCIAMACHY), Ozone Monitoring Instrument (OMI) and GOME-2 have been extensively used to derive a top-down NO_x emission inventories as a complement to traditional bottom-up estimation of emissions (Martin et al., 2003; Jaeglé et al., 2005; Stavrakou et al., 2008; Lin et al., 2010; Lamsal et al., 2011; Gu et al., 2014; Qu et al., 2017; Souri et al., 2016, 2017; Mijling et al., 2017). Inverse modeling of NO_x emissions combines model simulations with satellite observations. Martin et al. (2003) first developed the monthly inversion method by assuming a linear relationship between bottom-up emissions and top-down NO_2 vertical columns and estimated NO_x emissions using the linearly derived "bulk ratio". Zhao and Wang (2009) improved this method by conducting inversion on a daily basis to reduce chemical non-linearity errors. Gu et al. (2014) further included modeled NO_2 profiles in satellite retrieval reconciling the difference of inverse modeling and satellite observations. Nonlinear chemical feedbacks between OH and NO_x can lead to biases in the "bulk ratio" method, especially in high NO_x emission regions. Gu et al. (2016) accounted the chemical non-linearity by taking the local derivative of bottom-up emissions to NO_2 columns. However, only total NO_x emissions are considered in the above methods. Given the varied spatial and temporal contributions of different NO_x sources, other studies attempted to quantitatively estimate each NO_x source.

Several attempts have been made to partition NO_x emissions into anthropogenic and natural sources based on satellite observations (Jaeglé et al., 2005; Zhao and Wang, 2009; Wang et al., 2007). Jaeglé et al. (2005) distinguished emissions from soil, biomass burning, and fuel combustion using multiple assumptions and constraints from satellite observations of fire events and found an underestimation in modeled soil emissions

globally. Zhao and Wang (2009) applied a linear partition approach to the posterior emissions based on the ratio of the prior fossil fuel and soil NO_x emissions in China. Because of the high spatial and temporal variations of lightning NO_x emissions, most inversion studies did not constrain lightning NO_x (Jaeglé et al., 2005; Zhao and Wang, 2009; Wang et al., 2007). It is estimated that lightning NO_x could contribute 10-15% of total NO_x emissions globally (Schumann and Huntrieser, 2007). Stavrakou et al. (2008) found that the global posterior NO_x emissions from lightning increase by 50-80% concerning the prior in consistent with Boersma et al. (2005) and Schumann and Huntrleser (2007). Pickering et al. (2016) attempted to use air mass factor (AMF) to estimate lightning NO_x over the Gulf of Mexico with pixels of cloud fraction greater than 0.9 and found consistency with previous estimates (Ott et al., 2007; Beirle et al., 2010; Pickering et al., 2016). Previous studies only considered limited NO_x sources with very uncertain assumptions, and some did not constrain lightning NO_x emissions.

In this study, we developed a 3-stage daily retrieval-inversion (3SDRI) method to estimate NO_x emissions of onroad, nonroad, electric generating unit (EGU), industry, Oil & Gas, aircraft, soil and lightning, constraint by the retrieved OMI NO_2 measurements over the West, Central and East contiguous United States (CONUS) for June, July and August (JJA) 2011. We implement the 3SDRI method in the source-specific 3-D Regional chEmistry and transport Model (SSREAM) and examine the posterior emissions of each NO_x source. The modeled NO_2 vertical column densities (VCDs) using 3SDRI method are compared to the modeled NO_2 VCDs with the prior emissions to demonstrate the advantages of the 3SDRI method. We also show detailed contributions of each emission

source over the West, Central and East CONUS to the total NO_2 VCDs and provide insights for regulating source-specific NO_x emissions and air quality control policies.

2.2 Methods and datasets

2.2.1 OMI Tropospheric NO_2 columns

OMI onboard Aura Sun-synchronous polar satellite is a UV/Visible nadir solar backscatter spectrometer, launched in July 2004. It overpasses the equator about 13:30 local time (LT) and achieves a near-global daily coverage with a nadir resolution of 13 km × 24 km (Levelt et al., 2006). OMI has a view of 114° with 2600 km viewing swath and observes solar irradiance and sunlight reflected from the surface of the Earth in the 270-500 nm wavelength range at approximately 0.5 nm resolution. We exclude pixels with cloud radiance fraction exceeding 0.5 and affected by cross-track row anomaly to minimize biases rising from cloud effect and the variable availability of reliable pixels.

We used the Quality Assurance for Essential Climate Variables (QA4ECV) version 1.1 level 2 (L2) OMI NO_2 products in this study (Boersma et al., 2017). In the retrieval process, we estimated the tropospheric NO_2 slant column densities (SCDs) by subtracting global chemical transport model (CTM) TM5 assimilated stratospheric SCDs from the total SCDs (Williams et al., 2017). We derived tropospheric VCDs from tropospheric SCDs divided by AMFs. The tropospheric AMFs are estimated using the prior SSREAM NO_2 profiles, the WRF temperature and pressure profiles (Zhang et al., 2018) and the pre-computed AMF lookup table generated from the radiative transfer models (RTM) (Lorente et al., 2017). AMF calculation is the largest source of uncertainties in NO_2 satellite retrievals (Boersma et al., 2004; Lorente et al., 2017). The AMF structural uncertainty can

be 31% over unpolluted regions and 42% over polluted regions (Lorente et al., 2017). In general, estimated errors in the tropospheric NO_2 vertical columns from the satellite are approximately 30% under clear-sky conditions (Boersma et al., 2011).

2.2.2 The prior source-specific emission inventories

Anthropogenic NO_x emissions we used in the model are from the National Air Quality Forecast Capability (NAQFC) emissions based on assimilation results of 2011 EPA National Emission Inventories (NEI 2011), emission measurements, and trend projections (Tong et al., 2015). NEI 2011 emissions, including national continuous emission monitors (CEMs) data, nonroad inventories and onroad activity data, and point and nonpoint inventories (EPA, 2015), are used as base inventories. The area and mobile emissions are further processed separately using an emission tool called Sparse Matrix Operator Kennel Emission (SMOKE) (Houyoux et al., 2000) to represent hourly data at a 12 km resolution. In this study, we separated NAQFC emissions into six anthropogenic sources (onroad, nonroad, EGU, industry, Oil & Gas and aircraft) as the six anthropogenic prior. We assumed a uniform weekday to weekend ratios for all anthropogenic NO_x sources in consideration of the diurnal cycle following previous studies (Beirle et al., 2003; Boersma et al., 2009; Choi et al., 2012; Kim et al., 2016). NEI 2011 mobile emissions estimated by an early version of the Motor Vehicle Emission Simulator (MOVES) (EPA, 2015) are biased high by at least 50% (Anderson et al., 2014; Canty et al., 2015), here, mobile emissions, including onroad emissions (E_{ON}) and nonroad emissions (E_{NON}), are generated from MOBILE6 using projection factors from the Cross-State Air Pollution Rule (Tong et al., 2015). EGU emissions (E_E) are point sectors. Other non-EGU point sectors and nonpoint emissions associated with industrial and commercial activities are merged as

the industry emissions (E_I). Point Oil & Gas and non-point Oil & Gas emissions are combined into Oil & Gas emissions (E_{OG}). Aircraft emissions (E_A) are estimated based on aircraft activities for all known airports in the U.S. (Hudman et al., 2010).

In this study, we considered two important natural NO_x emission sources including soil emissions (E_S) and lightning emissions (E_L). The Berkley Dalhousie Soil NO Parameterization (BDSNP) scheme is implemented in the model to calculate soil NO_x emissions, which has a continuous dependence on soil moisture and temperature, and a detailed spatial and temporal representation of N-inputs from chemical/manure fertilizer and atmospheric N-deposition (Hudman et al., 2012). E_L are estimated based on observed cloud-to-ground (CG) flashes and intra-cloud (IC) flashes from the National Lightning Detection Network (NLDN) (Orville, 2008). Emissions from biomass burning are not considered due to the extremely small amount (0.01 Tg N/a) compared to lightning (0.90 Tg N/a) and soil (0.76 Tg N/a) NO_x emissions (Hudman et al., 2010).

2.2.3 Uncertainties of eight emission source

The North American Research Strategy for Tropospheric Ozone (NARSTO) emission inventory assessment has given a quantitative estimate of uncertainties for all NO_x sectors. In the U.S., the confidence level of EGU is the highest, followed by onroad (medium high), nonroad(medium), non-EGU point sources (medium), stationary nonpoint sources (low) and biogenic sources (low) (NARSTO, 2005). Detailed uncertainties for each source are shown in Table 2.1. E_E are estimated from CEMs, and E_A are directly derived from emissions of all airports in the U.S. (EPA, 2015). Therefore, they are typically accurate within 5% (Gluck et al., 2003). E_{NON} are more uncertain than E_{ON} due to poorly

known input parameters in MOBILE model (Dallmann and Harley, 2010). We then assigned 50% and 70% uncertainties to E_{ON} and E_{NON} individually. E_{OG} are mainly in the form of stationary nonpoint sources with low confidence level, a 100% uncertainty therefore assigned to. E_I consists mostly of non-EGU point emissions and part of nonpoint sources with an assumed 70% uncertainty. For natural sources, lightning NO_x is not well captured by satellite, because its major influence on the upper troposphere, especially in mid-latitudes during summer (Bucsela et al., 2013). Here, a 100% uncertainty is considered for E_L. Studies show that global E_S are about 10 Tg N/a (Hudman et al., 2012). The estimated NO_x emission from soil is highly uncertain, ranging from 4 to 15 Tg N/a and may be misinterpreted in spatial and temporal distribution (Vinken et al., 2014, Rasool et al., 2016). Hence, the uncertainty of E_S is also assumed 100%.

Table 2.1 Uncertainties of E_{ON}, E_{NON}, E_E, E_I, E_{OG}, E_A, E_S and E_L.

Source	Uncertainties
Onroad	50%
Nonroad	70%
EGU	5%
Industry	70%
Oil & Gas	100%
Aircraft	5%
Soil	100%
Lightning	100%

2.2.4 Inverse modeling of source-specific NO_x emissions

2.2.4.1 REAM and SSREAM

REAM is a 3-D tropospheric regional model, which has been applied and evaluated in many studies about emission inversions and tropospheric chemical mechanisms and physical processes in the U.S. and China (Gu et al., 2014, 2016; Zhao and Wang, 2009; Zhang et al., 2018; Li et al., 2019; Hang et al., 2020). This model has a horizontal resolution of 36×36 km^2 and 30 vertical layers in the troposphere. The transport process is driven by the meteorology field of Weather Research and Forecasting (WRF, version 3.9). The chemical mechanism is adopted from the GEOS-Chem model (v11.01) (Fisher et al., 2016). Chemical initiation and boundary conditions are consistently from GEOs-Chem simulation with a $2° \times 2.5°$ resolution. Biogenic emissions are computed hourly using the Model of Emissions of Gases and Aerosols from Nature (MEGAN) version 2.1 (Guenther et al., 2012) driven by WRF. Anthropogenic CO and VOC emissions are estimated from the EPA NEI 2011.

In order to distinguish NO_x sources, we built SSREAM upon REAM as shown in the orange and blue part of Figure 2.1, respectively. We add eight NO_x tracers to differentiate NO_x from different sources and independently track the production and loss of eight NO_x tracers in each grid box during chemical and physical processes. Because the long-term transport of nitrate reservoirs could dramatically increase the lifetime of NO_x in the troposphere, we flagged eight nitrate reservoir tracers corresponding to eight NO_x tracers in the same manner. The spin-up time of the SSREAM is a week. For computational efficiency, in the SSREAM, we combine 4 horizontal grid boxes into one grid box, therefore the resolution of each grid box is 72×72 km^2, and 30 vertical layers are evenly combined into six layers to capture the increasing lifetime of NO_x with height. The eight prior NO_x emissions are assigned to corresponding NO_x tracers at the initial time step.

During the chemical process, we tracked total chemical exchanges between NO_x and reservoirs at every one-hour chemical time step from the REAM and assigned the total NO_x change and NO_x reservoir change to corresponding eight NO_x tracers and reservoir tracers based on their ratios at the beginning of every chemical time step in the SSREAM, as the chemical process is homogenous for eight sources. Similarly, in the transport module, we tracked the total fluxes of NO_x and NO_x reservoirs separately in the REAM and assigned the fluxes to corresponding tracers according to saved proportions at the beginning of every five-minute transport time step in the SSREAM. We can then convert the NO_x tracers to NO_2 columns. Simulated tropospheric NO_2 VCDs of eight sources were calculated using the ratio of NO_2/NO_x in the REAM and separately outputted at each grid box hourly matching corresponding valid OMI observations.

2.2.4.2 3SDRI

The daily retrieval-inversion (DRI) method introduced by Gu et al. (2014) estimates the total emissions of NO_x using "bulk ratio" by coupling the retrieved profiles to inverse modeling. In this study, we improved the DRI method by considering detailed NO_x sources. We divide CONUS into three regions: the West, Central and East (Figure 2.2) and conduct inversion in three regions independently because the contribution of each source to the total emissions are spatially inconsistent. We apply a bounded multivariate linear regression between satellite observations and model simulations using Equation (2.1) in three regions on a daily basis to calculate the posterior emissions, constrained by the uncertainties of eight sources which are described in the section 2.2.3. The detailed derivations of Equation (2.1) are shown below:

$$\Omega_{sat} - \sum_i \Omega_i = \sum_i \frac{\partial \Omega_i}{\partial E_i} \Delta E_i k_i^{'} + \varepsilon \quad (1)$$

$$E_i^{poster} = k_i^{'} E_i^{pre-day} = k_i E_i^0 \quad (2)$$

$$k_i^{'} = k_i \frac{E_i^0}{E_i^{pre-day}} \quad (3)$$

Using Equation (1), (2) and (3), we derive:

$$\Omega_{sat} - \sum_i \Omega_i = \sum_i \frac{\partial \Omega_i}{\partial E_i} \Delta E_i k_i \frac{E_i^0}{E_i^{pre-day}} + \varepsilon \quad (2.1)$$

Ω_{sat} denotes the satellite observed tropospheric NO_2 VCDs. Ω_i (i = E_{ON}, E_{NON}, E_E, E_I, E_{OG}, E_A, E_S and E_L) denotes tropospheric NO_2 VCDs of eight emission sources. Δ denotes the change between current and initial timesteps. $k_i^{'}$ denotes the ratio between the posterior emissions after each inversion time step and the posterior emissions at the previous timestep. k_i denotes the ratio between the posterior emissions after each inversion time step and the prior emissions at the first timestep. ε (Normal distribution with zero means) is a random error term. At each inversion timestep (one day), we calculate the posterior emissions by multiplying the prior emissions (at the initial timestep) and k_i. After each inversion, eight emissions are updated in the model simulation with the newly calculated posterior emissions. To reduce the effect of varied natural emissions and one-day OMI measurements, at each timestep, we apply Equation (2.1) to all data from previous timesteps. Therefore, the final posterior emissions are calculated based on all usable simulation and observation results for JJA 2011.

Before applying multivariate linear regression of Equation (2.1), we first checked the correlations of each variable as shown in Table 2.2. Noted that Ω_{E_A}, $\Omega_{E_{ON}}$, $\Omega_{E_{NON}}$ and Ω_{E_I} are more correlated (correlations greater than 0.5) than other sources, we developed a 3SDRI method (Table 2.3) to reduce errors of the interdependence between variables within multivariate linear regression. As E_A are more certain, within 5% uncertainty, compared to E_{ON} (50%), E_{NON} (70%) and E_I (70%), we neglected impact of E_A on the regression results. At the first stage, we did daily inversion on six sources including E^{S1} ($E^{S1} = E_I + E_{ON} + E_{NON}$), E_E, E_{OG}, E_A, E_S and E_L and got a set of scaling factors k_i^{S1}. Because of the interdependency between E_I, E_{ON} and E_{NON}, we then did inversion on seven sources to distinguish E_I from E^{S1} at stage two, using outliers ($\Omega_{E_{ON}} + \Omega_{E_{NON}}$ and Ω_{E_I} outside of one standard error of the regression) of the linear regression between $\Omega_{E_{ON}} + \Omega_{E_{NON}}$ and Ω_{E_I} and fixing scaling factors of E_E, E_{OG}, E_A, E_S and E_L as what we derived at stage one to ensure the consistency of other sources. Similarly, we further distinguished E_{ON} and E_{NON}. Finally, the posterior emissions of eight sources in three regions were computed as the prior emissions multiplied by k_i^{S3} (i = E_{ON}, E_{NON}, E_E, E_I, E_{OG}, E_A, E_S and E_L).

Table 2.2 Correlations among Ω_i (i = E_{ON}, E_{NON}, E_E, E_I, E_{OG}, E_A, E_S and E_L) during JJA 2011 over West, Central and East CONUS.

West	Ω_{E_S}	Ω_{E_I}	Ω_{E_E}	$\Omega_{E_{ON}}$	$\Omega_{E_{NON}}$	$\Omega_{E_{OG}}$	Ω_{E_A}	Ω_{E_L}
Ω_{E_S}	1.000	0.086	0.035	0.110	0.187	0.219	0.314	0.138
Ω_{E_I}	0.086	1.000	0.031	0.695	0.683	0.006	0.499	-0.043
Ω_{E_E}	0.035	0.031	1.000	0.096	0.098	0.010	-0.036	0.003
$\Omega_{E_{ON}}$	0.110	0.695	0.096	1.000	0.802	0.003	0.557	0.063

$\Omega_{E_{NON}}$	0.187	0.683	0.098	0.802	1.000	0.093	0.552	-0.015
$\Omega_{E_{OG}}$	0.219	0.006	0.010	0.003	0.093	1.000	0.117	0.308
Ω_{E_A}	0.314	0.499	-0.036	0.557	0.552	0.117	1.000	0.161
Ω_{E_L}	0.138	-0.043	0.003	0.063	-0.015	0.308	0.161	1.000
Central	Ω_{E_S}	Ω_{E_I}	Ω_{E_E}	$\Omega_{E_{ON}}$	$\Omega_{E_{NON}}$	$\Omega_{E_{OG}}$	Ω_{E_A}	Ω_{E_L}
Ω_{E_S}	1.000	0.048	-0.009	0.161	0.329	0.291	0.172	0.004
Ω_{E_I}	0.048	1.000	-0.090	0.476	0.333	0.064	0.251	0.053
Ω_{E_E}	-0.009	-0.090	1.000	-0.133	-0.054	-0.083	-0.146	-0.145
$\Omega_{E_{ON}}$	0.161	0.476	-0.133	1.000	0.639	0.228	0.460	0.125
$\Omega_{E_{NON}}$	0.329	0.333	-0.054	0.639	1.000	0.190	0.398	0.158
$\Omega_{E_{OG}}$	0.291	0.064	-0.083	0.228	0.190	1.000	0.181	0.173
Ω_{E_A}	0.172	0.251	-0.146	0.460	0.398	0.181	1.000	0.101
Ω_{E_L}	0.004	0.053	-0.145	0.125	0.158	0.173	0.101	1.000
East	Ω_{E_S}	Ω_{E_I}	Ω_{E_E}	$\Omega_{E_{ON}}$	$\Omega_{E_{NON}}$	$\Omega_{E_{OG}}$	Ω_{E_A}	Ω_{E_L}
Ω_{E_S}	1.000	0.238	-0.074	0.246	0.294	0.160	0.306	0.142
Ω_{E_I}	0.238	1.000	0.072	0.706	0.730	0.116	0.563	0.092
Ω_{E_E}	-0.074	0.072	1.000	0.086	0.080	-0.033	0.156	-0.174
$\Omega_{E_{ON}}$	0.246	0.706	0.086	1.000	0.841	0.091	0.732	0.079
$\Omega_{E_{NON}}$	0.294	0.730	0.080	0.841	1.000	0.065	0.670	0.062
$\Omega_{E_{OG}}$	0.160	0.116	-0.033	0.091	0.065	1.000	0.122	0.112
Ω_{E_A}	0.306	0.563	0.156	0.732	0.670	0.122	1.000	0.084
Ω_{E_L}	0.142	0.092	-0.174	0.079	0.062	0.112	0.084	1.000

Table 2.3 Descriptions of three stages in 3SDRI.

Stage	Description
1	Do inversion on 6 sources, E^{S1} (E^{S1} = E_I + E_{ON} + E_{NON}), E_E, E_{OG}, E_A, E_S and E_L.
2	Do inversion on 7 sources, E_I, E^{S2} (E^{S2} = E_{ON} + E_{NON}), E_E, E_{OG}, E_A, E_S and E_L, using outliers of linear regression between Ω_{E_I} and $\Omega_{E^{S2}}$ and fixing k_i^{S2} as k_i^{S1}(i = E_E, E_{OG}, E_A, E_S and E_L).
3	Do inversion on 8 sources, E_{ON}, E_{NON}, E_E, E_I, E_{OG}, E_A, E_S and E_L, using outliers of linear regression between $\Omega_{E_{ON}}$ and $\Omega_{E_{NON}}$, fixing k_i^{S3} as k_i^{S2}(i = E_I, E_E, E_{OG}, E_A, E_S and E_L).

2.2.5 Surface ozone observations

Hourly surface ozone measurements are obtained from the US EPA Air Quality System (AQS) (https://www3.epa.gov/airdata/), collected at 1333 observation sites with available data during JJA 2011 and converted to ambient surface maximum daily 8-h average (MDA8). Model simulations with original and updated NO_x emissions from inversion results are evaluated in the West, Central and East CONUS. We chose to analyze the statistics of model and observations for mean bias (MB), mean error (ME), normalized mean bias (NMB), normalized mean error (NME), and correlation coefficient (r) and root mean square error (RMSE) according to Simon et al. (2012) to demonstrate the impact of uncertainties of NO_x emissions on ozone simulations.

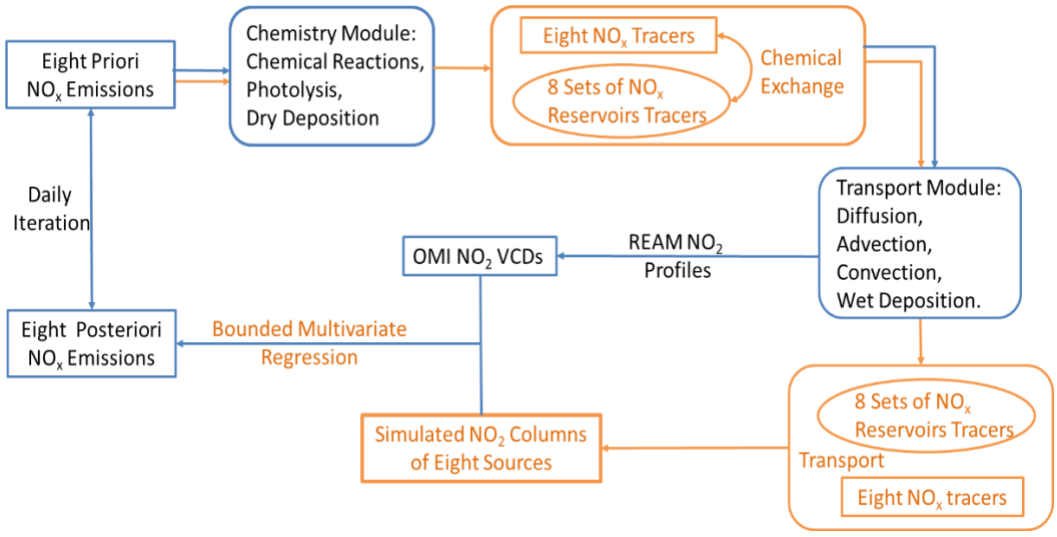

Figure 2.1 Schematic diagrams of SSREAM (orange) built in REAM (blue). In SSREAM, we have two sets of tracers including NO_x and NO_x reservoirs, which are individually tracked for E_{ON}, E_{NON}, E_E, E_I, E_{OG}, E_A, E_S and E_L sources at each chemical (1 hr) and transport (5 min) time step. E_{ON}, E_{NON}, E_E, E_I, E_{OG}, E_A, E_S and E_L are updated iteratively using a 3SDRI method on a daily basis.

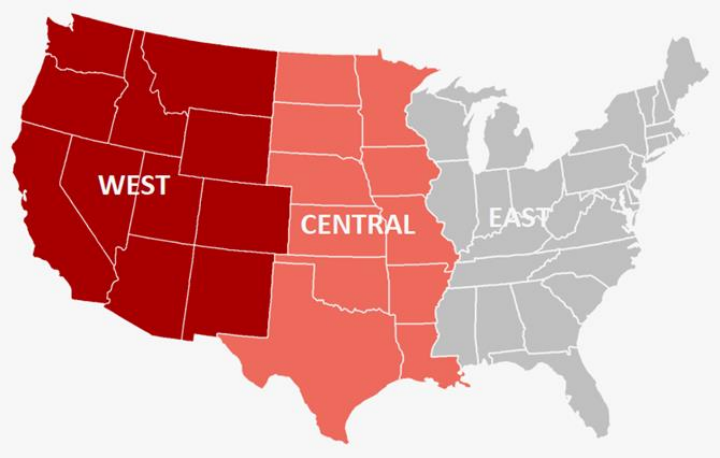

Figure 2.2 Region definitions of the West, Central and East CONUS.

2.3 Results and discussion

2.3.1 The prior source-specific NO_x emissions and modeled tropospheric NO_2 VCDs

Model simulations were conducted based on NO_x emissions from source-specific 2011 NAQFC emissions. The total prior NO_x emissions over CONUS are 5.00 Tg N/a. Distributions of the prior NO_x emissions of each source over the West, Central and East CONUS are shown in Figure 2.3, and respective contributions to the total emissions are in Figure 2.4. Natural emissions exhibit large spatial and seasonal variations (Jaeglé et al., 2005; Pickering et al., 2016). We found that natural sources take up 33.2% of the total emissions over the CONUS. E_L, consisting 17.9% of total emissions, have a substantial impact on the upper troposphere with a longer NO_x lifetime of several days. (Pickering et al., 1998). E_L contribute more than 80% of the total NO_x near the Rocky Mountains, followed by 60-70% contributions over the Southeast. Over the CONUS, 62% of E_S occur

between May to August (EPA, 2016). It shows that 53% of total E_S are in the Central regions, especially over agricultural Great Plain, taking up approximately 40% of the total NO_x emissions. High soil NO_x emissions are also collocated with national parks over the West CONUS, contributing more than 60% to the total emission in certain grid boxes. E_{ON} are the major anthropogenic emissions accounting for 20.7% of the total prior emissions over the CONUS, followed by E_E, E_{NON}, E_I, E_{OG} and E_A, exhibiting a correlated pattern with distributions of metropolitan areas and highways. E_E are 0.72 Tg N/a and attributed to point sources from electric power plants near large cities, taking up to 80% of total NO_x emissions around areas near power plants, while E_I are mostly non-EGU emissions. The largest emitting categories of E_I include external combustion boilers, internal combustion engines, and chemical manufacturing (EPA, 2010), located mainly in the East with 53.4% of the total E_I. The spatial distribution of E_{NON} dominates in the Midwest and Northern Great Plains matching fertilizer using areas (Cao et al., 2018), contributing 40-50% to the total NO_x emissions, which indicates nonroad emissions are closely related to agricultural activity facilities. Drilling, production and gas flaring activities are conducted in seven key Oil & Gas production areas (Figure 2.5), emitting a large amount of NO_x that compose up to 90% local NO_x emissions. E_A are collocated with flight tracks and large airports, and only take about 6% of annual NO_x emissions.

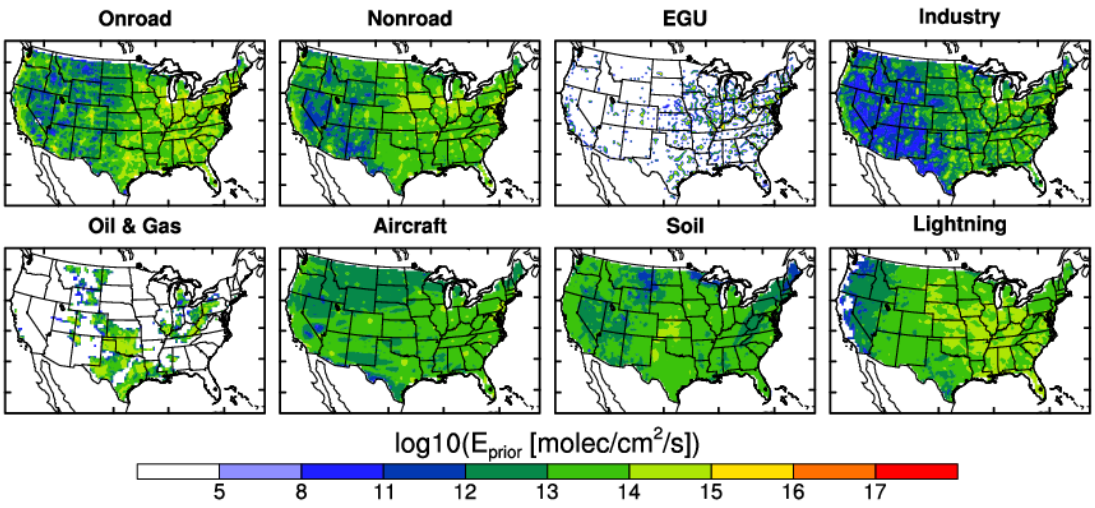

Figure 2.3 The prior estimates of E_{ON}, E_{NON}, E_E, E_I, E_{OG}, E_A, E_S and E_L in logarithmic scale over the CONUS for JJA 2011.

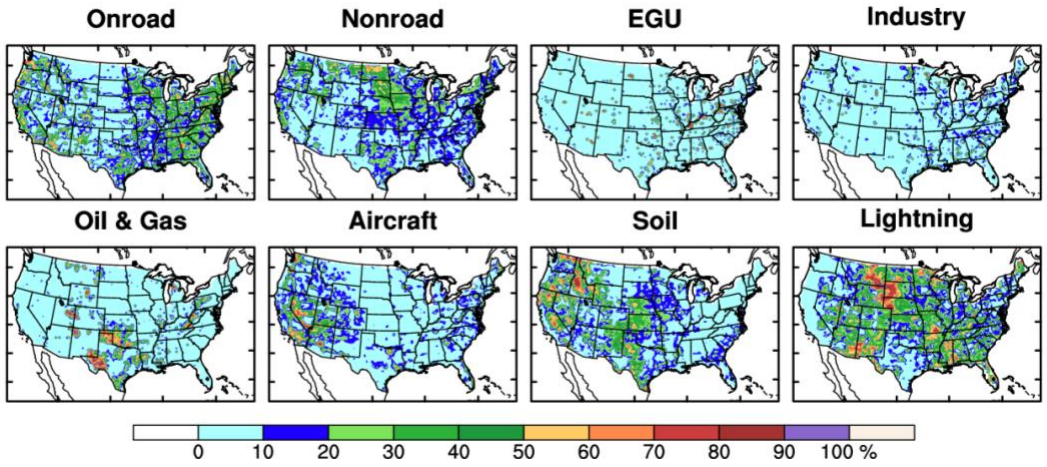

Figure 2.4 Averaged contributions of the prior source-specific NO_x emissions (E_{ON}, E_{NON}, E_E, E_I, E_{OG}, E_A, E_S and E_L) to the total prior NO_x emissions in percentage over the CONUS for JJA 2011.

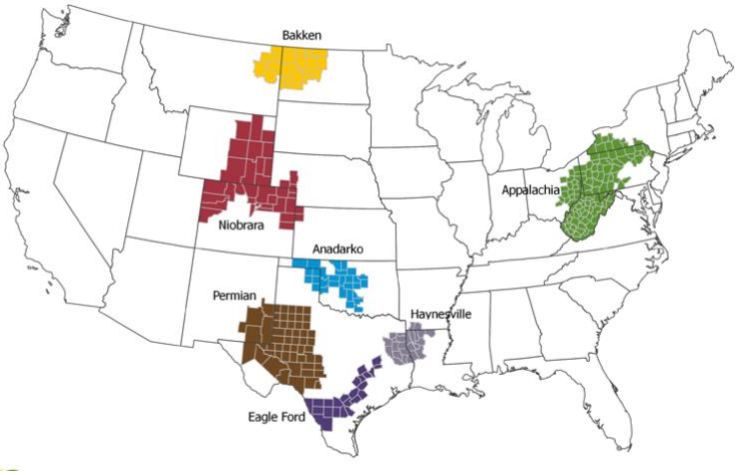

Figure 2.5 Seven key oil and gas production areas over the CONUS from US Energy Information Administration (https://www.eia.gov/petroleum/drilling/#tabs-summary-2).

We show the simulated and retrieved OMI total tropospheric NO_2 VCDs in Figure 2.6. The cross-correlation between satellite observations and simulation results with the prior emissions are 0.58. Noted that compared to the results of the REAM simulations using the posterior emissions and MI results using SSREAM, the correlations increase to 0.82 and 0.71, respectively. Simulated NO_2 VCDs with the posterior emissions computed using 3SDRI by SSREAM have the best match to retrieved columns. The 3SDRI method ensures the consistency of the prior emissions, retrieved profiles and inverse modeling results, and reduces the dependence of posterior emissions on the prior. The modeled results using REAM with the prior emissions are biased high over the Central and in some large cities compared to the OMI observations. Monthly inversion method using SSREAM could reduce the high NO_2 VCDs simulated by REAM over the Central region around Kansas, but still have problems capturing NO_2 VCDs over metropolitan areas and Central

agricultural regions. The remaining differences between 3SDRI results and satellite retrievals imply that detailed region divisions are needed in the future and some unreported emissions could exist.

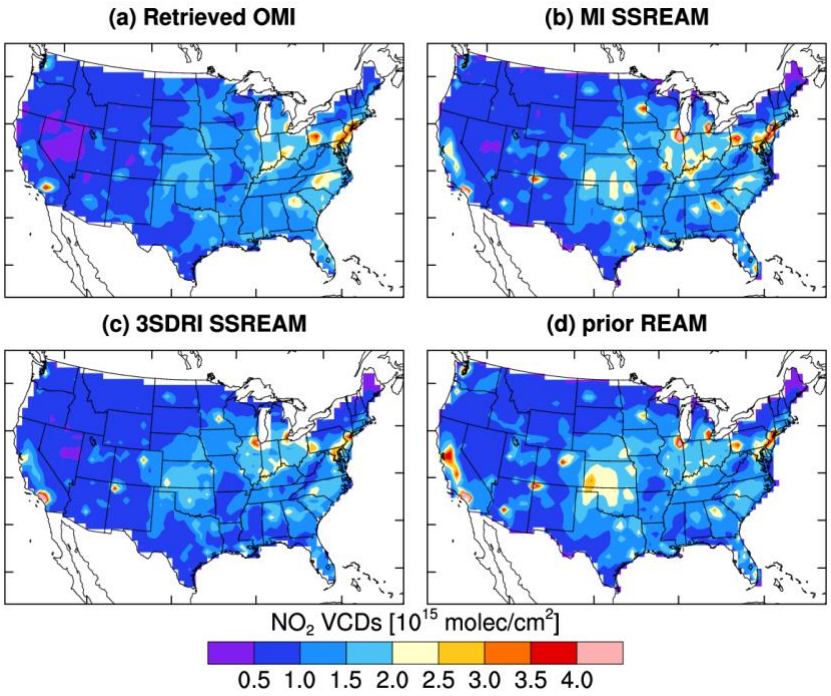

Figure 2.6 Total tropospheric NO_2 VCDs (a) retrieved from OMI, (b) simulated by SSREAM using MI method, (c) simulated by SSREAM using 3SDRI method and (d) simulated by REAM using the prior emissions for JJA 2011.

2.3.2 The posterior source-specific NO_x emissions

The total posterior emissions of NO_x over CONUS are estimated to be 5.02 Tg N/a using the 3SDRI method in consistent with the prior emissions, while better matches of NO_2 VCDs between satellite observations and model simulations using the 3SDRI method are achieved. It indicates that EPA has a good estimation of total NO_x emissions, but the source distributions are biased. Figure 2.7 shows the source-specific posterior emissions of NO_x using the 3SDRI method with detailed numbers in **Table 2.4** and relative contributions

of each source in Figure 2.8. We compare the prior and posterior emissions and show detailed contributions of each source to the total over the West, Central, East and CONUS in Figure 2.9. Total emissions of the Central are increased by 5% from 1.89 Tg N/a to 1.99 Tg N/a, compensated by decreases over the West (from 0.95 Tg N/a to 0.93 Tg N/a) and East (from 2.16 Tg N/a to 2.09 Tg N/a). The scaling factors of E_{ON}, E_{NON}, E_E, E_I, E_{OG}, E_A, E_S and E_L derived from Eqs. (1) over the West, Central and East CONUS for JJA 2011 are shown in Table 2.5.

Table 2.4 The prior and posterior annual NO_x emissions (Tg N/a) of E_{ON}, E_{NON}, E_E, E_I, E_{OG}, E_A, E_S and E_L over the West, Central, East and CONUS.

Source	CONUS		West		Central		East	
	Prior	Posterior	Prior	Posterior	Prior	Posterior	Prior	Posterior
Onroad	1.03	0.82	0.19	0.13	0.25	0.23	0.59	0.46
Nonroad	0.58	0.57	0.10	0.06	0.21	0.25	0.28	0.26
EGU	0.72	0.70	0.10	0.10	0.24	0.23	0.37	0.38
Industry	0.40	0.45	0.05	0.04	0.13	0.17	0.21	0.25
Oil & Gas	0.31	0.41	0.05	0.05	0.17	0.25	0.08	0.12
Aircraft	0.30	0.33	0.14	0.16	0.12	0.14	0.03	0.03
Soil	0.76	0.67	0.19	0.18	0.40	0.27	0.18	0.22
Lightning	0.90	1.06	0.12	0.23	0.37	0.46	0.42	0.37
Total	5.00	5.02	0.95	0.93	1.89	1.99	2.16	2.09

Table 2.5 The estimated scaling factors of E_{ON}, E_{NON}, E_E, E_I, E_{OG}, E_A, E_S and E_L using 3SDRI method over the West, Central and East CONUS for JJA 2011.

Source	West	Central	East
Onroad	0.67	0.94	0.78
Nonroad	0.58	1.2	0.95
EGU	0.95	0.95	1.01
Industry	0.71	1.29	1.15
Oil & Gas	0.82	1.44	1.5
Aircraft	1.1	1.1	1.1
Soil	0.95	0.67	1.24
Lightning	2	1.26	0.89

Over the West, anthropogenic emissions, especially vehicle emissions overestimated by 18.8%, are expected to have 12% fewer contributions to the West NO_x emissions, while natural emissions, in contrast, are underestimated by 35.4% with 13% more contributions, suggesting underestimations of lightning NO_x emissions and overestimations of E_{ON} and E_{NON} across the U.S. Mountain West States. It implies that NO_x emissions originated from transportation activities are overestimated in the model over those regions. E_{OG} are important NO_x sources over the Central and the East, but subject to large uncertainties related to missing emission source types and inaccurate oil and gas activity data (Allen et al., 2016). We found 44% and 50% underestimation of E_{OG} over the Central and the East, respectively. It shows that E_{OG} make 3% more contributions over the Central with 2% more E_I and 2% less E_E contributions. Over the Great Plains, E_S are dominant sources and have unique pulsing effects of emissions following the dry spell (Hudman et al., 2012). E_S have significant temporal and emission uncertainties, which are overestimated by 33% and have a corresponding 7% fewer contribution over the Central. Over the East, contributions of natural emissions are invariant. We found E_{ON} contribute 5% less to the emissions over the East compared to the prior emissions and are compensated by E_{OG} and E_I with 2% more contributions respectively. Over the CONUS, on the report of EPA emission estimations, mobile emissions are 1.71 Tg N/a in the NEI2011 and are cut by 50% in the NEI2014v2 (EPA, 2015). Here, we achieve the posterior mobile emissions of 1.39 Tg N/a, indicating that EPA may excessively reduce mobile emissions in the NEI2014v2, and a 20% reduction of NEI2011 mobile emissions are expected. Generally, over the CONUS, we found total natural contributions remain, the

contributions of E_{ON} are overestimated by 5% offsetting by more contributions from E_{OG}, E_I and E_A.

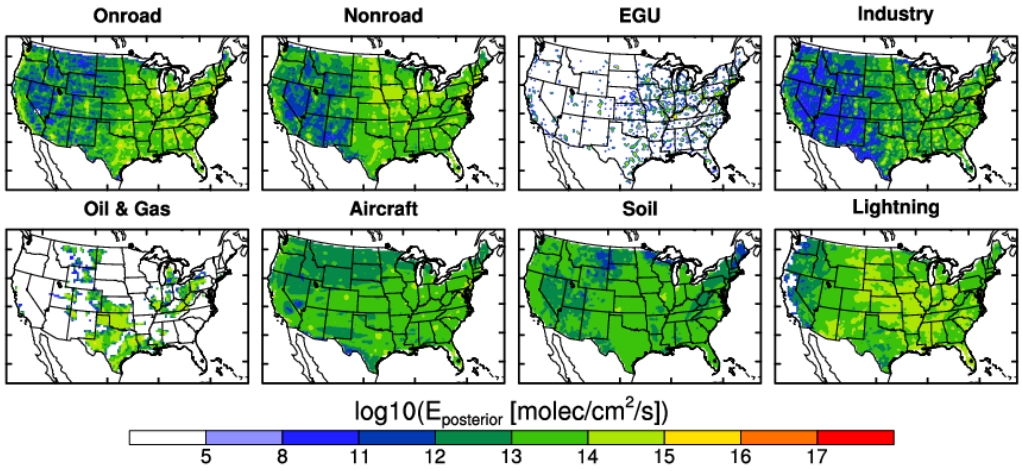

Figure 2.7 The posterior estimates of E_{ON}, E_{NON}, E_E, E_I, E_{OG}, E_A, E_S and E_L by SSREAM using 3SDRI method in logarithm scale over the CONUS for JJA 2011.

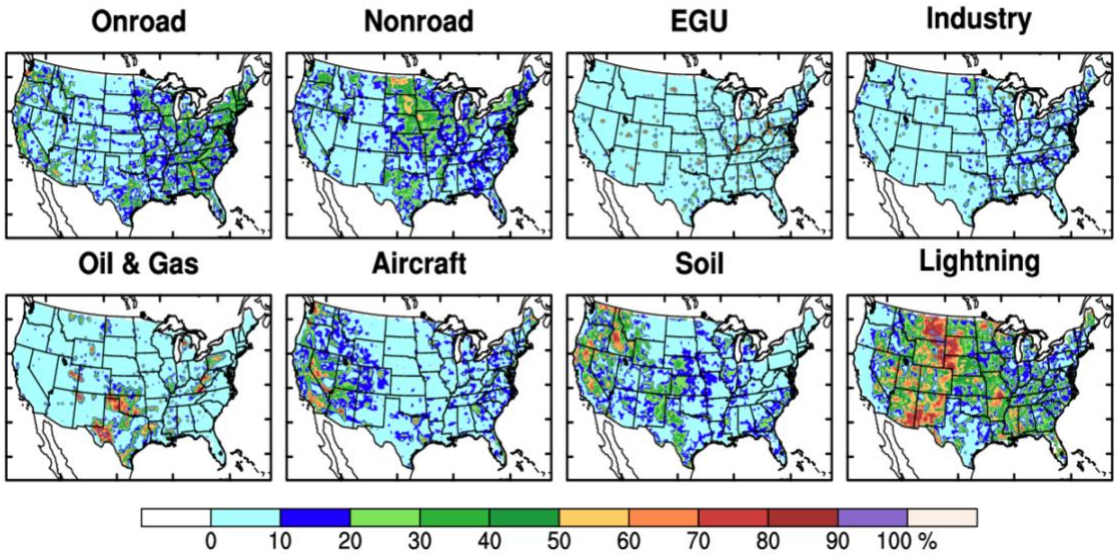

Figure 2.8 Averaged contributions of the posterior source-specific NO_x emissions (E_{ON}, E_{NON}, E_E, E_I, E_{OG}, E_A, E_S and E_L) to the total posterior NO_x emissions in percentage over the CONUS for JJA 2011.

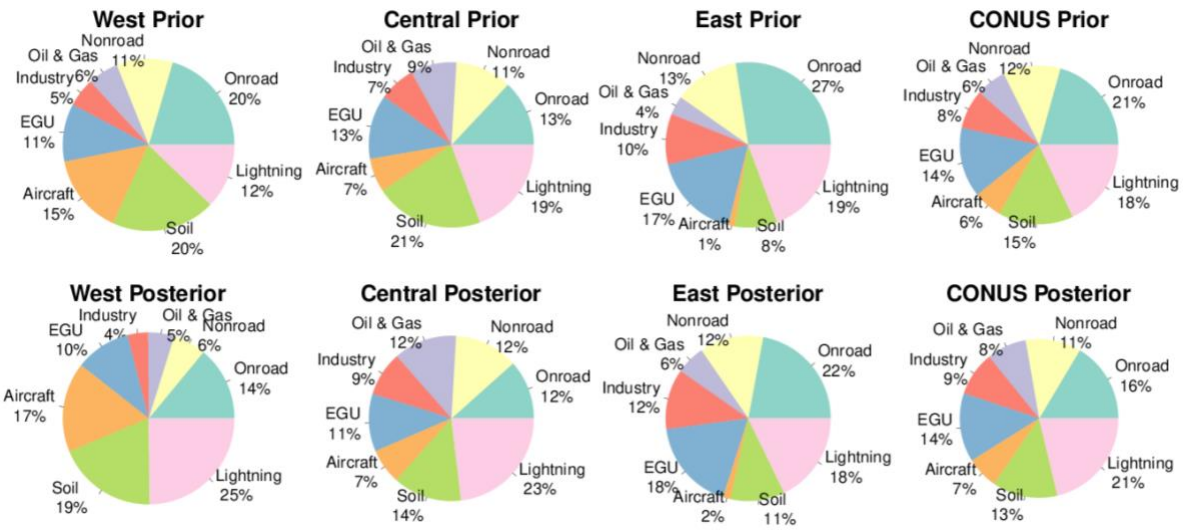

Figure 2.9 Relative distribution of the E_{ON}, E_{NON}, E_E, E_I, E_{OG}, E_A, E_S and E_L to the total prior (top) emissions and posteriori (bottom) emissions estimated by SSREAM using 3SDRI method over the West, Central, East and CONUS in logarithm scale for JJA 2011.

2.3.3 Contributions of modeled source-specific NO_2 VCDs to total NO_2 VCDs

In the SSREAM, tropospheric NO_2 VCDs of each source are simulated and constrained by OMI measurements (Figure 2.10). Figure 2.11 shows averaged contributions of tropospheric NO_2 VCDs from each source to the total tropospheric NO_2 VCDs simulated by SSREAM using 3SDRI method for JJA 2011. The contributions of anthropogenic NO_2 VCDs to the total NO_2 VCDs are spatially consistent with contributions of posterior anthropogenic emissions, while it differs for lightning in some regions. NO_2 VCDs of lightning take up approximately 30% of total VCDs over southern Texas, though E_L only contribute about 10% to the total NO_x emissions. Compared to anthropogenic

emissions generating mainly near the surface, E_L locate at higher altitudes with longer lifetime. Therefore, E_L have higher column impacts compared to surface NO_x emissions. It is also noted that high E_L contributions over the north of the Rocky Mountain area are not consistent with the low NO_2 VCDs contributions of lighting. It is possible that inconsistencies come from the difference between how we calculated natural emissions and mean NO_2 VCDs. We selected grid boxes corresponding to valid satellite retrievals, sampled at 13:30 LT, to calculate the mean NO_2 VCDs for JJA 2011, while E_L are averaged over all days for JJA 2011. In previous studies, E_S are predicted to have as much as 60% contributions to the NO_2 columns over the Great Plains where anthropogenic impacts are relatively small (Hudman et al., 2012), in consistent with our results that about 50% E_S contribute to the total columns over the Great Plains. When total anthropogenic contributions are considered, it is found that NO_2 VCDs with more than 80% human impacts are mainly located over metropolitan areas and Oil & Gas production areas, whereas, in other regions over the CONUS, natural sources generally contribute 30-50% of the total NO_2 VCDs with an average of 38.2% and as much as 60% over certain areas in the summer 2011.

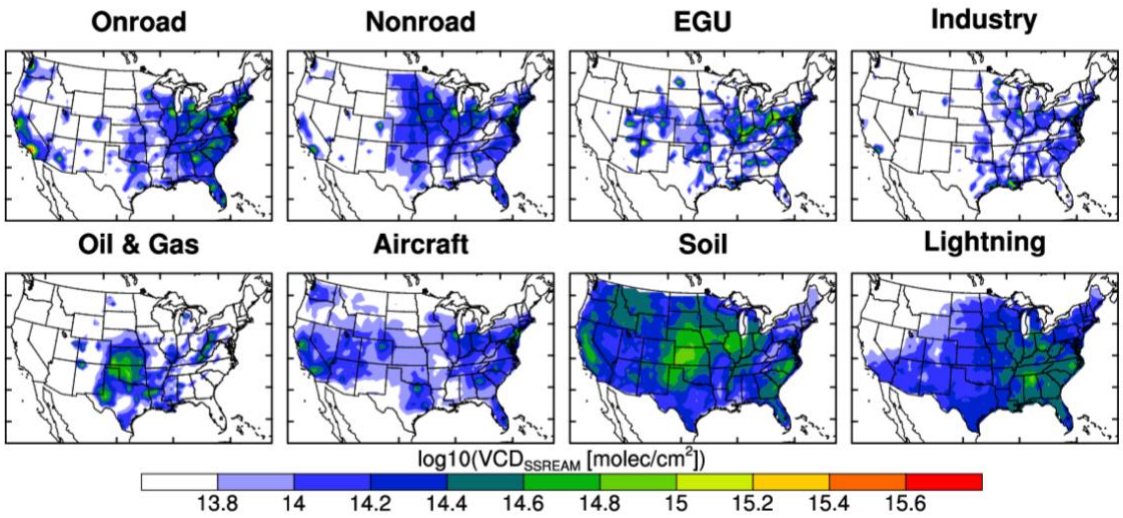

Figure 2.10 Averaged tropospheric NO_2 VCDs of eight emission sources (E_{ON}, E_{NON}, E_E, E_I, E_{OG}, E_A, E_S and E_L) estimated by SSREAM for JJA 2011.

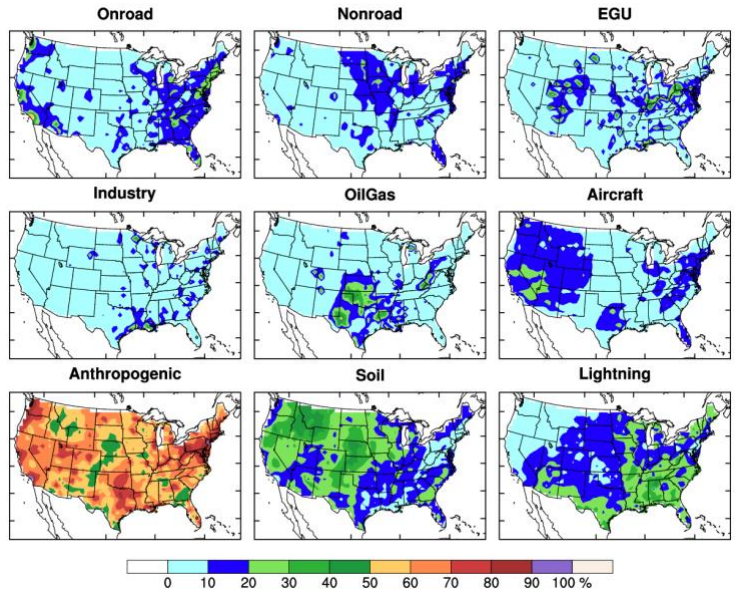

Figure 2.11 Averaged contributions of source-specific tropospheric NO_2 VCDs from E_{ON}, E_{NON}, E_E, E_I, E_{OG}, E_A, E_S and E_L to the total tropospheric NO_2 VCDs simulated by SSREAM using 3SDRI method in percentage for JJA 2011, matching corresponding valid OMI retrievals.

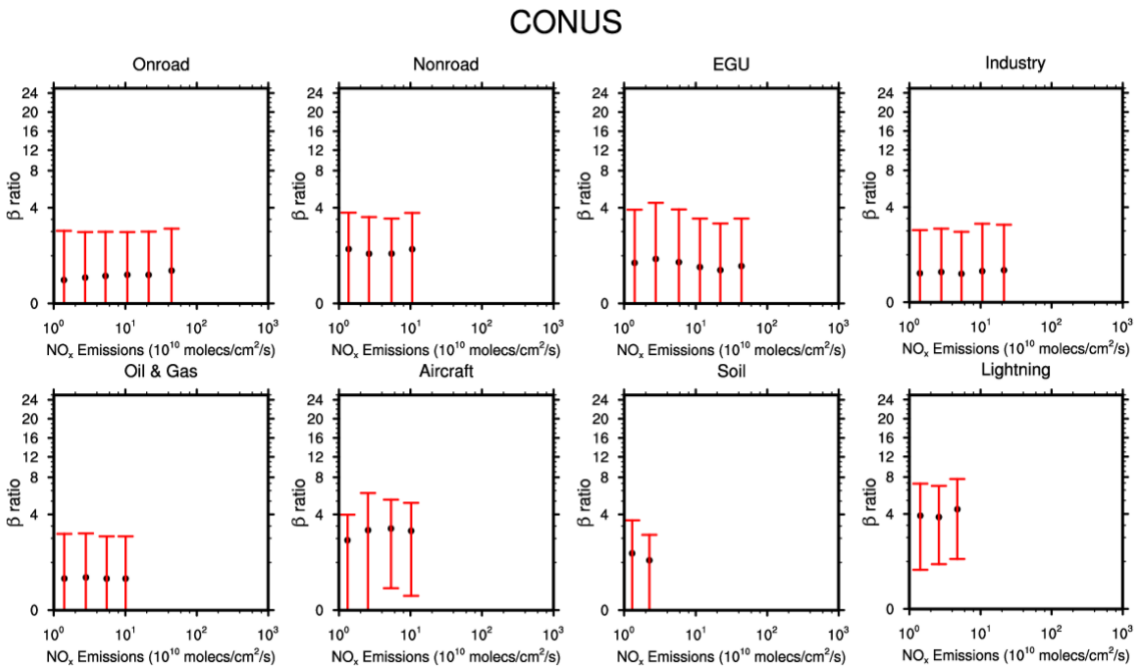

Figure 2.12 Simulated average β values as a function of E_{ON}, E_{NON}, E_E, E_I, E_{OG}, E_A, E_S and E_L over the CONUS for JJA 2011. The data are binned into seven groups based on NO_x emissions: E_i (i= ON, NON, E, I, OG, A, S)$\in$ (0, 2^1], (2^1, 2^2], (2^2, 2^3], (2^3, 2^4], (2^4, 2^5], (2^5, 2^6], (2^6, 2^7] × 10^{10} molecules/cm^2/s. (0, 2^1] denotes 0< $E_i \leq 2^1 \times 10^{10}$ molecules/cm^2/s. Error bars denote one standard deviation of the binned data.

2.3.4 Nonlinear relationships between source-specific NO_x emissions and NO_2 VCDs

Total vertical NO_2 columns are closely related to NO_x emissions due to relative short lifetime of NO_x and high NO_2/NO_x ratios in the lower troposphere (Martin et al., 2003; Lamsal et al., 2011). NO_2 VCDs are not linearly correlated with NO_x emissions due to the nonlinear photochemical procedures of NO_x (Gu et al., 2013; Li et al., 2019). We investigate the nonlinearity between NO_2 VCDs and eight NO_x emissions by examining the sensitivities (β_i , i = E_{ON}, E_{NON}, E_E, E_I, E_{OG}, E_A, E_S and E_L) of different NO_2 VCDs (Ω_i) to corresponding NO_x emissions (E_i):

$$\frac{\Delta E_i}{E_i} = \beta_i \frac{\Delta \Omega_i}{\Omega_i}$$

where ΔE_i denotes the emission changes of E_{ON}, E_{NON}, E_E, E_I, E_{OG}, E_A, E_S and E_L, and $\Delta \Omega_i$ is the corresponding changes of simulated tropospheric NO_2 vertical columns. β_i is used as a proxy of nonlinear feedback between source-specific NO_x emissions and NO_2 VCDs. We calculate the β values of each source for JJA 2011 over the CONUS, West, Central and East using SSREAM. In the base simulation, we use the prior emissions in the model to calculate NO_2 VCDs of each sector. Because the calculation of β values are insensitive to varied emission perturbations (Gu et al., 2013; Li et al., 2019), we choose to change the emissions to the posterior emissions in the sensitivity simulation with perturbations shown in Table 2.5. The β values of eight sources are computed using the base and sensitivity simulations.

Figure **2.12** shows the simulated average β values of eight sources over the CONUS for JJA 2011 as a function of corresponding NO_x emissions binned into seven emission groups. For specific emission sources, we find no significant change of β values as the emission increase. The β values are fluctuating around 1.0 for nonroad, EGU and soil sources, indicating a small nonlinearity effect. For onroad, industry and Oil & Gas, the mean β values are in the range of 0.5-0.7, implying that the emission changes are about 30-50% lower than the changes of NO_2 VCDs. As aircraft and lightning emissions impose more impacts on the upper layers, we find that β values are generally higher than 2.0 and as high as 4.3 for lightning. It indicates that compared to ground sources, the change of NO_2 VCDs are less sensitive to emission changes when emission sources are dominant at

higher levels. Similar results are found in the West, Central and East shown in the Figure **2.13**, Figure **2.14** and Figure **2.15**.

The newly developed 3SDRI method estimates NO_x emissions of six anthropogenic sources (E_{ON}, E_{NON}, E_E, E_I, E_{OG} and E_A) and two natural sources (E_S and E_L) respectively over West, East and Central CONUS for 2011. Tropospheric NO_2 VCDs of each source are simulated separately in the SSREAM constrained by OMI observations, providing detailed column contributions of different NO_x sources during JJA 2011. Inversion results show consistent total NO_x emissions of 5.02 Tg N/a with the prior NAQFC emissions, but distributions of each source are biased. Soil and lightning NO_x have large contributions as much as 60% to NO_2 columns in the summer 2011. Surface maximum daily 8-h average ozone (MDA8) modeled in the SSREAM using 3SDRI methods are compared to EPA Air Quality System observations (Figure 2.16). Ozone concentrations simulated over the West are relatively improved with more lightning NO_x emissions in the model compared to the East and Central (Figure 2.17, Figure 2.18, Figure 2.19, Table 2.6). It indicates that ozone levels in the West could be greatly modulated by natural sources, which matches the results of Kang et al. (2020). In Figure 2.16, MDA8 ozone concentrations are slightly decreased with posterior emissions over the West and Central by about 1-3 ppb, except over large cities and Oil & Gas areas, and generally increased over the East. Noted that better distributions of NO_x emissions largely improve modeled NO_2 columns but could have small impacts on MDA8 ozone simulations over the Central and East. Besides, large contributions of anthropogenic emissions over the East, especially the Northeast, suggest the importance of regional emission regulations in the future.

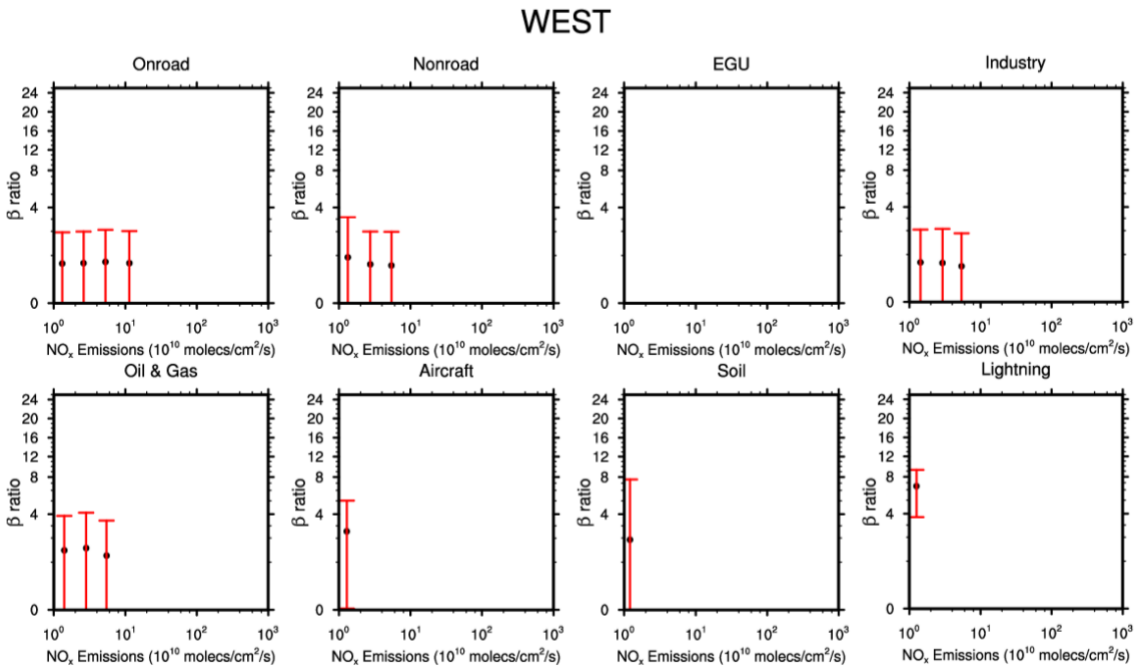

Figure 2.13 Simulated average β values as a function of E_{ON}, E_{NON}, E_E, E_I, E_{OG}, E_A, E_S and E_L over the WEST for JJA 2011. The data are binned into seven groups based on NO_x emissions: E_i (i= ON, NON, E, I, OG, A, S)$\in$ (0, 2^1], (2^1, 2^2], (2^2, 2^3], (2^3, 2^4], (2^4, 2^5], (2^5, 2^6], (2^6, 2^7] × 10^{10} molecules/cm^2/s. (0, 2^1] denotes 0< $E_i \leq 2^1 \times 10^{10}$ molecules/cm^2/s. Error bars denote one standard deviation of the binned data.

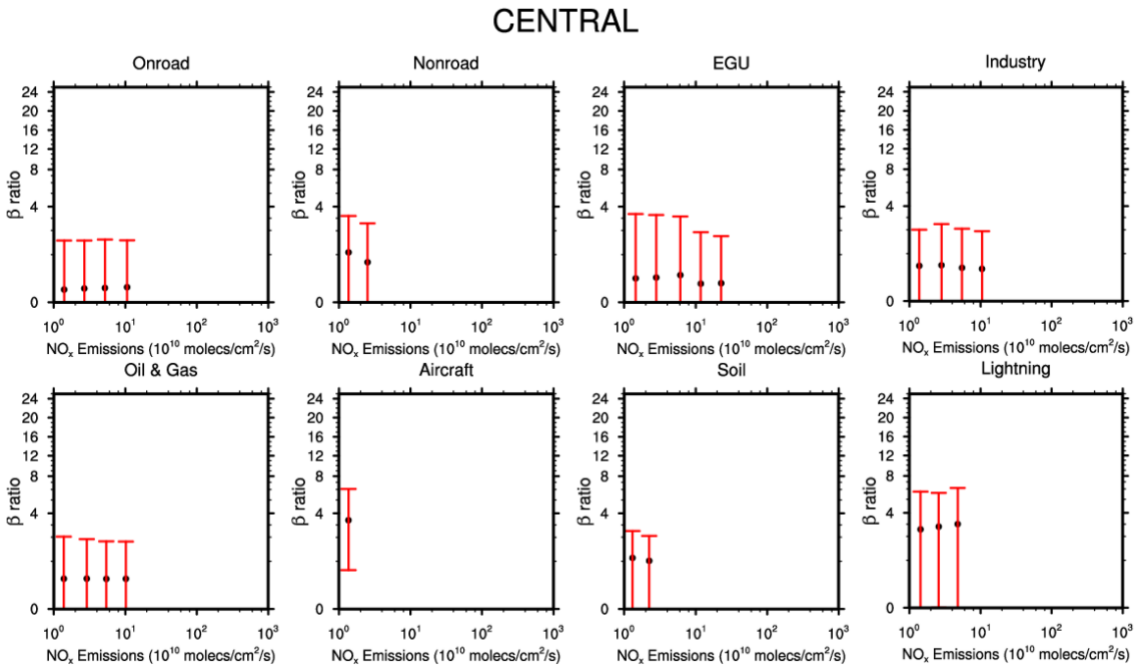

Figure 2.14 Simulated average β values as a function of E_{ON}, E_{NON}, E_E, E_I, E_{OG}, E_A, E_S and E_L over the CENTRAL for JJA 2011. The data are binned into seven groups based on NO_x emissions: E_i (i= ON, NON, E, I, OG, A, S)$\in$ (0, 2^1], (2^1, 2^2], (2^2, 2^3], (2^3, 2^4], (2^4, 2^5], (2^5, 2^6], (2^6, 2^7] × 10^{10} molecules/cm^2/s. (0, 2^1] denotes 0< $E_i \leq 2^1 \times 10^{10}$ molecules/cm^2/s. Error bars denote one standard deviation of the binned data.

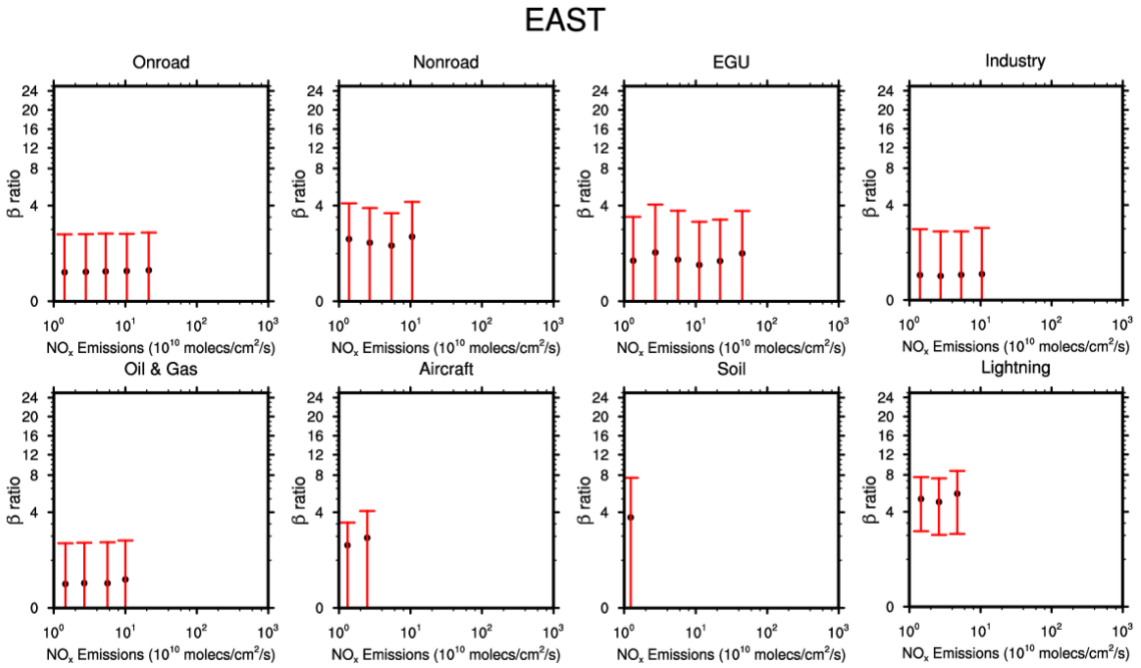

Figure 2.15 Simulated average β values as a function of E_{ON}, E_{NON}, E_E, E_I, E_{OG}, E_A, E_S and E_L over the EAST for JJA 2011. The data are binned into seven groups based on NO_x emissions: E_i (i= ON, NON, E, I, OG, A, S)$\in$ (0, 2^1], (2^1, 2^2], (2^2, 2^3], (2^3, 2^4], (2^4, 2^5], (2^5, 2^6], (2^6, 2^7] × 10^{10} molecules/cm^2/s. (0, 2^1] denotes 0< $E_i \leq 2^1 \times 10^{10}$ molecules/cm^2/s. Error bars denote one standard deviation of the binned data.

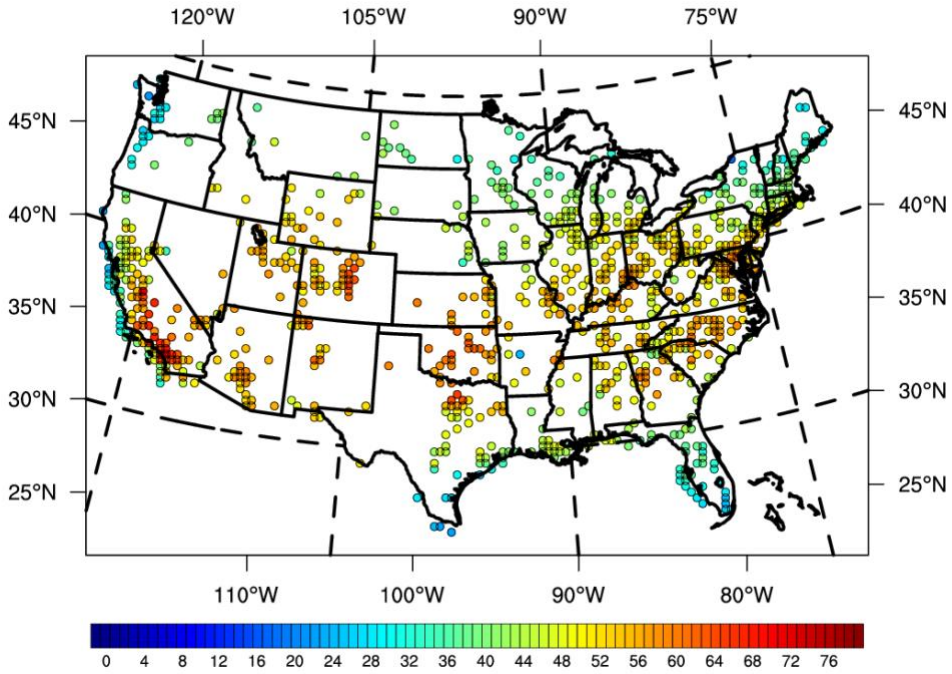

Figure 2.16 Locations of AQS ozone surface observation sites and averaged MDA8 ozone observed at AQS sites for JJA 2011.

Table 2.6 The statistics of simulations and observations for MDA8 ozone over the West, Central and East CONUS.

monthly	MB	NMB	ME	NME	RMSE	R^2
posterior (W)	0.10	0.01	1.91	0.14	4.76	0.40
prior (W)	0.46	0.03	1.96	0.14	4.94	0.38
posterior (C)	-0.46	-0.04	1.58	0.14	3.90	0.53
prior (C)	-0.37	-0.03	1.57	0.13	3.87	0.52
posterior (E)	-0.13	0.00	2.80	0.08	4.27	0.63
prior (E)	-0.90	-0.03	2.97	0.09	4.45	0.62

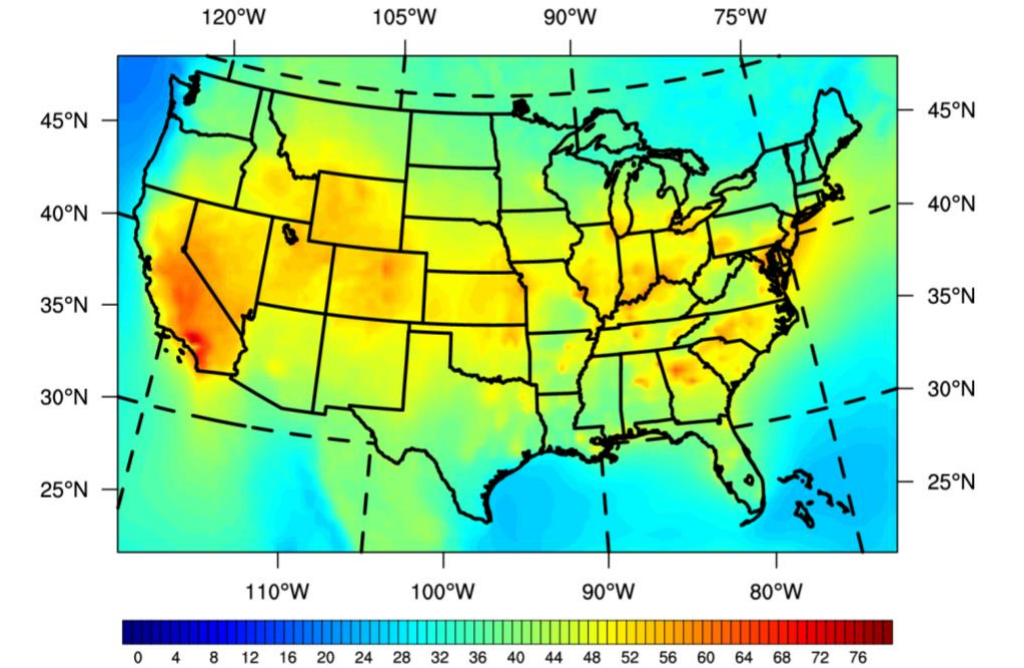

Figure 2.17 Averaged MDA8 ozone with the prior emissions in the REAM for JJA 2011.

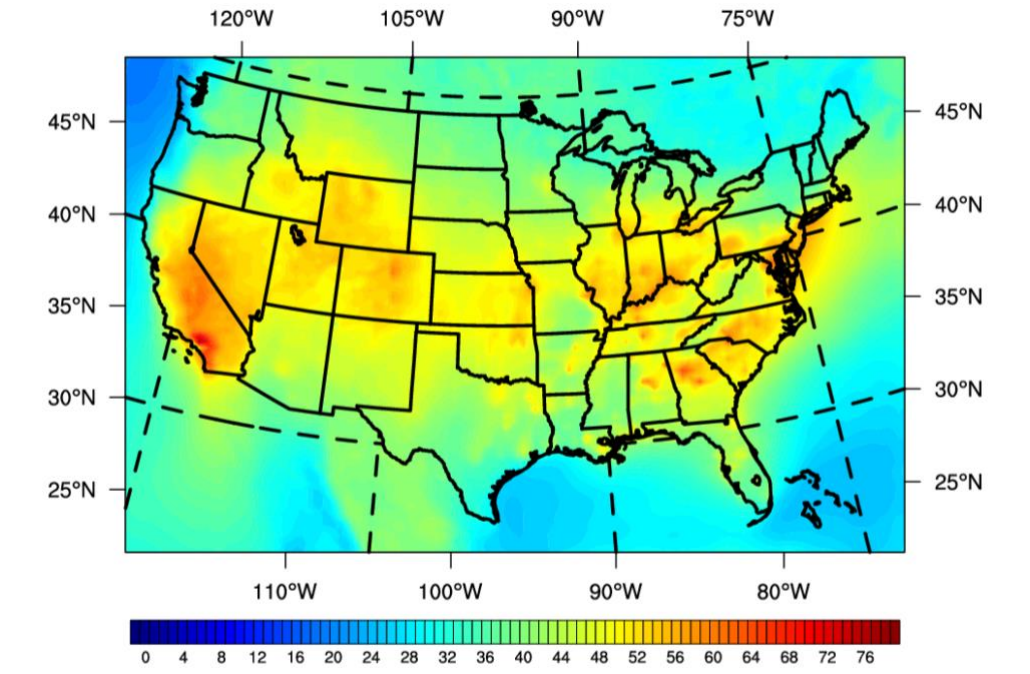

Figure 2.18 Averaged MDA8 ozone with the posterior emissions in the SSREAM for JJA 2011.

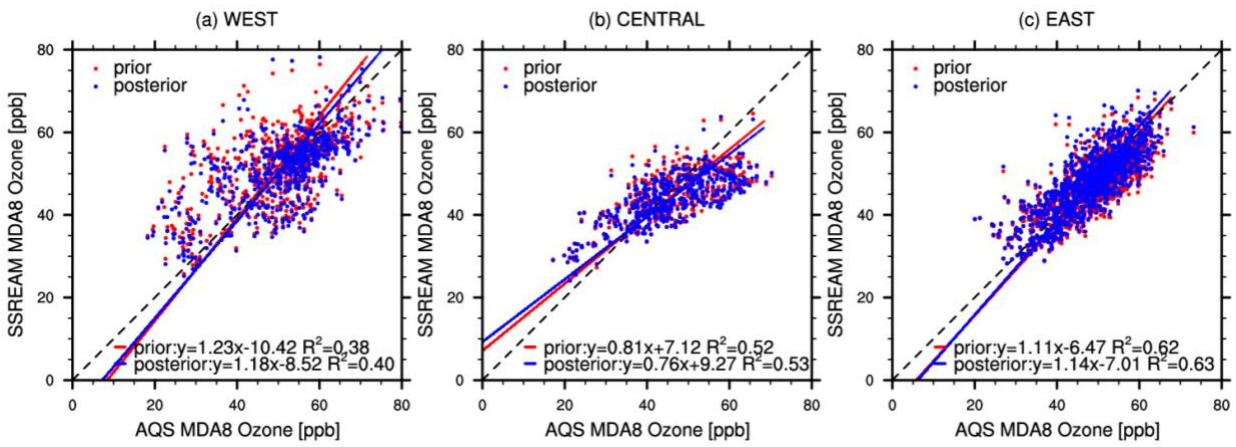

Figure 2.19 The relationship between observed AQS MDA8 ozone and simulated MDA8 ozone using prior and posterior emissions over the West, Central and East CONUS averaged for JJA 2011.

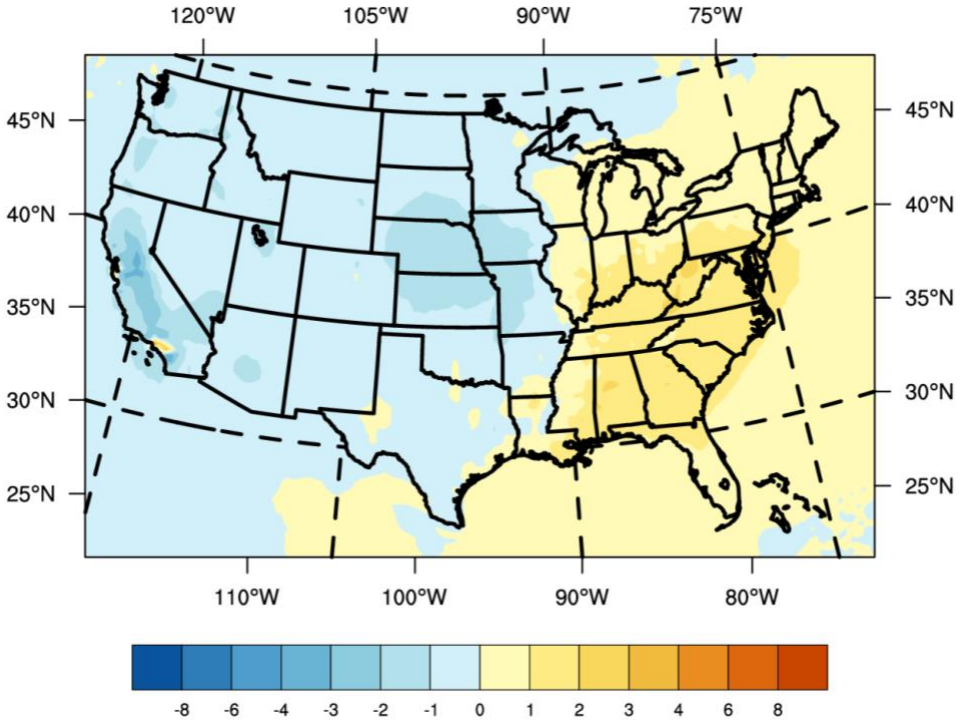

Figure 2.20 The difference of averaged MDA8 ozone between model simulations using the prior and the posterior emissions for JJA 2011.

CHAPTER 3. NOCTURNAL DECAY OF ISOPRENE DURING THE 2013 SOUTHERN OXIDANT AND AEROSOL STUDY (SOAS): EVALUATION AND IMPLICATIONS

3.1 Introduction

Isoprene, the most important biogenic volatile organic compounds (BVOCs) globally, accounts for about half of the BVOC emissions (~500 Tg yr-1) (Guenther et al., 2012). Its emission is highly light- and temperature-dependent with almost no emission at night (Sharkey, 1995). Isoprene can be quickly oxidized by hydroxyl radicals (OH), producing hydroxyperoxy radicals that drive ozone (O_3) and hydroxynitrates production in the presence of nitrogen oxides (NO_x) (Sillman et al., 1990). Despite large emission flux, only moderate concentrations (0-10 ppb) are observed even near emission sources due to the high reactivity of isoprene (von Kuhlmann et al., 2004).). Rapid oxidation of isoprene is a main driver of the atmospheric chemistry over forest region like southeast United States, which has important impact on ozone and secondary organic aerosol (SOA) formation (Xu et al., 2015; Fisher et al., 2016; Travis et al., 2016;).

Generally, isoprene follows a marked diurnal pattern of a steady increase throughout the morning and decrease in the afternoon due to reduced emissions and rapid oxidation of OH. Many field studies observed an accumulation of isoprene in the early evening with a decline after sunset and some production of organic nitrates at night (Starn et al., 1998; Hurst et al., 2001; Stroud et al., 2002). Previous studies credited the nighttime decay of isoprene to nitrate radicals (NO_3) oxidation with cases of high NO_x emissions

(Brown et al., 2009; Millet et al., 2016) or forest regions susceptible to high NO_x transport events (Starn et al., 1998). Nitrate radicals, generated from NO_2 reacting with O_3, can be abundant at night and rapidly photolyzed during the day. However, in high-NO environments, it is possible that isoprene is accumulated at night and causes a late-morning ozone peak (Millet et al., 2016), when rapid NO_3 titration by NO significantly suppress NO_3 levels (Aliwell and Jones, 1998). NO_3 oxidation of isoprene is relatively fast (τ = 20 min at [NO_3] = 50 ppt) compared with O_3 oxidation (τ = 30 hr at [O_3] = 30 ppb) during night (Atkinson et al., 2006). Yields of isoprene nitrates (INs) through NO_3 pathway are about 62%-78% (Rollins et al., 2009). These INs can form secondary organic aerosols (SOA) and be a reservoir of NO_x, which are transported to downwind cities and release NO_x back when sunlight comes in, further impacting on next day O_3 concentration.

However, there are alternative explanations for nocturnal decay of isoprene if there is low NO_x impact over forest regions with high isoprene emissions. During daytime, isoprene emits directly from trees near the surface exhibiting a sharply decreasing vertical profile (Andronache et al., 1994; Guenther et al., 1996). When emissions of isoprene are shut down after sunset, high isoprene concentrations at surface could be vertically dispersed to higher levels (Makar et al., 1999). Reaction with OH is also worth attention because high nighttime OH could account for a significant part of the observed decrease in isoprene at night (Hurst et al., 2001). Another possible explanation is that, during daytime, lifetime of isoprene (about an hour) is much shorter than the travel time of fresh air from regions with less isoprene emissions, while, at night, fresh air could be gradually advected in when there is no newly emitted isoprene and cause a steady decrease of isoprene (Sillman et al., 2002).

This study is conducted at Centreville, Alabama, a rural region in the Southeast with substantial isoprene emissions and minor impact from anthropogenic pollution, resulting in a low NO_x (peaks at about 1.3 ppb) and high isoprene (ranges from 1 to 6 ppb) environment (Figure 3.3). Measurements show a consistent decay of isoprene at night during SOAS campaign, however, barely any previous studies explored the reason for this nighttime decay of isoprene. In this study, we use a 3-D Regional chEmical trAnsport Model constrained by SOAS observations at Centreville during summer 2013 to quantify impacts from chemical processes (OH, NO_3 and O_3 oxidation of isoprene) and transport (diffusion and advection) on nighttime decay of isoprene. Other secondary species produced from isoprene chemistry, such as MVK, MACR and gas-phase INs, are also examined in model-observation comparisons, in complement to isoprene, O_3, NO_x and OH analysis. Lastly, implications on current isoprene chemical mechanism constraint by measurements at Centreville during 2013 SOAS campaign could be demonstrated based on critical assessments of oxidation products of isoprene.

3.2 Data and methods

3.2.1 Field measurements

Ground observations were conducted a (32.9°N, 87.2°W) from June 1st to July 15th, 2013, as part of the SouthEastern Aerosol Research and Characterization (SEARCH) network. It is a rural site surrounded by a dense mixed forest of pine and broadleaf species where isoprene is the dominant BVOC emissions with a molar fraction of 82% (Xu et al., 2015) during the day. This site is subject to low pollution but could experience occasional influences by aged air masses from nearby southern metropolitan cities, power plants, and

traffic on roads (Feiner et al., 2016). Surface meteorological conditions were collected by Atmospheric Research and Analysis (ARA) as part of SEARCH. Conditions are favorable for the formation of air pollution with days of high relative humidity, high solar radiation, light winds, and nocturnal temperature inversion in the boundary layer (Hidy et al., 2014). In the morning, the inversion layer breaks up and draws pollutions aloft down to the ground. Occasional wind events could disperse pollutants across regions, thus decrease the surface concentrations and above. We binned all observations to one-hour intervals to compare with our model simulations.

During SOAS campaign, chemical measurements are mostly obtained from a walk-up tower with about 20m height and 10m above the canopy. Isoprene was measured by a proton-transfer-reaction time-of flight mass spectrometer (PTR-ToF-MS) with 10% uncertainty. O_3, NO and NO_2 collected by ARA have corresponding uncertainties of 5%, 3% and 3% (Hidy et al., 2014). O_3 was detected from UV absorption at 254nm, while NO and NO_2 are measured by chemiluminescence detection (CLD) upon NO reaction with O3 and NO from ozone photolysis (Hansen et al., 2003). The OH was determined from chemical ionization mass spectrometry (CIMS) utilizing ambient pressure ionization as a reagent ion with an updated corona discharge ion source for the SOAS campaign (Kurten et al., 2011). The uncertainty of OH is about 40%, and the detection limit is 2×10^5 molecules cm^{-3} (Kim et al., 2015a). MVK and MACR were measured individually by gas chromatography coupled with mass spectrometry (GC-MS). PTR-ToF-MS was used to observe their sums due to possible line losses for oxygenated species in GC-MS measurements (Jordan et al. , 2009) with about 30% uncertainty. To reduce errors, analysis of GC-MS MVK and MACR are conducted, based on days, from June 18 to June 24, in

good agreement with PTR-ToF-MS sums (Figure 3.1). INs used in this study are composed of both first-generation INs, including β-hydroxyl INs and isomers, δ-hydroxyl INs and isomers, and nighttime carbonyl nitrates, and second-generation INs, further oxidized from the first-generation INs (methylvinylketone nitrate (MVKN), methacrolein nitrate (MACRN), propanone nitrate (PROPNN) and ethanal nitrate (ETHLN)) which observed by the Caltech CF3O− Time-of-Flight Chemical Ionization Mass Spectrometer (CIT-ToF-CIMS) with 20% errors (Crounse et al., 2006; Nguyen et al., 2015). Mass concentrations of speciated particle phase INs were determined by high-resolution chemical ionization time-of-flight mass spectrometer (HR-ToF-CIMS) using iodide-adduct ionization (Lee et al., 2014) with a filter inlet for gases and aerosols (FIGAERO), applying highest sensitivity of β-isomer isoprene hydroxy nitrate ($C_5H_9NO_4$) to calculate mass concentrations of all observed organic nitrates (Lopez-Hilfiker et al., 2014).

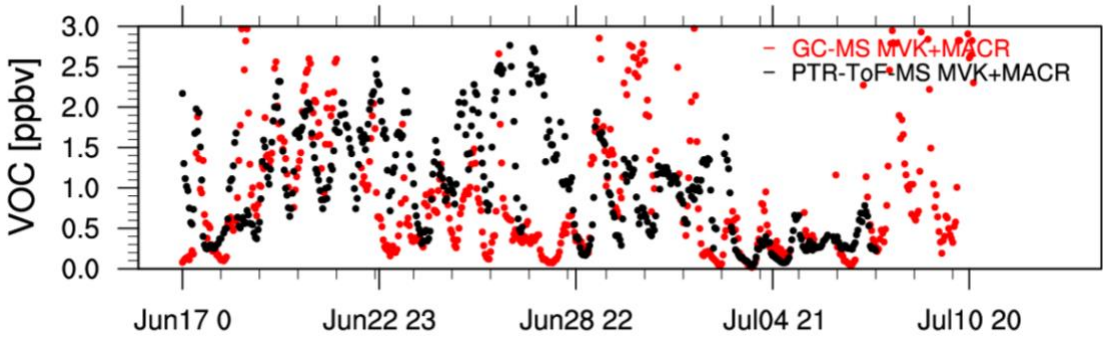

Figure 3.1 Time series of MVK and MACR sums observed by GC-MS (red) and PTR-ToF-MS (black) at Centreville during the 2013 SOAS campaign.

3.2.2 3D-REAM and isoprene oxidation chemical mechanism

3D-REAM, driven by hourly Weather Research and Forecasting (WRF, version 3.9) outputs constrained by the Climate Forecast System Reanalysis products (http://cfs.ncep. noaa.gov/cfsr), is used to represent and analyze observations. WRF reproduces the meteorological fields at Centreville during the SOAS campaign within the error range (Figure 3.2). Previous studies have applied REAM to conduct regional studies of tropospheric chemistry, vertical mixing and horizontal transport in the US and China (Choi et al., 2005, 2008a, b; Zeng et al., 2003; Zhao and Wang et al., 2009; Zhao et al., 2009, 2010; Liu et al., 2010, 2012a, 2012b;2014; Gu et al., 2013, 2014, 2016; Zhang et al., 2016, 2017; Li et al., 2019a, b; Qu et al., 2020). The model covers the CONUS, with a horizontal resolution of 36 km × 36 km and 30 vertical layers in the troposphere. The initial and boundary conditions are from a 2° × 2.5° global simulation using GEOS-Chem. We use a timestep of 5 min for transport and 60 min for chemistry in the simulation. Hourly anthropogenic emissions are estimated from 2011 National Emission Inventory (NEI2011) with a pronounced weekday-to-weekend cycle (Choi et al., 2012). Biogenic VOC emissions, driven consistently by WRF 3.9, are hourly computed by Model of Emissions of Gases and Aerosols from Nature (MEGAN) version 2.1 (Guenther et al., 2012). The chemical mechanism in REAM is adopted from a mini-Caltech isoprene mechanism (Mini-CIM) with updated isomer distributions of isoprene peroxy radicals instead of single lumped isoprene peroxy radicals in previous GEOS-Chem v11-02c chemical mechanism, increased OH regeneration especially in low-NO pathways, higher MVK to MACR ratio, better representation of SOA precursors and more efficient NO_x transition to inorganic nitrates detailed described in the Bates et al. (2019) and Wennberg et al. (2018). The

deposition and SOA formation processes are based on GEOS-Chem v12.1.1 (Travis et al., 2016).

The fates of the INs include photolysis, oxidation, aerosol uptake with further hydrolysis, wet deposition, and dry deposition. Aerosol uptake followed by hydrolysis is a significant loss for gas-phase nitrates taking up more than half of the total loss (Fry et al., 2013; 2014). Because of the complexities of various formation pathways and limited constraints on accurate OA concentration modeling, we consider a simple SOA scheme in this study (Pai et al., 2020). Uptake coefficients (ɣ) used in REAM, providing a sufficient irreversible sink for gas-phase INs. Assumptions have been made in REAM that ɣ = 0.05 for first generation INs and ɣ = 0.005 for MACRN and MVKN, constraint to match the measurements. Because PROPNN and ETHLN are extremely less soluble due to lack of hydroxyl groups, aerosol uptakes of both PROPNN and ETHLN are not considered in our simulation. As there is no aerosol module in REAM, we assume a bulk lifetime of 20 min for hydrolysis process to estimate particle-phase INs. At night, isoprene reacts mainly with NO_3 to form a nitrooxy peroxy radical, subsequently reacting with NO, NO_3, itself and other peroxy radicals to form nighttime INs. For second-generation INs, the majority of MVKN and MACRN are coming from β-pathway, while PROPNN and ETHLN are from δ-pathway and nighttime NO_3 initiated oxidation of isoprene (Lee et al., 2014).

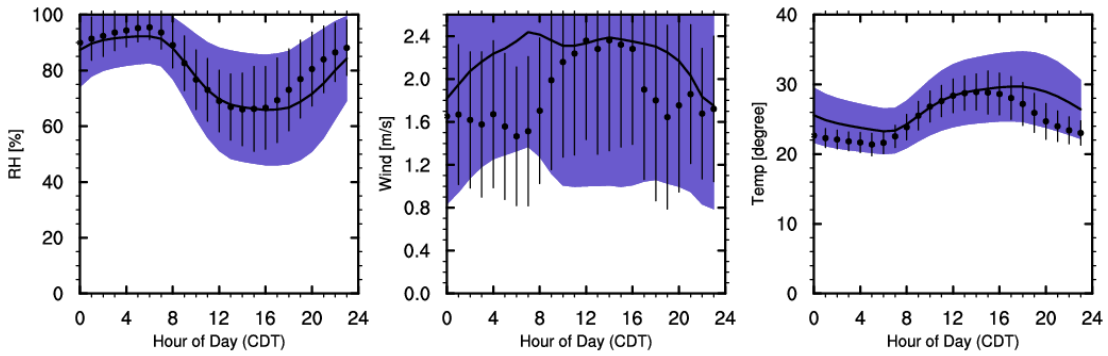

Figure 3.2 Observed (dots) and WRF (solid line) mean diurnal cycles of relative humidity (Left), wind speed (Middle) and temperature (Right) at Centreville during the 2013 SOAS campaign. Blue shadings represent the WRF data uncertainties. The vertical bars are standard deviations of the measurements.

3.3 Results and discussion

3.3.1 Loss of isoprene at night

Figure 3.3 shows that the observed and REAM simulated diurnal variabilities of isoprene, related tracer gases and OH radicals averaged during the SOAS campaign are basically in good agreement. Model reproduces the diurnal change of isoprene compared to measurements at Centreville, which peaks during midafternoon and generally drops during nighttime. The sun sets between 7:50 pm to 8:00 pm and rises between 5:35 am to 5:50 am at Centreville during the 2013 SOAS campaign. In this study, we consider the time period, 8:00 pm to 5:00 am, as the nighttime. Isoprene decays around 4:00 pm in the model, nevertheless, for observed cases, it sharply falls out after 7:00 pm, coinciding with sunset times. It could be explained by the overestimation of OH during 4:00 pm to 7:00 pm in the model as daytime isoprene chemistry is OH-driven. Isoprene gradually decays until 5:00 am in the morning, when sun rises and brings back isoprene emissions and OH concentrations. After sunset, there are barely any isoprene emissions, and only small

portion of isoprene will persist into night due to its short lifetime. Since OH are extremely low at night, some previous studies attributed nighttime decay of isoprene to NO_3, formed by reaction of NO_2 with O_3, due to the accumulation of NO_3 at night and its relatively fast isoprene oxidation rate (Brown et al., 2009; Millet et al., 2016). At Centreville, nighttime OH concentrations are low but not completely reaching zero, with observed values around detection limit of 2×10^5 molecules/cm^3. The nighttime OH could come from oxidation of VOC initiated by NO_3 (Platt et al., 1990) and reactions of VOC with O_3 (Atkinson and Aschmann, 1993). The simulated NO_x captures observation well, while REAM tends to overestimate nighttime surface ozone. It suggests limit titration of ozone with NO in the model (Sharma et al., 2017). The isoprene measurements show no significant peaks in late afternoon and early evening compared to previous studies (Millet et al., 2016), instead a gradually consistent decay occurs shown in Figure 3.3. Here, we explored this nocturnal decline of isoprene during 2013 SOAS campaign at Centreville within the frame of chemical and physical processes.

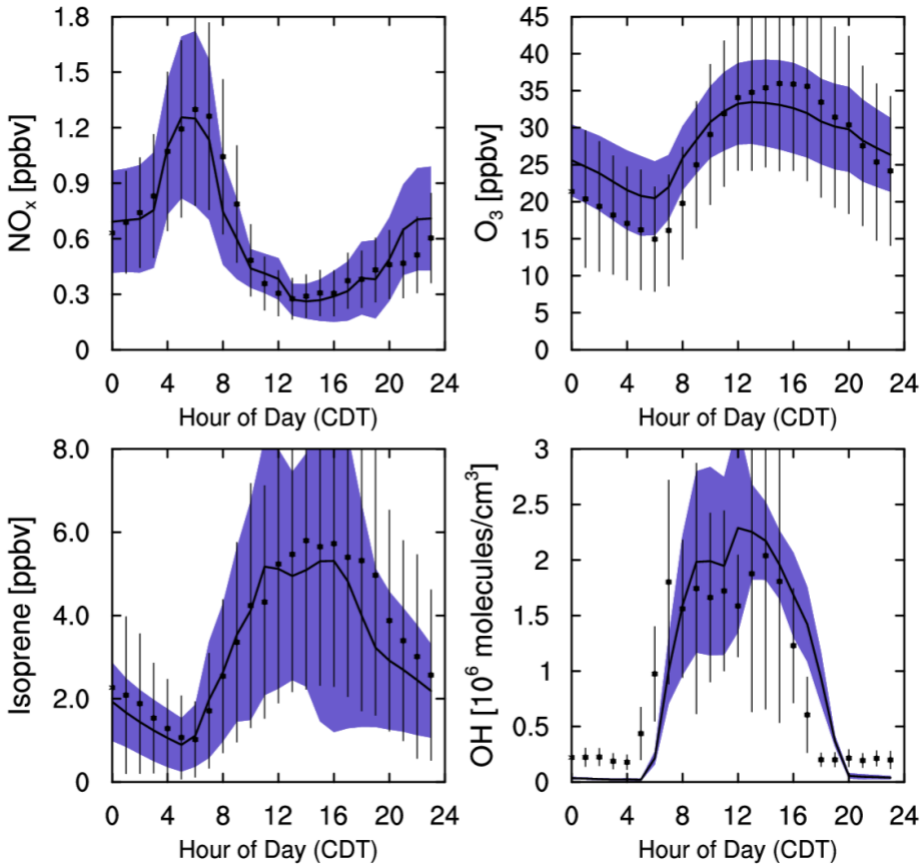

Figure 3.3 Observed (dots) and modeled (solid line) mean diurnal cycles of NO_x, O_3, isoprene and OH at Centreville during the 2013 SOAS campaign. Blue shadings represent the model uncertainties. The vertical bars are standard deviations of the measurements.

In Figure 3.5, we show nighttime evolutions of chemical and physical loss rates of isoprene from 8:00 pm to 5:00 am averaged during the 2013 SOAS campaign in REAM. Emissions of isoprene are highly light dependent and reach zero at night. Three possible oxidation pathways of isoprene are OH, NO_3 and O_3. Ozone is the most abundant oxidant compared to OH and NO_3. However, the reaction rate of ozone with isoprene is relatively slow (τ = 30 hr at [O_3] = 30 ppb), which explains its moderate impact on isoprene. During

daytime, the photochemical reactions convert O_3 precursors into O_3. At night, O_3 levels are removed by chemical reactions with NO and NO_2, and dry deposition. In terms of the low concentrations of NO and NO_2 at Centreville (Figure 3.11), O_3 concentrations are relatively high compared to polluted city environments. Ozone oxidation dominates the chemical loss of isoprene at night shown in Figure 3.5, consuming as much as 50% more isoprene than OH or NO_3 radicals. Isoprene loss through ozonolysis shows a decreasing trend, consistent with the overnight chemical and physical consumption of O_3 concentrations which reach the minimum right before the sunset. The dominant removal mechanism of isoprene during daytime is the OH oxidation with fast reaction rates ($\tau \sim 1$ h at [OH] = 2.5×10^6 molecules/cm^3) (Atkinson et al., 2006). OH radicals are generated via photolysis of ozone and HCHO (Crutzen and Zimmermann, 1991). The levels of OH radicals are decreasing with reduced radiation after noon and are not completely depleted at night without sunlight. Instead, small amounts of OH, about 2.5×10^5 molecules/cm^3 observed at Centreville, are generated either by ozonolysis of alkenes or through nitrate radical initiated chemistry leading to the formation of HO_2 radicals, which are then converted to OH (Platt et al., 1990; Atkinson and Aschmann, 1993). Although isoprene reacts fast with nitrate radicals, they are not major sinks of isoprene during daytime due to fast photolysis. In absence of sunlight, NO_3 oxidation of isoprene should be considered. During the early evening, from 8:00 pm to 10:00 pm, isoprene depleting from OH oxidation exceeds that through NO_3 pathway. As night proceeds, the buildup of NO_3 radicals (Figure 3.11) by reaction of NO_2 with O_3 makes NO_3 oxidation play a more important role than OH oxidations and show comparable importance as the O_3 oxidation in the early morning.

Transport processes including advection and vertical mixing, are also suggested physical mechanism to explain the nighttime decay of isoprene. The dry deposition of isoprene is not considered as a possible loss pathway because isoprene is a nonpolar species (Hurst et al., 2001). Advection of air parcels with less isoprene to this ground site decreases isoprene at night. The average southerly wind shown in Figure 3.7 bring in air masses with insignificant amount of isoprene from Gulf of Mexico to Centreville. Corresponding increase of isoprene downwind Centreville further supports the possibility of advection at night. Vertical mixing is another possibility of isoprene decay, where low-isoprene air aloft is mixing down. Isoprene exhibits strong vertical gradient from surface to 500m shown in Figure 3.12 because of its surface emissions and rapid consumption by OH (Trainer et al., 1987). In the model, the magnitude of vertical mixing is depicted by the diffusion coefficient (K_{zz}), which are based on the WRF outputs and adjusted to match the observations following the method of Li et al. (2021). Better agreements between modeled and observed boundary layer height compared to WRF outputs (Figure 3.4) validate that the REAM captures the nighttime vertical mixing processes. Good capture of nighttime vertical mixing processes in the REAM can be also validated by the good agreements between observed and simulated NO_x levels. In Figure 3.5, we find that depletion from advection is comparable to that from diffusion at night. Diffusion impact on isoprene change drops at early evening and gradually increases in consistent with the vertical gradients of isoprene at surface (Figure 3.12). We find that the decay of isoprene transits from chemical oxidation driven to the transport process driven at around 11:00 pm. Fresh isoprene-depleted air from aloft and upper wind then continuously dilutes in over the night with an average loss of isoprene is around 0.13 ppb/h from 8:00 pm to 5:00 am, with

chemical loss rate of 0.12 ppb/h and a total of 0.25 ppb/hr. The average lifetime of isoprene at Centreville at night is estimated to be 8.0 hours and about 15.9 hours for advection processes.

We quantify the total loss of isoprene through all possible pathways in the model overnight at Centreville averaged during the 2013 SOAS campaign in Figure 3.6. About half of the nighttime isoprene removal attributes to transport (51.7%), competing with chemical terms (48.3%). The diffusion and advection share similar contribution to the nighttime isoprene decay, 26.8% and 24.8%, respectively. Ozone oxidation contributes to 24.4% of the total isoprene decay, consuming 0.6 ppb of isoprene, which is respectively 50.1% and 51.5% more than NO_3 and OH oxidation. 12.2% of isoprene decay at Centreville is arise from the NO_3 oxidation, comparable to 11.8% OH oxidations.

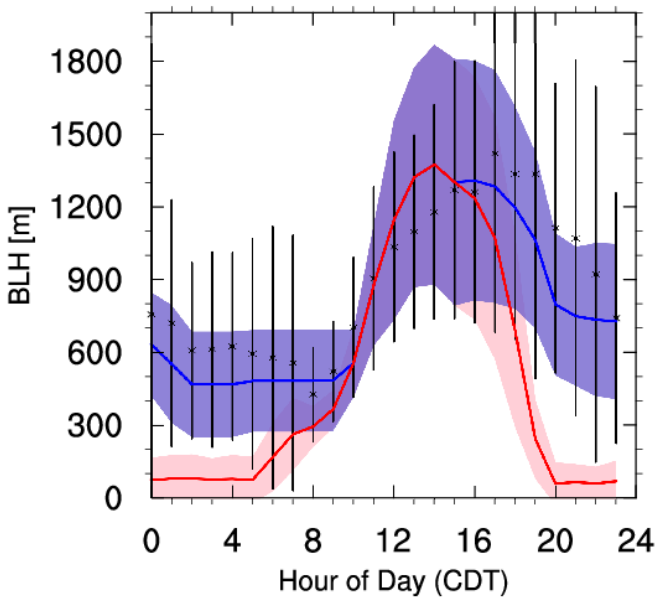

Figure 3.4 Observed (dots), WRF (solid red) and K_{zz}-adjusted (solid blue) mean diurnal cycles of boundary layer height (BLH) at Centreville during the 2013 SOAS campaign. Shadings represent the WRF (red) and Kzz-adjusted (blue) BLH uncertainties. The vertical bars are standard deviations of the measurements.

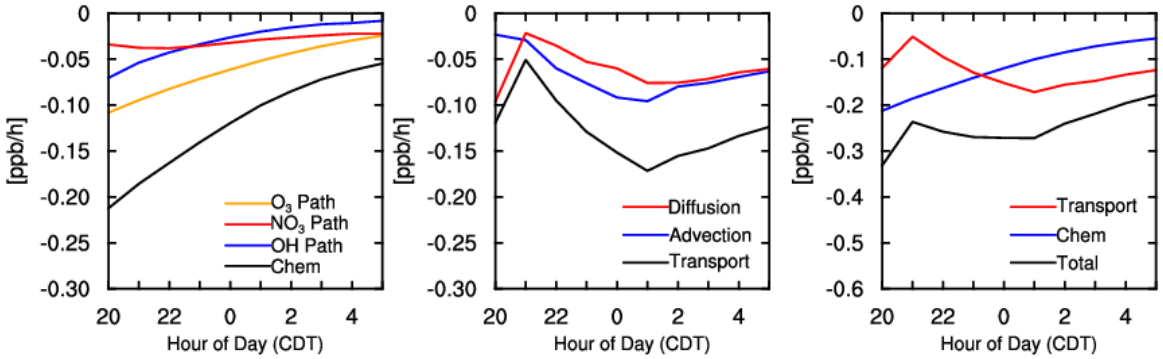

Figure 3.5 Time series of nocturnal isoprene mean hourly change through chemical processes (O_3, NO_3 and OH oxidation) and transport processes (diffusion and advection) from 8:00 pm to 5:00 am at Centreville during the 2013 SOAS campaign.

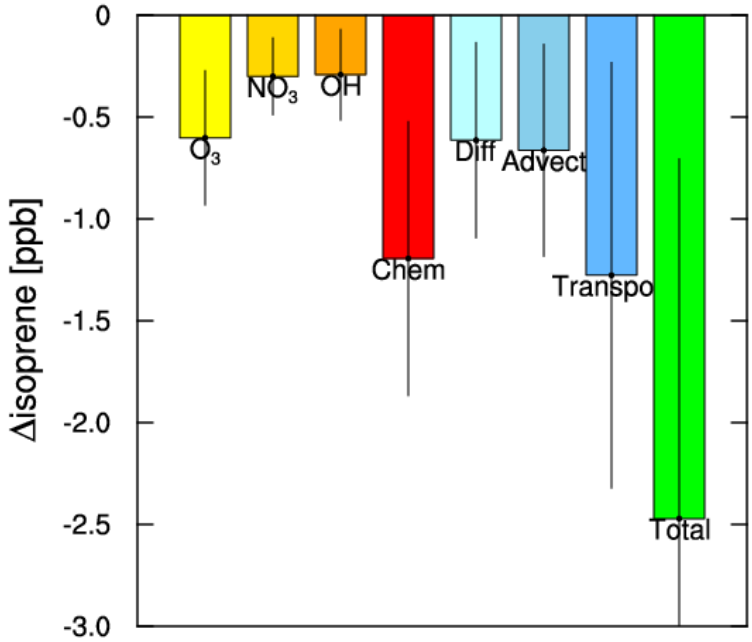

Figure 3.6 Total mean nocturnal isoprene changes through chemical processes (O_3, NO_3 and OH oxidation) and transport processes (diffusion and advection) from 8:00

pm to 5:00 am at Centreville during the 2013 SOAS campaign. The vertical bars are standard deviations of the model results.

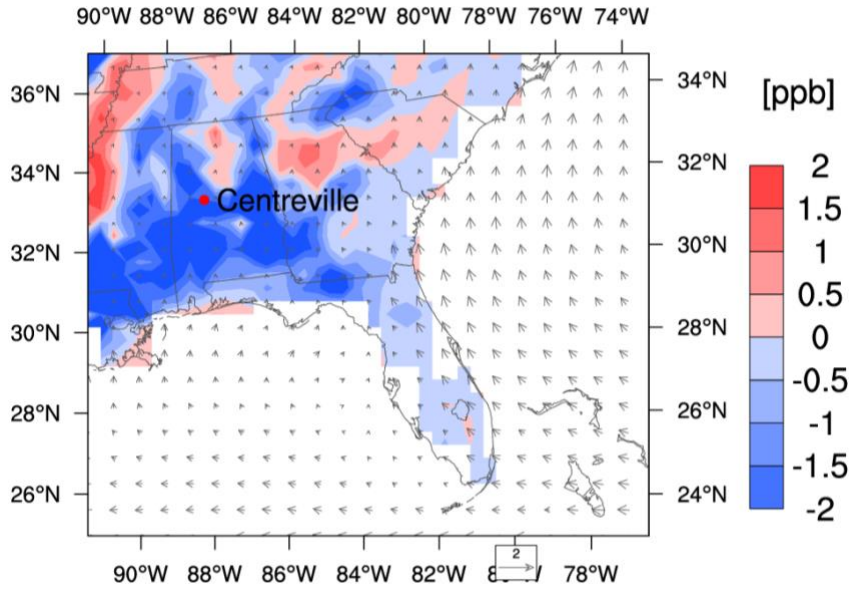

Figure 3.7 The distribution of total nighttime isoprene changes (from 8:00 pm to 6:00 am CDT), overlayed by the averaged wind field, in the Southeast averaged during the 2013 SOAS campaign. The red dot is the observation site Centreville.

3.3.2 first-generation oxidation products of isoprene

Methyl Vinyl Ketone (MVK) and methacrolein (MACR) are both major first-generation oxidation products of isoprene from multiple pathways. They serve as important tracers of isoprene chemistry with high yields from OH and O_3 oxidations (Tuazon and Atkinson, 1990; Paulson et at., 1992; Liu et al, 2013; Jenkin et al., 2015), variant with different NO condition (Jenkin et al., 2015). Approximately, 3.5% of MVK and MACR are produced in the NO_3 pathway (Wennberg et al., 2018). Therefore, we explore the diurnal cycle of MVK and MACR as the additional criteria to test the nocturnal isoprene decay. In Figure 3.8, we find that REAM shows overestimations of MVK and MACR using mini-CIM mechanism compared to observations. It can be explained by the

underestimation of dry deposition in the model as we increased the dry deposition velocity of MVK and MACR by factor of 4 in Figure 3.13 and found perfect matches with observations during late afternoon and night. Figure 3.17 shows that no significant changes of isoprene, OH, ozone and NO_x levels are found with increased MVK and MACR dry deposition velocities. The late afternoon peak hours of MVK and MACR are not captured by the model, instead the peaks of MVK and MACR are consistent with the isoprene peak around 12:00 pm to 4:00 pm, coinciding production from OH oxidation of isoprene in the model. The lower than model concentrations and relative flat trends of MVK and MACR during daytime suggest that in the model either the productions of MVK and MACR are overestimated, or slower sinks compared to OH oxidation are missing.

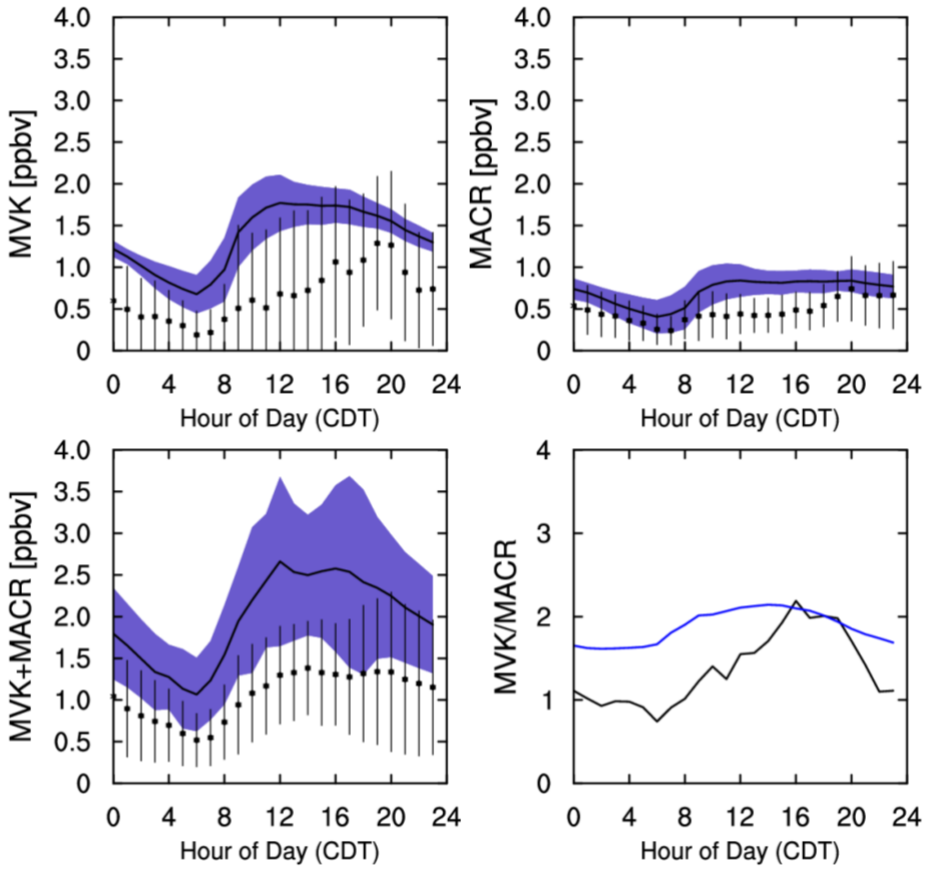

Figure 3.8 Observed (dots) and modeled (solid line) mean diurnal cycles of MVK, MACR and MVK+MACR at Centreville during the 2013 SOAS campaign. Blue shadings represent the model uncertainties. The vertical bars are standard deviations of the measurements. The lower right figure is the observed (solid black) and simulated (solid blue) ratio of MVK and MACR.

Because MVK and MACR are less reactive species and longer-lived than isoprene, we used the ratio of first oxidation products of isoprene (MVK/MACR) as a proxy to estimate the oxidation of isoprene. Isoprene ozonolysis reaction results in a MVK to MACR ratio of 0.41 (Montzka et al., 1993) but MVK reacts faster with O_3 than MACR (Carter and Atkinson, 1996), so a concentration ratio slightly less than 0.41 would be expected from pure ozonolysis reactions at steady state. Similarly, the ideal yield ratio of

MVK to MACR is approximately equal to 1.4 considering only the OH pathway. MACR reacts faster with OH than MVK, which induces the ratio of MVK to MACR to be around 2.0 in OH term (Carter and Atkinson, 1996). Figure 3.8 shows that the ratios of MVK to MACR are overall reproduced in the model in the range of 1 to 2 using mini-CIM mechanism during daytime and have similar trends at night compared to measurements. The ratio gradually increases from 5:00 am and peaks at 4:00 pm at about 2.0 in both model and observations, implicating shifts from O_3-driven to OH-driven isoprene oxidations. The model captures the peak ratio of 2.0 when OH-oxidation is dominant, while the observed rapid change of MVK to MACR ratio in the early evening is not reproduced by the model when OH levels are rapidly dropping, and ozonolysis becomes important. This reflects the relative yield of MVK to MACR from the O_3 oxidation pathway of isoprene in the model could be overestimated. After sunset, ratios of MVK to MACR change slightly and show the fairly constant ratio after midnight in the model, suggesting the nighttime isoprene decay has changed from chemical to transport driven processes, in support of the trends shown in Figure 3.5. The nocturnal boundary layer can be stratified with significant vertical gradients and mix down more photochemically aged air aloft. The vertical profiles of MVK and MACR in the model are shown in Figure 3.14. The gradients of MVK and MACR are less steep and have slightly inversion near surface because of their relative longer lifetime than isoprene and secondary production from isoprene, leading to slower decay rate of vertical mixing. However, the similar decay rates of surface MVK and MACR to isoprene implies the importance of advection in the transport process. The ratio of isoprene and MVK+MACR are also checked in Figure 3.15, representing the degree of oxidation,

similar flat nighttime trends are found in both observed and modeled values, which is in support of the importance of nighttime transport at Centreville during the SOAS campaign.

3.3.3 Isoprene nitrates and implications

First generation of INs are mainly formed by isoprene peroxy radicals reacting with NO. In this study, mini-CIM mechanism considers the changing distributions of isoprene-hydroxy-peroxy isomers from OH oxidation under different NO_x levels instead of lumping and using fixed isomer distributions. It is found that, on average, δ-isomers contribute 17 % of the total isoprene-hydroxy-peroxy reactivity in the Southeast (Bates et al., 2019), increased from 10% in previous GEOs-Chem mechanism (Fisher et al., 2016). First generation INs are yielded from β- and δ-branches ranging from 4% to 15% in previous studies (Chen et al., 1998; Chuong et al., 2002; Mao et al., 2013; Xiong et al., 2015). Here, 12% is assigned to δ-branches and 14% and 13% are recommended for two isomers of β-branches, (1,2)-isoprene-hydroxy nitrate and (4,3)-isoprene-hydroxy nitrate, respectively. Second generation INs are subsequently produced from further oxidations of isoprene-hydroxy nitrates to generate MVKN and MACRN, mainly from β-branches, and PROPNN and ETHLN, primarily from δ-branches. In the mini-CIM mechanism, updated isoprene-hydroxy-peroxy isomer distributions result in lower yield of methacrolein-derived nitrates and higher hydroxynitrates (Bates et al., 2019). Addition of NO_3 to isoprene produces substantial isoprene carbonyl nitrate, hydroxynitrates and hydroperoxy nitrate, which could also get further oxidized to form secondary nitrates. PROPNN is considered as a high-yield photooxidation product of INs from NO_3-initiated oxidation (Fisher et al., 2016).

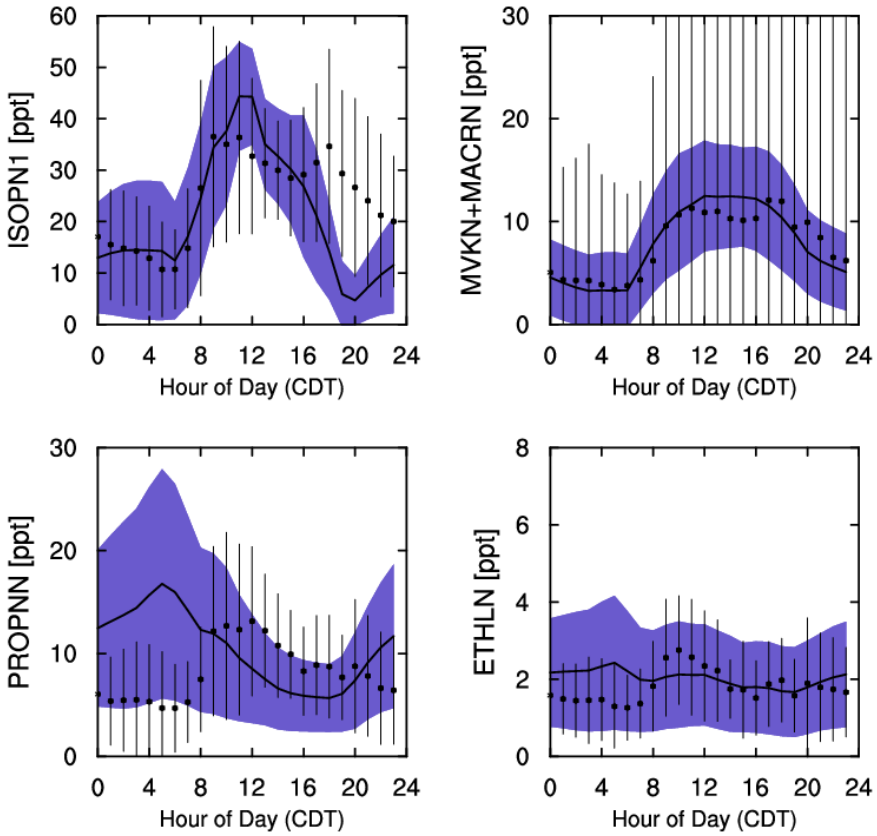

Figure 3.9 Observed (dots) and simulated (solid line) mean diurnal cycles of first-generation isoprene nitrates and second-generation isoprene nitrates (MVKN + MACRN, PROPNN and ETHLN) at Centreville during the 2013 SOAS campaign. Blue shadings represent the model uncertainties. The vertical bars are standard deviations of the measurements.

In Figure 3.9, it explicitly shows the modeled diurnal cycle of first generation of isoprene nitrates (ISOPN1: isoprene-hydroxy nitrates and carbonyl nitrate), MVKN, MACRN, RPOPNN and ETHLN in comparison with the SOAS CIT-ToF-CIMS measurements. In the model, we consider aerosol uptake coefficients for isoprene nitrates followed by irreversible hydrolysis sinks, except PROPNN and ETHLN which are less soluble. ISOPN1 peak at 11:00 am in the model, and steadily drop to a minimum of about

5 ppt around sunset. In the SOAS observation, there is another ISOPN1 peak at 6:00 pm and declines overnight. Model results are generally in agreement with observed diurnal cycles, except the missing second peak near dusk in the SOAS observations when isoprene chemistry shifts from OH-driven to O_3-driven. Because the photochemical lifetimes of ISOPN1 are short (Lee et al., 2014), it is implausible that ISOPN1 generated from elsewhere are transported to this site during late afternoon. The missing second peak of ISOPN1 near dusk in the model, coinciding with MVK and MACR diurnal profiles, imply that either there are missing sources of ISOPN1 or poorly understood sinks of ISOPN1 related to the uncaptured processes of isoprene chemical mechanism, especially in transition from OH-driven to O_3-driven oxidation of isoprene. After midnight, modeled ISOPN1 concentrations are generally consistent with the measurements. For second generation of isoprene nitrates, MVKN, MACRN, RPOPNN and ETHLN are explicitly measured at Centreville during the 2013 SOAS campaign. Figure 3.9 shows that model have better simulations of MVKN and MACRN than PROPNN and ETHLN, compared with CIT-ToF-CIMS measurements. Model tends to capture the diurnal variability of MVKN and MACRN, which peak at midday and steadily decrease then with a minimal concentration of 4 ppt. However, PROPNN and ETHLN are barely reproduced in the model, with early peaks at sunrise, and continuously decreasing during daytime until sunset. Model overestimates PROPNN and ETHLN at night and underestimates during the day, suggesting that PROPNN production in the mini-CIM mechanism are mainly from nighttime NO_3-initiated isoprene chemistry, accumulated overnight and then tend to get consumed during the day. The observed diurnal cycle of PROPNN and ETHLN on the other hand reflects that more daytime production of PROPNN and ETHLN from oxidation

of δ-isoprene-hydroxy nitrates and less nighttime PROPNN and ETHLN production from NO_3-initiated isoprene chemistry are expected. It infers that the distribution of β- and δ-branches and yields from NO_3-branches of isoprene chemical mechanism could still be problematic in the model.

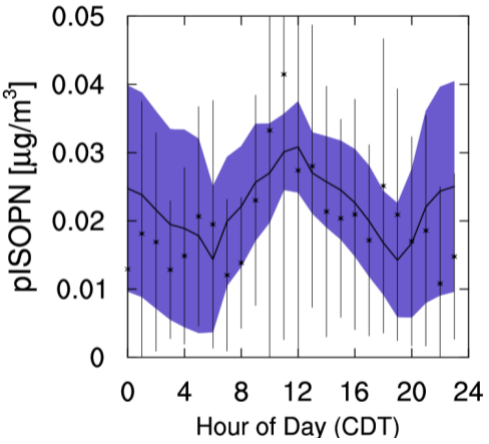

Figure 3.10 Observed (dots) and simulated (solid line) mean diurnal cycles of particle phase isoprene nitrates at Centreville during the 2013 SOAS campaign. Blue shadings represent the model uncertainties. The vertical bars are standard deviations of the measurements.

We also compared the modeled diurnal cycle of particle-phase isoprene nitrates (pINs) to the SOAS observations at Centreville. The FIGAERO HRToF-CIMS identified 88 speciated particle-phase organic nitrates (pONs). Here, the sums of all C5 pONs are assumed to represent the observed pINs. In the model, we assumed the simplified processes of aerosol partition, where gas phase isoprene nitrates form pINs on aerosols with presumed constant uptake coefficients, constrained by gas-phase observations, except PROPNN and ETHLN which are less soluble. We then assume a bulk lifetime for pINs, encountering hydrolysis to form HNO_3. As assumptions in the model are preliminary, which could result in biases in modeled pINs. Figure 3.10 shows that pINs peak at around

11:00 am and then form a second peak in the late afternoon in the observation, coinciding with gas-phase INs (ISOPN1+MVKN+MACRN) observations. Modeled pINs generally capture the diurnal variation of the SOAS Centreville observations. We find decay of pINs levels at night. But the early morning peak of pINs is barely captured, indicating biases from homogeneous uptake coefficients and bulk lifetime assumed in the model and other complicated processes not considered in this simplified aerosol formation model.

At Centreville, we find that only 12.2% of isoprene is consumed by NO_3 oxidations and more than half of the isoprene undergoes transport at night. Area downwind Centreville undergoes 1-1.5 ppbv increase of isoprene overnight. Transported isoprene could drive photochemistry and ozone production during the early morning (Millet et al., 2016) and cause an increase on the next day ozone levels. Methyl Vinyl Ketone (MVK) and methacrolein (MACR) are both major first-generation oxidation products of isoprene. The ratio of MVK and MACR is used as a proxy of isoprene chemistry. Constant ratios at night further supports the transport as the cause of nighttime decline of isoprene. Though model generally captures the diurnal cycle of MVK and MACR, the late afternoon peaks in both species are not captured, suggesting either the productions of MVK and MACR are overestimated, or slower sinks compared to OH oxidation are missing during this transition period of OH-driven to O_3-driven isoprene oxidations. Similar cases are found with the missing peaks of INs, such as ISOPN1 and MVKN+MACRN, at dusk, which further emphasizes the unknown isoprene oxidation processes in the model mechanism during this transition period. INs, mostly formed from isoprene chemistry of OH and NO_3 oxidations, are parts of NO_x reservoirs and SOA precursors. INs are sensitive to NO_x levels, showing rapid decrease with increasing NO_x emissions (Fisher et al., 2016). pINs could be

subsequently formed from INs, undergoing aerosol uptake and hydrolysis, releasing HNO_3 back, impacting the NO_x budgets (Lee et al., 2016). Better model mechanism of isoprene oxidation from OH-driven to O_3-driven transition period and elucidation of formation and loss of pINs are needed in the future to accurately quantify the impacts of isoprene chemistry on the NO_x budgets and SOA formations.

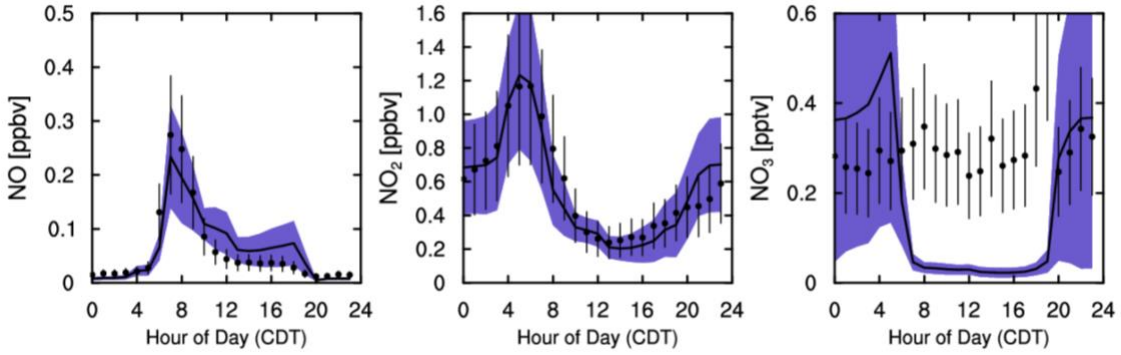

Figure 3.11 Observed (dots) and modeled (solid line) mean diurnal cycles of NO, NO_2 and NO_3 at Centreville during the 2013 SOAS campaign. Blue shadings represent the model uncertainties. The vertical bars are standard deviations of the measurements.

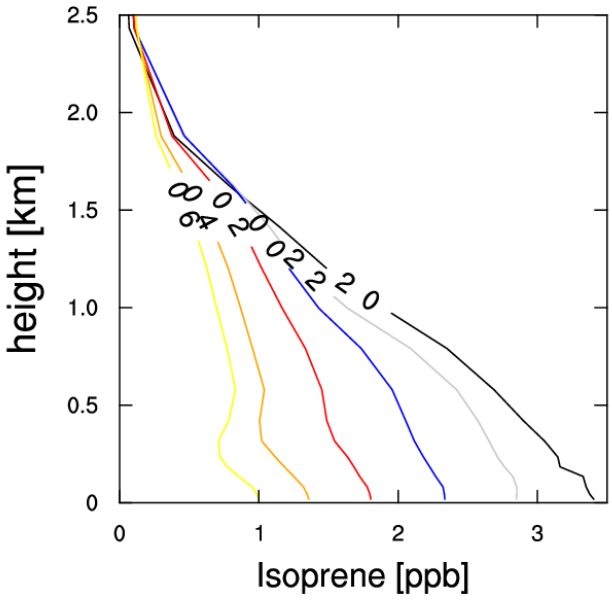

Figure 3.12 Modeled (solid line) mean vertical distribution of isoprene at Centreville during the 2013 SOAS campaign from 8:00 pm to 6:00 pm every two hours (in different colors).

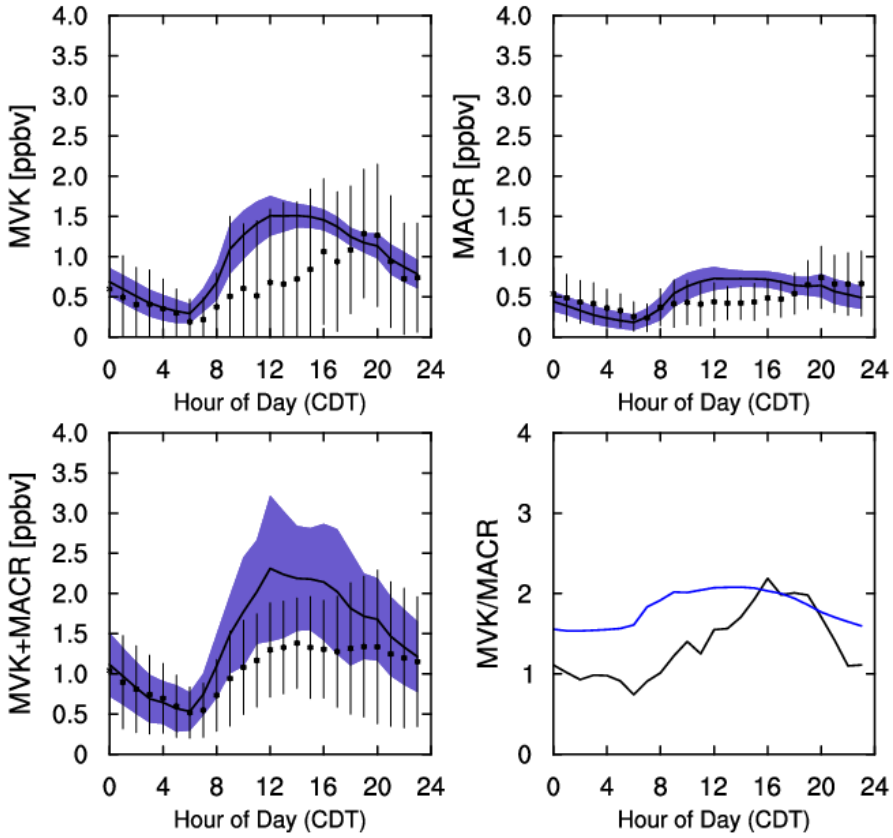

Figure 3.13 Observed (dots) and simulated (solid line) with 4 times deposition velocities of MVK, MACR and MVK+MACR at Centreville during the 2013 SOAS campaign. Blue shadings represent the model uncertainties. The vertical bars are standard deviations of the measurements. The lower right figure is the observed (solid black) and simulated (solid blue) ratio of MVK and MACR.

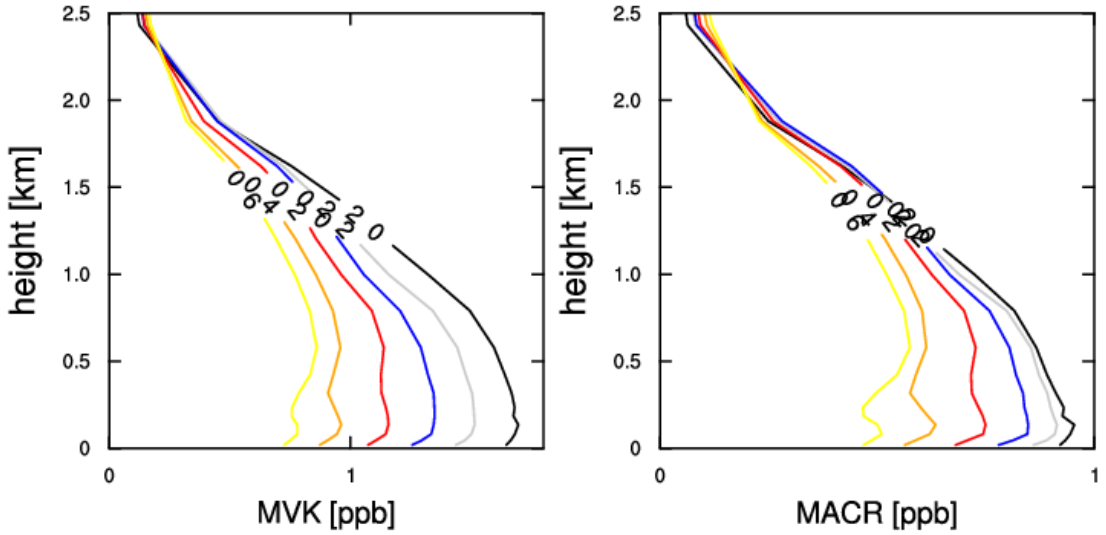

Figure 3.14 Modeled (solid line) mean vertical distribution of MVK and MACR at Centreville during the 2013 SOAS campaign from 8:00 pm to 6:00 pm.

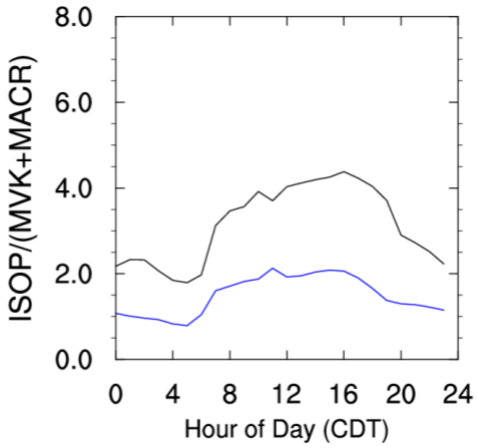

Figure 3.15 The observed (solid black) and simulated (solid blue) ratio of isoprene and MVK + MACR at Centreville during the 2013 SOAS campaign.

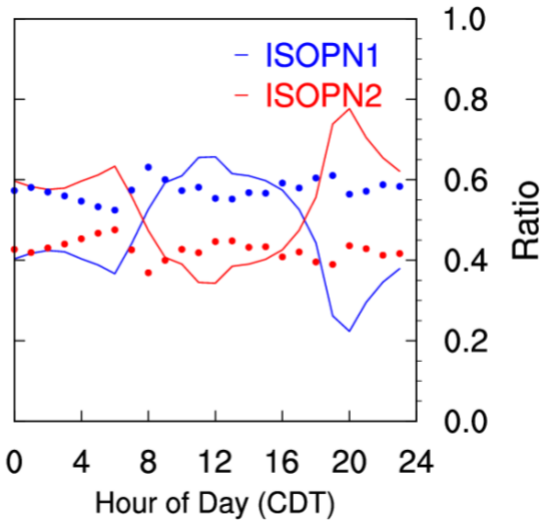

Figure 3.16 Observed (dots) and modeled (solid line) mean diurnal cycles of the contribution of first-generation isoprene nitrates (blue) and second-generation isoprene nitrates (red) to the total isoprene nitrates at Centreville during the 2013 SOAS campaign.

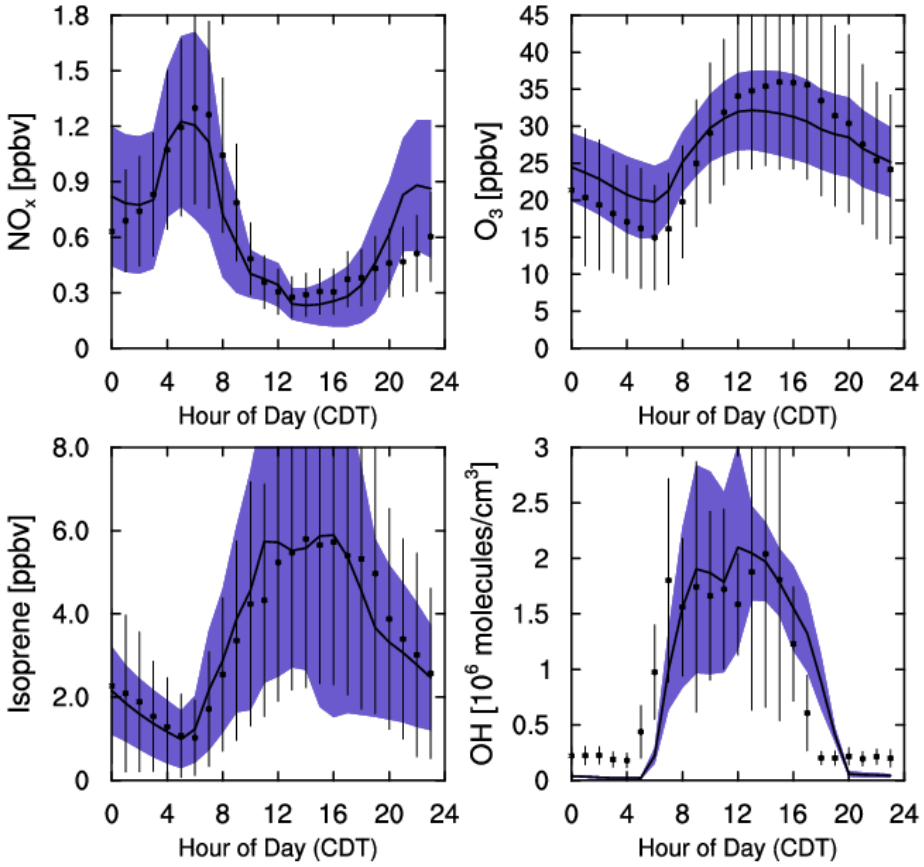

Figure 3.17 Observed (dots) and modeled (solid line) mean diurnal cycles of NO_x, O_3, isoprene and OH with 4 times deposition velocities of MVK, MACR at Centreville during the 2013 SOAS campaign. Blue shadings represent the model uncertainties. The vertical bars are standard deviations of the measurements.

CHAPTER 4. SUMMERTIME CLEAN-BACKGROUND OZONE CONCENTRATIONS DERIVED FROM OZONE PRECURSOR RELATIONSHIPS ARE LOWER THAN PREVIOUS ESTIMATES IN THE SOUTHEAST UNITED STATES

4.1 Introduction

"Surface-level" ozone is regulated by the National Ambient Air Quality Standards (NAAQS) in the United States (EPA, 2015). Summer is the season of high ozone concentrations in polluted regions although the ozone season can expand beyond summer as a result of climate change (Zhang et al., 2016). In the past several decades, the Clean Air Act Amendments and their enforcement have led to large reductions of anthropogenic emissions of nitrogen oxides ($NO_x = NO + NO_2$) and volatile organic compounds (VOC). However, summertime ozone concentrations over large regions of western United States (excluding California) have insignificant and even a small increasing trend in contrast to significant decreases over the eastern United States and California (Cooper et al., 2012; Simon et al., 2014; Lin et al., 2017). One potentially contributor is an increase of background ozone concentrations in the West (Lin et al., 2017). However, some of the uncertainties in defining regional ozone background were extensively discussed in the earlier works by Fiore et al. (2002, 2003) and were subsequently analyzed (Zhang et al., 2011; Lin et al., 2012; Emery et al., 2012; Fiore et al., 2014; Lefohn et al., 2014; Dolwick et al., 2015). The recent assessments by Jaffe et al. (2018) again emphasized the significant contributions and large uncertainties of background ozone.

There are many approaches to reduce the uncertainties of model-simulated background ozone, including modeling process-level intercomparison exercises and improving emissions, physical and chemical processes in the model. Ultimately, however, observation-based background ozone estimates will be needed as the ground-truth. We note that the analyses of remote and background ozone sites (Altshuller and Lefohn, 1996; Vingarzan, 2004) are for what Cooper et al. (2015) termed "baseline" ozone, which includes ozone produced from North American emissions. The "baseline" ozone, therefore, is higher than the background ozone. Other attempts to estimate background ozone have been made using the relationships between ozone and its precursors. Given the important role of NO_x in ozone photochemical production and the previously found dependence of ozone on NO_x and NO_y to derive ozone production efficiency (OPE) values (Lin et al., 1987; Kleinman et al., 2002), it is not surprising that the relationships of ozone with NO_z (defined as total reactive nitrogen (NO_y)-NO_x ($NO+NO_2$)) were explored to define background ozone (Altshuller and Lefohn, 1996; Hirsch et al., 1996) by extrapolating the O_3-NO_z linear regression line to the 0-value point of NO_z, the corresponding ozone value presumably represents a background value (hereafter referred to as the O_3-NO_z method).

Background ozone is not a well-defined term (Jaffe et al., 2018). If a location is downwind from a polluted urban region, transported high ozone concentrations can be considered as a background or "baseline" ozone level for the site (Fiore et al., 2002; Trainer et al., 1993). Using the type of operational definition, background ozone concentrations would vary depending on the applications and are therefore difficult to compare among different studies. For example, if we extend from one site to a region, the influence from the upwind city emissions would vary with time and location in the region. In this case,

defining a clean background not affected by the emissions from the upwind city is more objective and more easily intercomparable than trying to incorporate the effect of the city emissions in the background ozone calculation. In this work, we define a clean-background ozone as the portion of ozone that does not have chemical signatures that show ozone production from anthropogenic or natural emissions of ozone precursors. This definition is akin to deriving the ozone background using the O_3-NO_z regression method, but it is more refined (Altshuller and Lefohn, 1996). Hereafter we refer this clean-background ozone level as the ozone background in this work.

Another well-known linear relationship is between ozone and its precursor, CO (Parrish et al., 1993; Chin et al., 1994; Buhr et al., 1996; Parrish et al., 1998; Cardenas et al., 1998; Cooper et al., 2002; Honrath et al., 2004; Mao et al., 2004; Huntrieser et al., 2005). Cheng et al. (2017) examined the measurements from the DISCOVER-AQ campaign in July 2011 over the Baltimore-Washington area and found that the O_3-CO correlation does not vary significantly with time or altitude in the boundary layer and the observations are simulated well by our regional chemical transport model (REAM). Their analysis suggests that, due to the decrease of anthropogenic primary CO emissions during the past decades, the contribution from biogenic isoprene oxidation to the observed O_3-CO regression slope is as large as primary anthropogenic CO emissions in contrast to the finding that anthropogenic emissions are the main contributor to the observed O_3-CO relationship in the 1980s and early 1990s (Chin et al., 1994).

Cheng et al. (2018) went a step further and examined the utility of the robust linear regression relationships of observed O_3-HCHO, O_3-CO, and CO-HCHO, which do not vary significantly with time (11 A.M. to 4 P.M.) or altitude in the boundary layer during the

DISCOVER-AQ 2011 experiment. They found that these relationships can be used to provide a fast-response estimator of surface ozone when the concentrations of CO and HCHO are known in the Southeast. What we will explore in this study is how the relationships of ozone with CO and HCHO can be applied to compute background ozone (hereafter referred to as the O_3-CO-HCHO method).

In this study, we applied the methods of O_3-CO-HCHO (Cheng et al., 2018), O_3-NO_z (Altshuller and Lefohn, 1996; Hirsch et al., 1996), and 5th percentile ozone (Wilson et al., 2012) to surface and aircraft observations during the Southern Oxidant and Aerosol Study (SOAS) and Southeast Nexus (SENEX) campaigns in the summer of 2013 in the Southeast and the corresponding 3-D model simulation results. A model-only zero-emission method (Fiore et al., 2003; Dolwick et al., 2015) was also used. The background ozone concentrations derived from the observations and model results using various methods are compared to investigate the potential biases of the methods. We will show the distribution of summertime background ozone based on model simulations and discuss the implications for air quality management.

4.2 Methods and datasets

4.2.1 Observation datasets

We made use of the extensive observations during the Southeast Atmosphere Study (SAS) from 1 June 2013 to 15 July 2013 (Carlton et al., 2018). The SAS includes two field campaigns: SOAS and SENEX. SOAS provides detailed ground measurements of O_3, NO_x, NO_y, CO, and HCHO at the SouthEastern Aerosol Research and Characterization Network (SEARCH) site — Centreville, Alabama from 1 June to 15 July. It is a typical rural site in

the Southeast surrounded by mixed forest where biogenic emissions are dominant (Feiner et al., 2016). Along with SOAS, the National Oceanic and Atmospheric Administration (NOAA) WP-3D aircraft was deployed during the SENEX campaign to extensively measure O_3, NO_x, NO_y, CO, and HCHO concentrations around Smyrna, Tennessee. During the SENEX campaign, a total of 12 daytime flights were conducted to make atmospheric measurements in the lower troposphere. In this study, we selected the SENEX measurements in the Southeast at 0-1 km to derive the background ozone concentrations in the boundary layer in order to ensure the robustness of our O_3-CO-HCHO analysis results in the region where biogenic emissions dominate VOC reactivity and compared them to the ozone background derived from the SOAS surface data. For consistency, NO_y measurements using the chemiluminescence instruments were used to compute observed NO_z concentrations for both campaigns. Table 4.1 summarizes the instruments and uncertainties for O_3, NO_x, NO_y, CO and HCHO measurements (Ryerson et al., 1999; Holloway et al., 2000; Hansen et al., 2003; Hottle et al., 2009; Pollack et al., 2010).

Table 4.1 Atmospheric O_3, NO, NO_2, NO_y, CO and HCHO measurements during 2013 SOAS and SENEX campaigns.

	SOAS				SENEX			
	Technique	Detec. Limit	Sample Interval	Reference	Technique	Detec. Limit	Sample Interval	Reference
O_3	UV-Absorption	1 ppb	1-min	Hanen et al. (2003)	Chemiluminescence	15 ppt	1s	Ryerson et al. (1999) Pollack et al. (2010)
NO	Chemiluminescence	0.05 ppb	1-min			10 ppt	1s	
NO_2	Photolysis/ Chemiluminescence	0.1 ppb	1-min			30 ppt	1s	
NO_y	Mo reduction/ Chemiluminescence	0.1 ppb	1-min			40 ppt	1s	
CO	Nondispersive Infrared Spectroscopy	5 ppb	1-min		Vacuum UV Resonance Fluorescence	0.5 ppb	1s	Holloway et al. (2000)
HCHO	Fiber - Laser Induced Fluorescence	0.05 ppb	1s	Hottle et al. (2009)	Fiber - Laser Induced Fluorescence	36 ppt	1s	Hottle et al. (2009)

4.2.2 3-D REAM Model

We applied the Regional chEmistry and trAnsport Model (REAM) in this study to compute the regional background ozone in the Southeast during the SAS. REAM is a 3-D regional model which has been evaluated in a number of tropospheric chemistry and transport studies in the United States and China (Zhao et al., 2009; Zhao and Wang, 2009; Zhao et al., 2010; Liu et al., 2014; Gu et al., 2013; Gu et al., 2014; Gu et al., 2016; Zhang and Wang et al., 2016; Zhang et al., 2017; Li et al.,2019; Qu et al., 2020). The model domain of REAM is shown in Figure 4.8, with 30 vertical layers in the troposphere, and the horizontal resolution is 36 × 36 km^2. Simulations used in this study utilized lateral

boundary conditions taken from a 2° × 2.5° GEOS-Chem model (v11.01) simulation (Bey et al., 2001). Henderson et al. (2014) evaluated the GEOS-Chem model with respect to its ability to provide lateral boundary conditions of ozone and its precursors for the contiguous United States (CONUS) domain to regional models and showed good performance in the summer. The model is driven by assimilated meteorological fields from a Weather Research and Forecasting (WRF) simulation constrained by the Climate Forecast System Reanalysis products (EMC, 2019). The chemistry mechanism is from the GEOS-Chem (v11.01) with updated isoprene nitrate uptake on aerosols (Canty et al., 2015; Travis et al., 2016). Anthropogenic emissions are from the 2011 National Emission Inventories (2011 NEI). Biogenic emissions are calculated with the Model of Emissions of Gases and Aerosols from Nature (MEGAN) version 2.10 (Guenther et al., 2012). Emissions from biomass burning are not considered here in the model in the Southeast during summer due to the extremely small amount compared to anthropogenic, natural sources (Washenfelder et al., 2015). As shown in Figure 4.1 and Figure 4.2, the coincident REAM simulation results are generally within the standard deviations of observed surface and boundary-layer O_3, NO_x, NO_y (The sum of NO_x, PAN and HNO_3 are used as the NO_y concentrations in the model), CO, and HCHO concentrations. We discuss the potential effects of the model biases on simulation-derived background ozone concentrations in the result section.

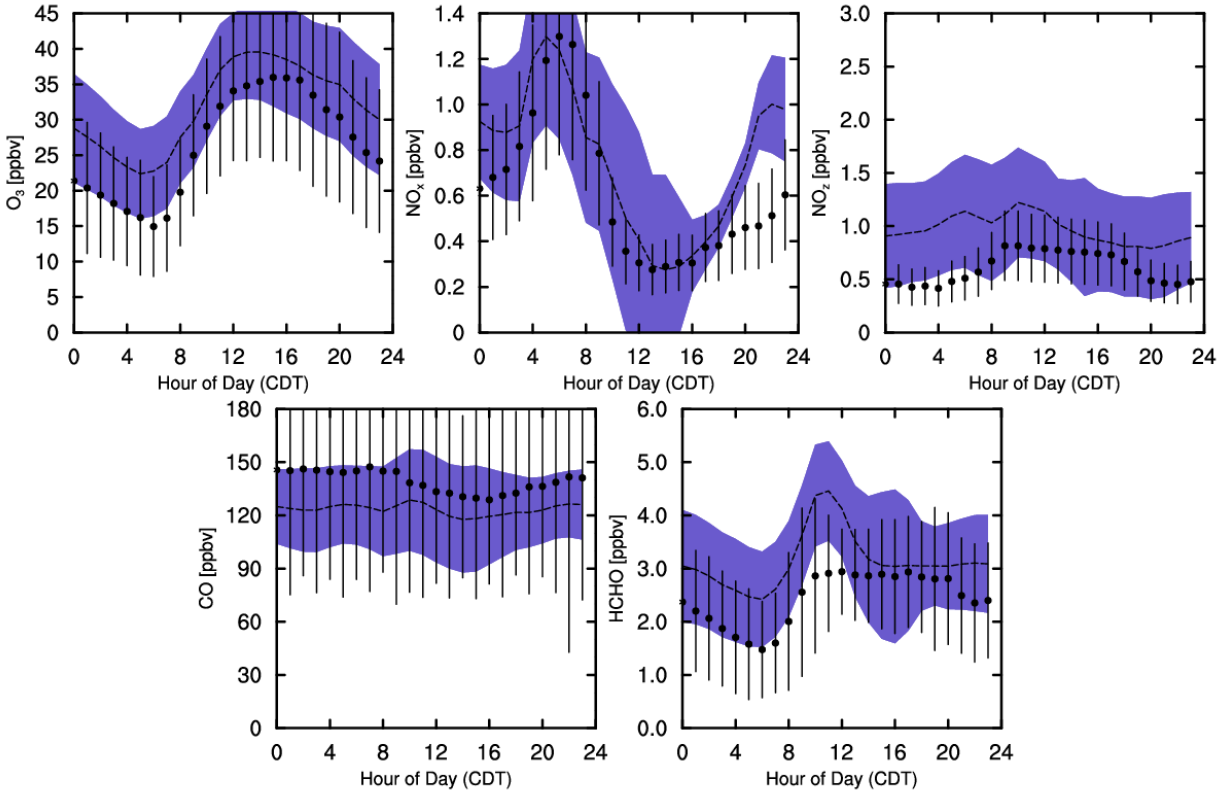

Figure 4.1 Observed (black dots) and modeled (dash line) mean diurnal profiles of surface O_3, NO_x, NO_z, CO and HCHO at Centreville during the 2013 SOAS campaign. Vertical bars show the standard deviations of hourly measurement data, and blue shadings represent the model standard deviations. The model was sampled in the Centreville grid box only for hours with available measurements from 1 June to 15 July.

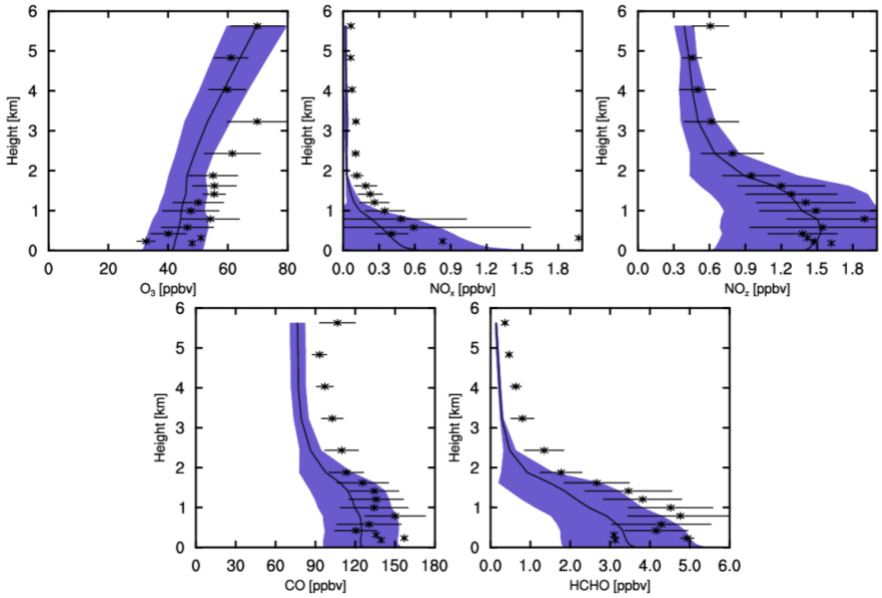

Figure 4.2 Observed (black dots) and modeled (solid line) mean vertical profiles of O_3, NO_x, NO_z, CO and HCHO over the Southeast US during the 2013 SENEX campaign. Measurement data are binned to model's vertical levels and horizontal bars indicate the standard deviations within each altitude bin. Blue shading represents the model standard deviations. The model was sampled at the time and locations of aircraft measurements.

4.2.3 Principle of the O_3-CO-HCHO method

As discussed by Cheng et al. (2018), regional O_3 can be decomposed into three components: O_3 produced from anthropogenic emissions ($O_{3anthro}$), O_3 produced from biogenic emissions (O_{3bio}), and background O_3 (O_{3back}). In a region where CO is from both biogenic and anthropogenic sources, but HCHO is dominated by the biogenic source, the CO-HCHO relationship can be used to compute the anthropogenic contribution to CO. As such, the three O_3 components can be separated based on Equation (2.1), detailed derivations are discussed by Cheng et al. (2018):

$$O_3 = \frac{\Delta O_3}{\Delta CO_{anthro}}(CO_{total} - \frac{\Delta CO_{bio}}{\Delta HCHO_{bio}}(HCHO_{total} - HCHO_{back}) - CO_{back}) + \frac{\Delta O_3}{\Delta HCHO_{bio}}(HCHO_{total} - HCHO_{back}) + O_{3back}$$

$$= k_1(CO_{total} - CO_{back}) - (k_1 k_2 - k_3)(HCHO_{total} - HCHO_{back}) + O_{3back} \quad (4.1)$$

where $k_1 = \frac{\Delta O_3}{\Delta CO_{anthro}}$, $k_2 = \frac{\Delta CO_{bio}}{\Delta HCHO_{bio}}$, $k_3 = \frac{\Delta O_3}{\Delta HCHO_{bio}}$, "anthro" denotes those from anthropogenic sources, "bio" denotes those from biogenic sources, and "total" denotes those from all sources, "back" denotes background values. The relationship of Eq. (1) reflects the net changes of the chemical species due to chemical production, loss, transport, and deposition. At present, we cannot separate the contribution from each process to the relationship.

We choose the time window of 11 am to 4 pm with active photochemistry over the southeastern United States where these three species are temporospatially stable (Figure 4.1) and the contributions from biogenic isoprene to the slope of O_3 to HCHO is dominant (Cheng et al., 2018) to ensure the robustness of our analysis.

We conducted tagged tracer simulations to derive CO and HCHO from anthropogenic and biogenic sources (including emissions and chemical production) and background transport (model lateral and upper boundary) separately while keeping model simulated other trace gases and radical concentrations, such as O_3, NO_x, and HO_x (OH and HO_2), the same as in the standard model, details as shown in the previous studies by Cheng et al. (2017, 2018). Using tagged tracer simulation results, we can compute the values of

k_1, k_2, and k_3 through least-squares regressions of O_3 and anthropogenic CO, biogenic CO and HCHO, O_3 and biogenic HCHO, respectively. We used Equation (4.1) to compute background ozone:

$$O_{3back} = O_3 - k_1(CO_{total} - CO_{back}) + (k_1k_2 - k_3)(HCHO_{total} - HCHO_{back}) \quad (4.2)$$

All variables on the right-hand side of the Equation (4.2) are known from standard and tagged-tracer model simulations and the background O_3 can be computed using Equation (4.2).

When using the observations, we cannot separate species from different sources. Therefore, the values of k_1, k_2, k_3, and background concentrations of CO, HCHO, and O_3 must be determined empirically. We applied a nonlinear regression (Holland et al., 1977) of Equation (4.1) to the SOAS and SENEX measurement data during the hours of active photochemistry between 11 am and 4 pm. The observation-derived background ozone concentrations will be compared with model results.

4.2.4 Modified O_3-NO_z and other methods to estimate background ozone

In the O_3-NO_z method, the O_3 value at zero NO_z of the least-squares regression is taken as the background ozone in previous studies (Altshuller and Lefohn, 1996). Figure 4.3 shows the scatter plot of O_3 and NO_z during SENEX (0-1 km) at 11 am - 4 pm. A least-squares regression gives an intercept value of 29.8 ppbv. The scatter of the data is fairly large reflecting in part the varying degree of impact from regional emissions in the observations. In order to derive the clean-background ozone estimates, we did a second

least-squares regression for the data, of which the O_3 values are less than $a+b[NO_z]-0.5\sigma$, where a, b, and σ are the intercept, slope, standard deviation of the first least-squares regression. For a Gaussian distribution, the data below half of the standard deviation are the lower 31 percentile data. Its mean value is close to the lower 1-σ (1 standard deviation) value. Figure 4.3 shows that the second regression line is close to the lower 1-σ line of the first regression. Since the data distribution is not ideally Gaussian, the lower 1-σ line of the first regression is slightly below the second regression line using the lower 31 percentile data. We refer to this method as the 1-σ O_3-NO_z method. Using this method, we obtain an ozone background value of 20.5±2.6 ppbv for the boundary layer (0-1 km) during SENEX.

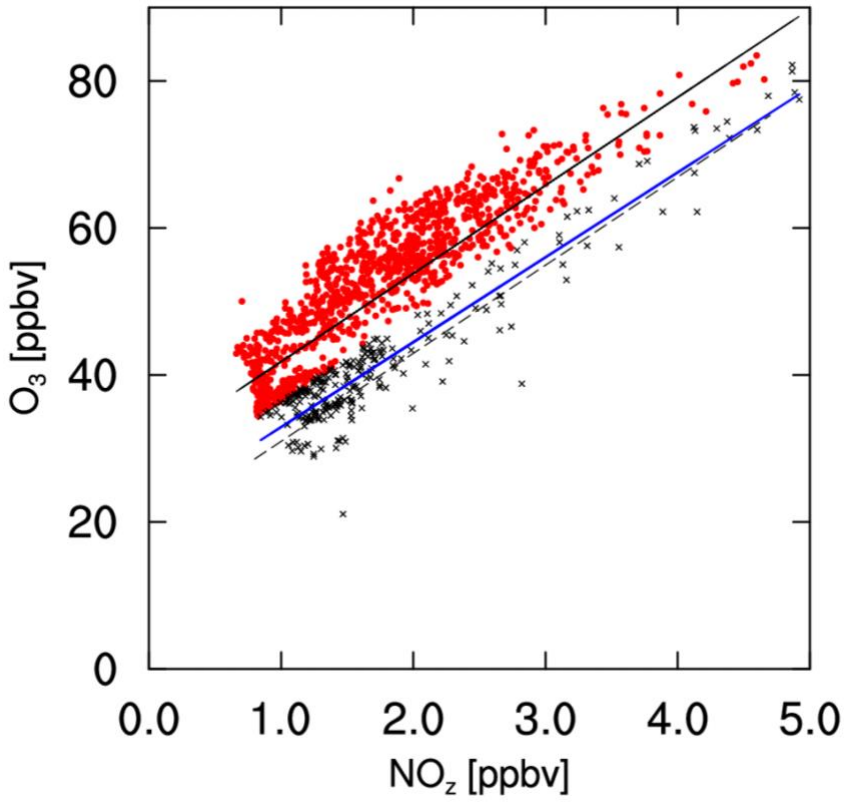

Figure 4.3 Relationship between observed O_3 and NO_z during SENEX (0-1 km) at 11 am - 4 pm. The black solid line is a linear fit of all data (red dots and black cross), the

blue solid line is a linear fit of data below half σ (black cross) and the black dash line is 1-σ cut-off line.

When using the zero-emission method (Fiore et al., 2003), we carried out a sensitivity simulation in which all anthropogenic emissions are turned off and the simulated O_3 concentrations are taken as the background. This method cannot be applied to the observation data. The 5th percentile method (Wilson et al., 2012), on the other hand, can be applied to both observation and model data, in which the 5th percentile O_3 concentrations are taken as the background. In order to compare to the results using the O_3-CO-HCHO method, observation and model data from 11 am to 4 pm were analyzed.

In this study, we seek to compute objectively the clean-background ozone as the portion of ozone that does not have chemical signatures that show ozone production from anthropogenic or natural emissions of ozone precursors based on the relationship of O_3-CO-HCHO. In the comparison to the results using other methods, we adapted the O_3-NO_z method to the 1-σ O_3-NO_z method for clean airmasses not affected by regional emissions. We applied the 5th percentile method to the entire analysis dataset such that the results are independent from site or data selection.

4.3 Results and discussion

4.3.1 Background ozone concentrations derived from SOAS and SENEX observations and corresponding model simulations using different methods

We applied different methods, tagged-tracer simulations and nonlinear regression method, to solve Equation (4.2) and derive the background ozone using simulated and observed data during SOAS and SENEX campaign as observation data cannot distinguish

tracer gases from different sources. We first discuss the results using the O_3-CO-HCHO method. Figure 4.4 shows the derived background values of O_3, CO, and HCHO, and the slopes of k_1, k_2, and k_3, in Equations (4.1) and (4.2), based on the observation and corresponding model data. The relationships between O_3, CO and HCHO during the SOAS and SENEX campaign are shown in Figure 4.5. The correlations between O_3 and CO are tighter than those of O_3 or CO with HCHO partly because the lifetime of HCHO is shorter than O_3 and CO. The general positive slops of O_3 to CO or HCHO, and CO to HCHO reflect photochemical productions of O_3, CO, and HCHO. Since the lifetimes of CO and O_3 are long enough for significant regional transport, both transport and chemistry errors in the model can lead to deviations from the observations and the transport effect is larger for CO. Detailed analysis requires another study and is beyond the scope of this work.

The error bars shown in Figure 1 are standard deviations of hourly values for the model simulations and standard errors of nonlinear regressions for the observations. In the model average, we first calculate the average regression results of k_1, k_2 and k_3 from all hours matching valid observations during 11 am to 4 pm. We apply the mean k_1, k_2 and k_3 to Equation (4.2), where total concentrations of CO, HCHO and O_3 and background values of CO and HCHO are hourly results of model simulations, to derive hourly background ozone concentrations. We finally take the mean of those hourly background ozone concentrations as the averaged background ozone shown in the plots. We use the error ranges of six parameters shown in Figure 4.4 to indicate the goodness of the nonlinear regression results. In a nonlinear regression, the traditional R^2 value, the fraction of the total variance explained by the regression model, cannot be used to assess the goodness-of-fit of the nonlinear model since the total variance does not equal to the sum of explained

variance and error variance and the R^2 value is not in the range of 0-100% (Spiess and Neumeyer, 2010). The parameter uncertainties reflect the effects of the independent variables and random data variations on the regression model (Ruckstuhl, 2010). The small standard errors of the six parameters shown in the Figure 4.4 indicate the robustness of the fitting results.

Observed and model-derived parameters are generally in good agreement; the one standard deviation error ranges of the parameters mostly overlap. The exception is that the model derived k_2 values are 10-30% lower than the observations. It may imply that either the CO yield is low or the net HCHO yield is high in the simulated isoprene chemical mechanism although regional transport of CO may also have an impact on the model bias. While additional measurements and modeling are necessary to infer the biases of CO and HCHO yields in the model isoprene oxidation mechanism, the analysis here provides an additional method to make use of the observation data to test the model chemical mechanism. The reasons for the observed and simulated 20-30% lower k_2 values at Centerville than the SENEX data are unclear. The large vertical gradients of NO_x, CO, and HCHO in the boundary layer (Figure 4.2), the nonlinear isoprene chemistry, and the sampling differences in time and location are among the factors complicating a quantitative analysis. Because CO has a long lifetime, the slope value of k_1 can be thought of as a measure of the O_3 production efficiency by anthropogenic NO_x during isoprene oxidation. The fairly good agreement between the model and observation results provides support for using the model to simulate the change of O_3 due to anthropogenic emissions. The slope value of k_3 indicates the change of O_3 relative to HCHO during isoprene oxidation. The value is much larger than 1 largely because of a much longer lifetime of O_3 than HCHO.

The observation and model-derived background levels of CO (50-65 ppbv) and HCHO (0.4-0.7 ppbv) are largely due to the oxidation of CH_4 and comparable to results of Cheng et al. (2018). The derived CO and HCHO background values using observations have lower uncertainties than the model results due largely to the difference of the calculation method. The purpose of a regression model is to minimize the uncertainties of regression function and parameters. Therefore, the range of the uncertainty reflects not just how well the regression model fits the data but also the optimization in the parameter space. The model background CO and HCHO mean and standard deviation values are computed directly using tagged tracer simulations. The standard deviations reflect the spatiotemporal variations of the model data. There is no optimization process to minimize the uncertainties in the model estimates. In other words, all terms on the right-hand side of Equation (4.2) are known from the model results, but they are unknown in the observation data. The higher degree of freedom in the nonlinear regression optimization of the observation data results in lower uncertainty estimates in the parameter space.

Using the O_3-CO-HCHO method, we estimate background ozone concentrations of 14.7±3.3 and 20.5±2.6 ppbv for SOAS and SENEX observations, respectively. The corresponding values for the model results are 13.9±5.7 and 20.8±4.8 ppbv, ~1 ppbv difference compared to the observation-based values but well within the standard deviations of the estimates. On average, the SENEX background ozone at 0-1 km is ~6 ppbv higher than that of SOAS near the surface in both observations and models, reflecting the effect of dry deposition loss of ozone at the surface. The excellent agreement between model and observation values reflects in part the robustness of this method.

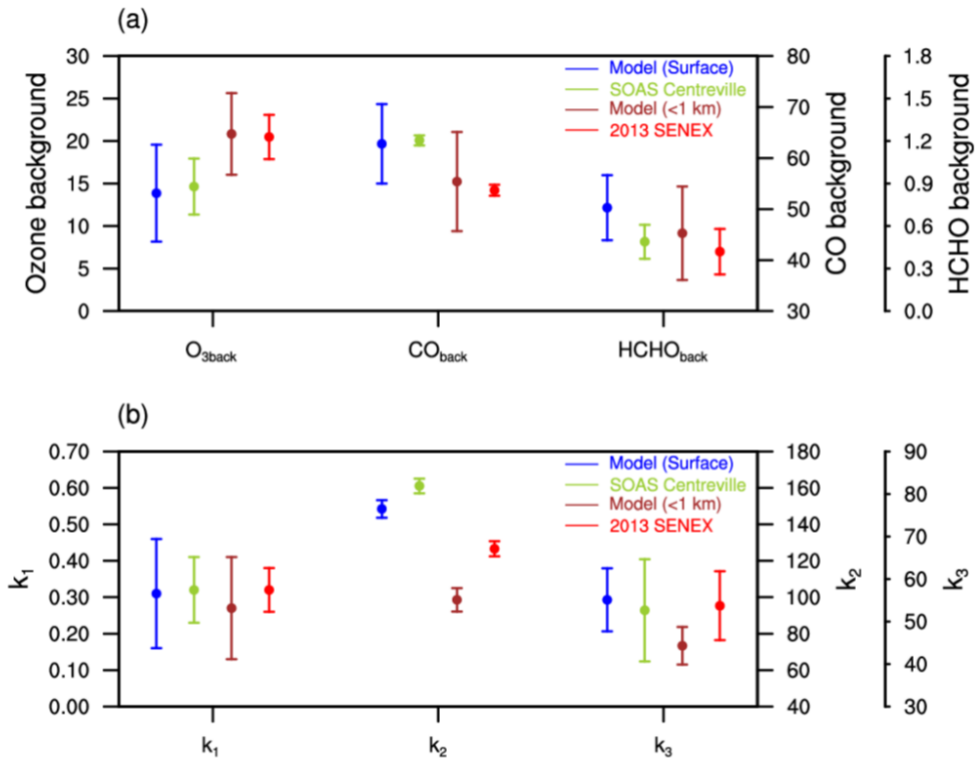

Figure 4.4 Estimates of the six parameters (O_{3back}, CO_{back}, $HCHO_{back}$, k_1, k_2 and k_3) in Equation (4.1) and (4.2) calculated using the observations during the 2013 SOAS Centreville campaign (green), 0-1 km measurements during the 2013 SENEX aircraft campaign (red), and the corresponding model results (blue for SOAS and brown for SENEX 0-1 km). Standard deviations of the estimates are shown by vertical bars. Daytime data from 11 am to 4 pm are used.

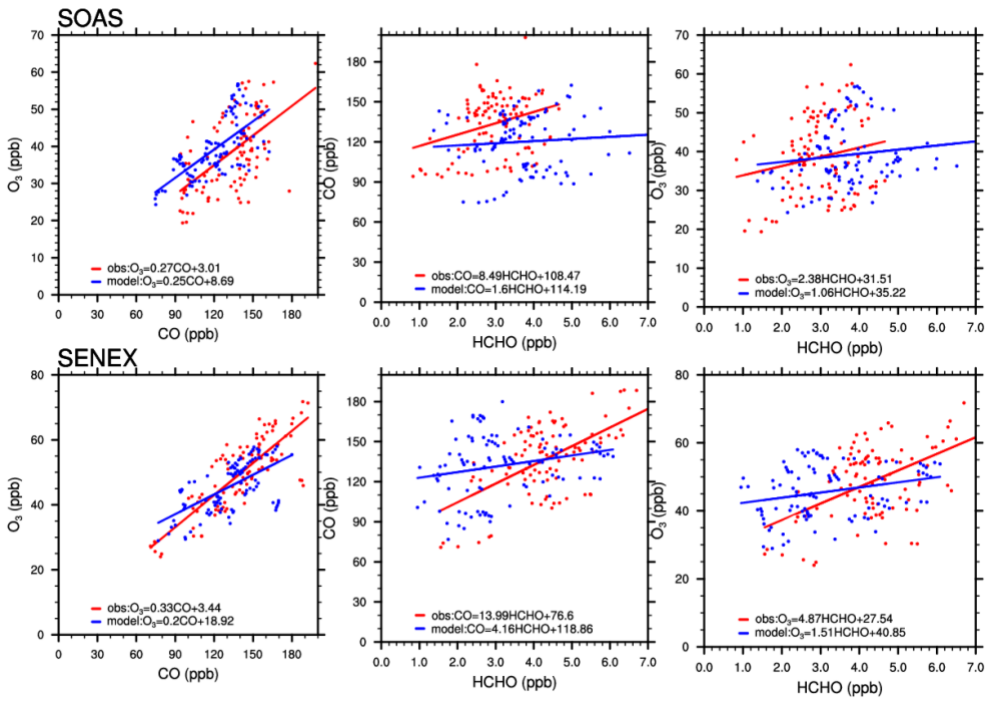

Figure 4.5 Scatter plots of O_3, CO and HCHO observations (red) during the SOAS and SENEX (0-1 km) campaigns at 11 am - 4 pm with corresponding model results (blue). The solid lines are linear regression of observed (red) and simulated (blue) data.

4.3.2 Comparisons of background ozone estimates using the O_3-CO-HCHO method to the previous methods

The comparison results are summarized in Figure 4.6. Among the previously used methods, the modified 1-σ O_3-NO_z method is the most similar to the O_3-CO-HCHO method, both of which rely on tracer correlations in the estimation of a clean-background ozone. However, the latter new method makes use of the full observation datasets while the former uses the lower 31 percentile data. The estimated background ozone concentrations are 18.7±6.5 and 21.3±10.5 ppbv, respectively, for SOAS (surface) and

SENEX (0-1 km) observations in the 1-σ O_3-NO_z method. The corresponding model estimates are 19.9±6.4 and 21.0±7.6 ppbv. The small increase of background ozone from the surface to 1 km can be found both in the model and observation data. Overall, the background concentrations derived using the 1-σ O_3-NO_z method are similar to the O_3-CO-HCHO results within the boundary layer, but higher by about 40% than the O_3-CO-HCHO method at the surface. It implies that the 1-σ threshold we chosen to indicate the clean-background ozone may bias high at the surface. We can reduce the high biases using the 1-σ O_3-NO_z method by increasing the cut-off threshold of $0.5\sigma_z$ from the regression line. If it is increased to $1\sigma_z$ from the regression line, we would use about 17% of the dataset. Since there is no physically based criterion for determining the cut-off threshold, the decision is statistical in nature. A small fraction of the data population calls into the question of the data representativeness. For example, if the 1σ cut-off line is used in Figure 4.3, only about 20 data points are left for NO_z > 2.5 ppbv, not representative of the original data.

Compared to the 1-σ O_3-NO_z method, the O_3-NO_z method gives 25-40% higher estimates, which are 26.5±8.8 and 29.8±10.8 ppbv for SOAS and SENEX observations, respectively, and the corresponding values are 27.6±9.2 and 26.8±10.1 ppbv in the model. The results are consistent with the discussion of Figure 4.3. The data scattering and higher intercepts of the O_3-NO_z regression reflect the variability of ozone production in the sampled air masses. For the purpose of deriving the clean-background ozone in this work, the 1-σ O_3-NO_z method is more appropriate.

The zero-emission method is for model only. Using the model data corresponding to the observations, we estimate background ozone concentrations of 20.6±4.7 and 21.3±6.9 ppbv for model data corresponding to the SOAS (surface) and SENEX (0-1 km) observations, respectively, which are 3-48% higher than the estimates using the O_3-CO-HCHO method. Fiore et al. (2013) found a mean afternoon background ozone of 15-30 ppbv in the eastern United States using the zero-emission method. Our zero-emission results are similar and in the middle range of their results. The higher zero-emission background ozone concentrations than those derived using the O_3-CO-HCHO method or the 1-σ O_3-NO_z method reflect two processes. In zero-emission simulations, all anthropogenic emissions are zeroed out but natural emissions, such as soil and lightning NO_x, are included, leading to chemical production of ozone by regional sources. In the O_3-CO-HCHO methods, anthropogenic and natural precursors are treated in the same manner and the derived background ozone is presumed to be independent of both anthropogenic and natural sources in the region. Another reason is that the HO_2 radical promotes ozone production and loss through the reactions of HO_2 + NO and HO_2 + O_3, respectively. In a photochemically active boundary layer with anthropogenic and natural emissions, background ozone transported from remote regions has a shorter lifetime and lower concentrations due in part to higher HO_2 concentrations compared to a photochemical environment without anthropogenic emissions and low ozone concentrations. For this chemical-nonlinearity reason, we expect a lower ozone background in the daytime than nighttime and in summer than the other seasons.

The 5th percentile method yields higher estimates of background ozone in general, 20.8±0.9 and 27.3±0.3 ppbv for SOAS (surface) and SENEX (0-1 km) observations,

respectively. The uncertainties, which are estimated using 10,000 times bootstraps, are considerably less than other methods. The corresponding model results are 27.7±0.5 and 31.6±0.5 ppbv. The lower value based on the SOAS observations than SENEX measurements could reflect periods of low surface ozone when the observation site was strongly affected by transport from the Gulf of Mexico, and lower modeled background values imply the effect of which was underestimated by the model. These estimates are 40-100% higher than the estimates using the O_3-CO-HCHO method. Wilson et al. (2012) selected 5^{th} percentile as the background ozone value based on 397 ground sites representing not only "baseline" sites, but also rural, suburban and urban sites. The implicit 5^{th} percentile selection as the background ozone level can be problematic with higher or lower estimation under different pollution environments. Also, the statistical and physical reasons of using a specific percentile as the background level are not apparent.

Among the various estimates, the O_3-CO-HCHO method gives the largest difference between the SOAS surface site and the SENEX 0-1 km background ozone concentrations. The 5^{th} percentile method also shows significantly lower ozone concentrations for SOAS surface background ozone reflecting in part the effect of ozone dry deposition to the surface. The zero-emission method shows less difference than the O_3-CO-HCHO method. The reason is related to shorter photochemical lifetime of background ozone with more active photochemistry driven by anthropogenic emissions, which we will discuss in more detail in the next section. The regular and 1-σ O_3-NO_z methods give somewhat lower SOAS surface than SENEX (0-1 km) background ozone concentrations, but the difference is well within the standard deviations. Unlike the other methods, the O_3-NO_z methods are also affected by dry deposition of HNO_3 to the surface, the rate of which

is much faster than ozone, thereby masking the effect of ozone dry deposition to the surface.

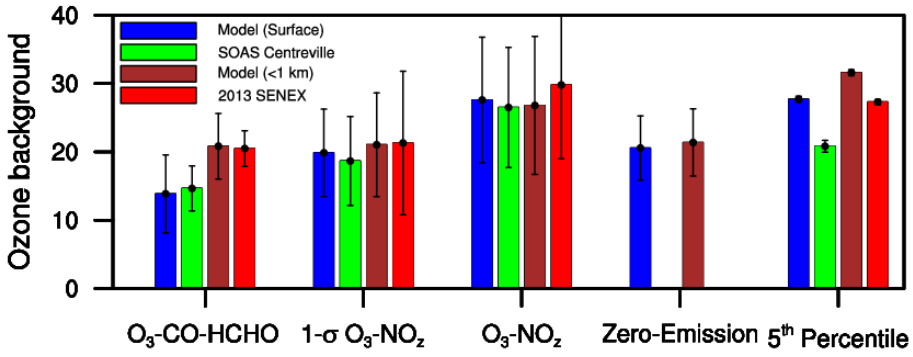

Figure 4.6 Estimated background ozone concentrations for the observations and corresponding model results during SOAS (surface) and SENEX (0-1 km). Standard deviations of the estimates are shown by vertical bars. Daytime data from 11 am to 4 pm are used.

4.3.3 Background ozone distribution in the Southeast

We compile previous background ozone estimates for the United States in Table 4.2. The previous observation and model studies suggest a background ozone of 15-40 ppbv for the eastern United States and higher levels for the western United States. The estimates using the new O_3-CO-HCHO method for SOAS and SENEX (Figure 4.6) are at the very low end of the previous estimates similar to the 1-σ O_3-NO_z results. Zero-emission result are in the middle range while the 5th percentile and O_3-NO_z results are more comparable to the previous studies.

To further compare to the previous studies, we apply the O_3-CO-HCHO and other methods to derive background ozone distributions of the Southeast for the summer (June-

August) of 2013 using model results. The O_3-CO-HCHO method can only be applied to the region where HCHO is dominated by biogenic isoprene emissions (Cheng et al., 2018). The other three methods are applied to the model results over the United States (Figure 4.8). The general distributions are similar to previous studies (Zhang et al., 2011; Emery et al., 2012; Parrish et al., 2017), showing that background ozone is about 20 ppbv higher in the West than the East.

Figure 4.7 compares the estimated background ozone distributions in the Southeast. The O_3-CO-HCHO and zero-emission methods give the most consistent distribution feature: background ozone concentrations decrease from the coastlines to inland regions. In comparison, the results from the 1-σ O_3-NO_z and 5th percentile methods show larger and different spatial variations in land areas. One difference between the O_3-CO-HCHO and zero-emission methods is apparent for the Atlanta region. The lifetime of ozone is impacted by photochemistry and dry deposition of ozone. In the O_3-CO-HCHO method, metropolitan areas yield a lower ozone background because active photochemistry decreases the lifetime of background ozone (Figure 4.10) and dry deposition lifetime have less impact on background ozone (Figure 4.12); the chemical lifetime of ozone is about 7 hours in Atlanta in comparison to 18 hours at Centreville. It is the opposite of the zero-emission method where the chemical lifetime of background ozone has been longer when there are no anthropogenic emissions and therefore the spatial variation of ozone is due primarily to dry deposition. The background ozone level of zero-emission is estimated higher in Atlanta than surrounding regions because of lower dry deposition loss of ozone in urban (~0.4 cm s^{-1} in Atlanta) than surrounding forest regions (0.6-0.7 cm s^{-1}) in the model (Figure 4.11). Since most of anthropogenic emissions occur near the surface, the

more active photochemistry driven by anthropogenic emissions tends to shorten ozone chemical lifetime near the surface. Therefore, changing ozone lifetime due to surface emissions and dry deposition to the surface tend to lead to increasing background ozone from urban to rural regions and from the surface to higher altitude (Figure 4.7 (e) and Figure 4.7 (f)).

The O_3-CO-HCHO method gives the lowest estimates of background ozone near the surface at 10-15 ppbv in the inland SE region, compared to 15-20, 15-25, and 20-30 ppbv in the zero-emission, 1-σ O_3-NO_z, and 5th percentile methods, respectively. Much of the differences are related to the interpretation of the results. The highest estimates by the 5th percentile method suggest that the effects of anthropogenic emissions are not entirely filtered out in this method. Downwind from an urban region, the estimate tends to be higher because ozone concentrations are higher than surrounding forest regions. The 1-σ O_3-NO_z estimates tend to have larger variations than other methods partly because HNO_3 is removed by dry and wet deposition. The effect of dry deposition is largest near the surface. The effect of wet deposition has large variations and is sporadic depending on convection, precipitation, and cloud, contributing to the uncertainties of this method. The zero-emission method does not consider the chemical nonlinearity and does not exclude the portion of ozone produced from natural emissions of ozone precursors.

The O_3-CO-HCHO method attempts to exclude the effects of anthropogenic and natural emissions of ozone precursors in the region on background ozone estimates. This method can be applied to both observation and model simulation data and the results are robust. The spatial distribution is what we expect, and it is the only method that shows

lower background ozone concentrations in urban regions (Figure 4.7). This method provides the means to compute the clean-background ozone as the portion of ozone that does not have chemical signatures that show ozone production from anthropogenic or natural emissions of ozone precursors. Compared to operationally defined background or baseline ozone levels, such as using the ozone measurements from a remote coastal "background" site which may still be affected by ozone produced from upwind polluted regions, the definition we used in this study does not rely on prior assumptions on factors such as the varying impacts of upwind polluted regions. It is therefore not surprising that we find a lower ozone background than computed using the other methods we tried or in comparison to previous studies. We suggest that the lower ozone background computed using the O_3-CO-HCHO method provides an objective basis for evaluating and interpreting the higher baseline ozone levels derived using operational definitions of ozone background.

The estimated clean background ozone tends to increase from urban to rural regions and from the surface to higher altitude due to changing ozone lifetime driven by surface emissions and dry deposition to the surface. A limitation of this method is that it does not discriminate anthropogenic from natural emissions. By comparing to the zero-emission method, the effect of chemical nonlinearity and natural emissions can be estimated, however, at ~5 ppbv in the Southeast (Figure 4.9). Unlike the model-only zero-emission method, the model-based background ozone estimates using O_3-CO-HCHO method can be evaluated using observations such as SOAS and SENEX. The lower summertime background ozone estimates using the newly developed O_3-CO-HCHO method than previous studies highlight the importance of the contributions by natural emissions to

ozone and the necessity to control anthropogenic emissions in ozone nonattainment areas of the Southeast.

Table 4.2 Previous observation and model estimates of background ozone in the United States.[a]

Study	Study period	Region	Method/Background statistics	Background Estimates
Trainer et al., 1993	Summer 1988	Eastern U.S.	O_3-NO_z/mean afternoon	30-40 ppbv
Hirsch et al., 1996	May-Sep 1990-1994	Harvard Forest[b]	O_3-NO_z/mean afternoon	25-40 ppbv
Altshuller and Lefohn, 1996	April-Oct 1988-1993	inland CONUS	O_3-NO_z/mean afternoon	25-45 ppbv
		coastal CONUS		25-35 ppbv
Lin et al., 2000	1980-1998	Harvard Forest	Percentile[c]/MDA8	35 (fall)-45 (Spring) ppbv
Fiore et al., 2002	Summer 1995	Eastern CONUS	Tracer tag[d] & zero-out (GEOS-Chem)/mean afternoon	15–30 ppbv
		Western CONUS		25-35 ppbv
Fiore et al., 2003	May-Oct 2001	U.S. CASTNet[e] Sites	Zero-out (GEOS-Chem) /mean afternoon	15-35 ppbv 40-50 ppbv at high altitude West sites
Zhang et al. 2011	2006-2008 (Spring-Summer)	U.S.	Zero-out (GEOS-Chem) /MDA8	27 ± 8 ppbv at low-altitude sites 40 ± 7 ppbv at high-altitude sites
Emery et al., 2011	Mar-Aug 2006	U.S.	Zero-out (CAMx with GEOS-Chem boundary)/ MDA8	25-50 ppbv
Huang et al., 2013	16th June to 14th July 2008	Pacific Southwest and Northwest	Assimilated forward sensitivity STEM model/ MDA8	30-35 ppbv
Fiore et al., 2014	Spring and summer 2006	Eastern CONUS	Zero-out (GEOS-Chem and GFDL AM3)/MDA8	40–50 ppbv in spring 25–40 ppbv in summer
		Western CONUS		20-30 ppbv in summer
Lefohn et al., 2014	2006	U.S.	Source apportionment (GEOS-Chem/CAMx) /MDA8	30–50 ppbv
Dolwick et al., 2015	Apr–Oct 2007	Rural West U.S.	Zero-out (CMAQ) and source apportionment (CAMx)/MDA8	40-45 ppbv (75–100% low ozone days 30-50% on ozone>75 ppbv)
Lin et al., 2015	1990-2012	Western CONUS	Zero-out (GFDL AM3)/MDA8	40-50 ppbv Apr-May 20 ppbv Jul-Aug
Dunker et al., 2017	Mar-Sep 2010	U.S. (12 cities)	Path-integral method (CAMx)/MDA8	30-65 ppbv
Parrish et al., 2017	1980 - 2015	Western CONUS	Regression analysis[f] /ODV	62.0 ± 1.9 ppb
Ninneman et al., 2019	2000-2017 & 2015-2017	Two rural sites in New York State	O_3-NO_z/mean afternoon	31-33 ppbv

Parrish and Ennis, 2019	mid-1970s-2017	Northern U.S.	Regression analysis[f] /ODV	Rural West: 54-63 ppbv The Northeast: 45.8±3.0

[a]Table is updated and modified from Jaffe et al., 2018.
[b]Rural site in central Massachusetts.
[c]The median values of ozone for the lowest 25th percentiles of CO and NO_y concentrations.
[d]Tag tracers to estimate ozone produced from outside of the U.S.
[e]Clean Air Status and Trends Network.
[f]An exponential function is used to quantify the temporal evolution of the Ozone Design Values (ODVs):
$ODV = y_0 + A \exp\{-(year-1980)/t\}$.
y_0 represents background ODVs. A is the enhancement of the ODVs above y_0 in 1980. t is the e-folding time constant.

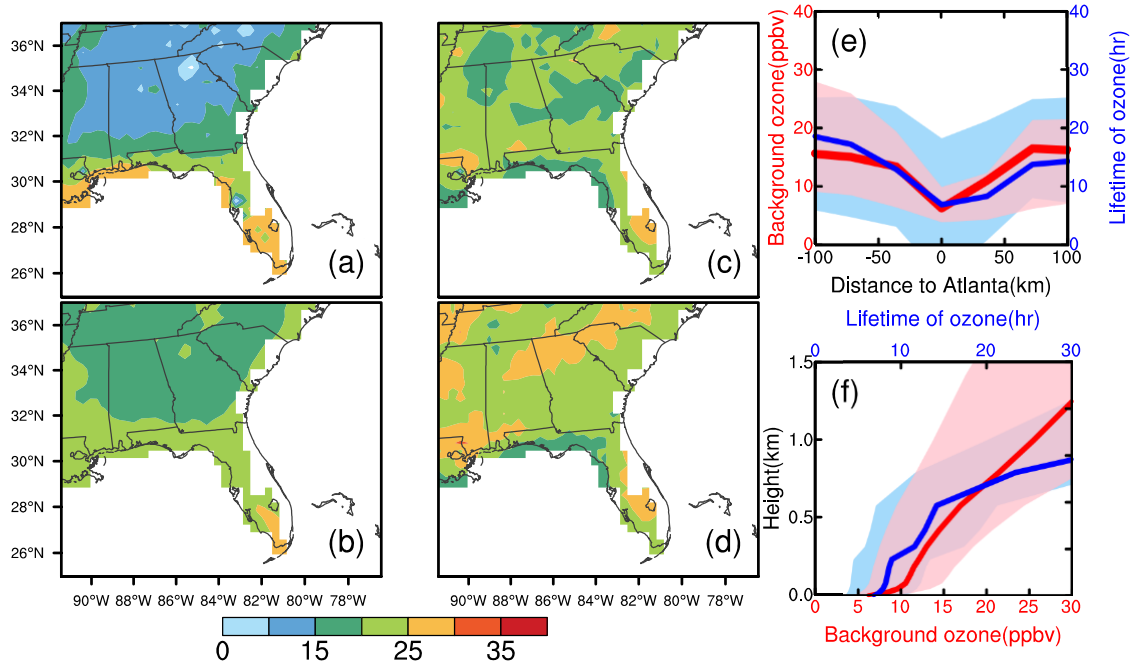

Figure 4.7 Estimates of background ozone distribution for the SE in the summer of 2013 using the O_3-CO-HCHO (a), zero-emission (b), 1-σ O_3-NO_z (c), and 5th percentile (d) methods. The horizontal distributions (e) and vertical distributions (f) of background ozone estimated by O_3-CO-HCHO method (red) and ozone lifetime (blue) from Atlanta city center to the rural regions and in the Atlanta in the summer of 2013. Blue and red shadings represent the standard errors of ozone lifetime and background ozone estimated by O_3-CO-HCHO method, respectively.

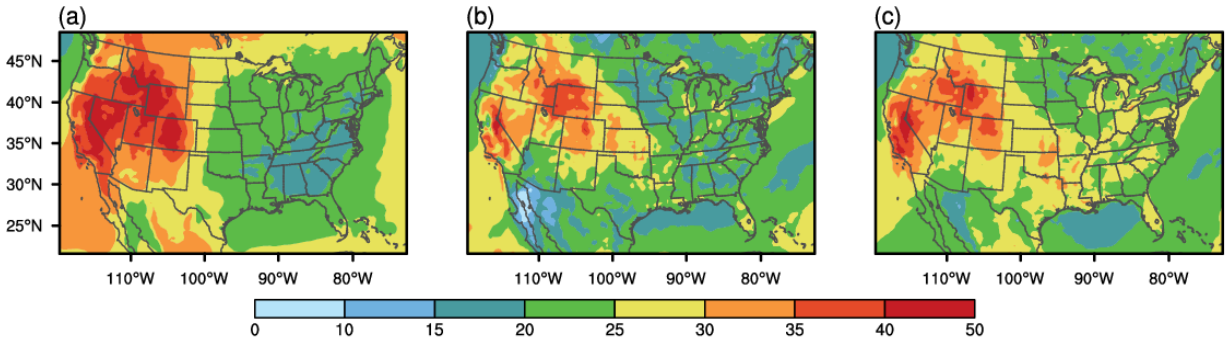

Figure 4.8 Same as Figure 4.7 but for the United States using the zero-emission (a), 1-σ O_3-NO_z (b), and 5th percentile (c) methods.

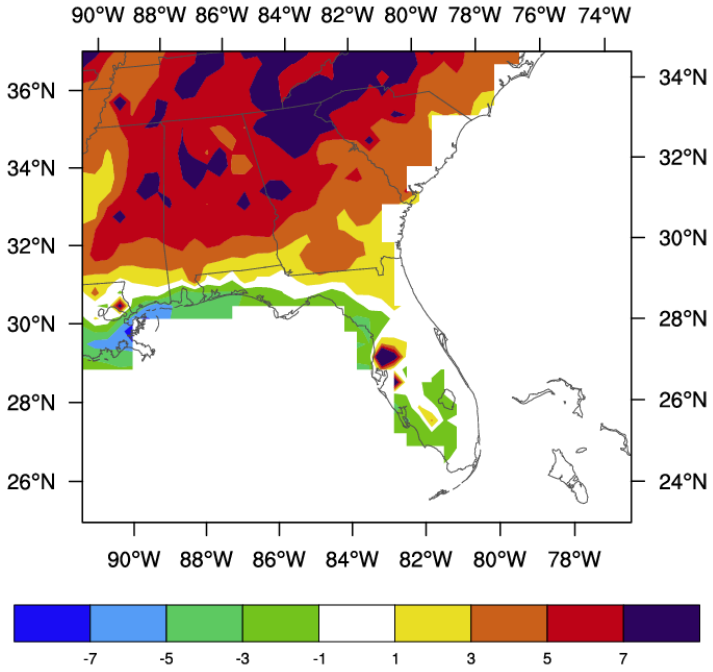

Figure 4.9 Difference of background ozone distribution between the O_3-CO-HCHO and zero-emission methods for the SE in the summer of 2013.

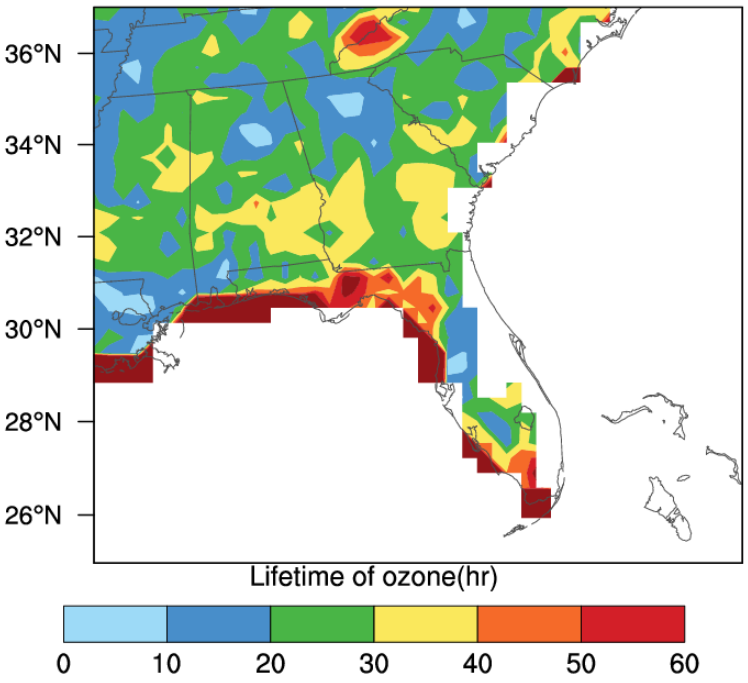

Figure 4.10 Distribution of ozone chemical lifetime (hr) over the SE for the summer of 2013.

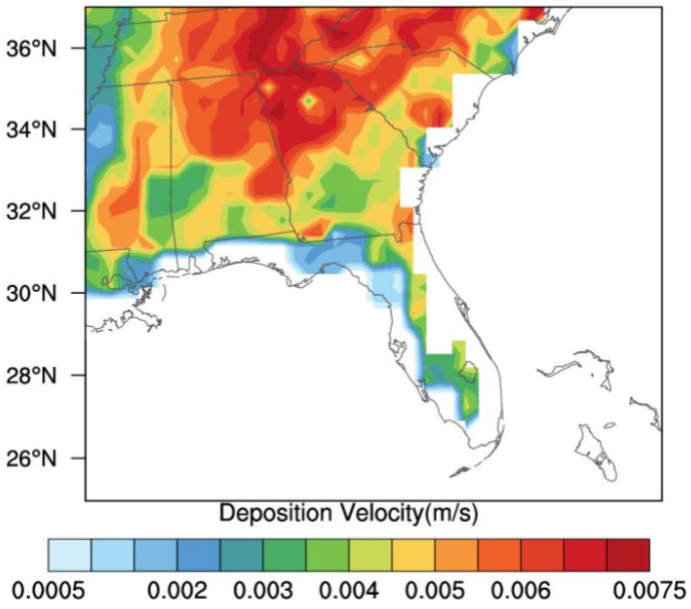

Figure 4.11 Distribution of ozone dry deposition velocity (m s^{-1}) over the SE for the summer of 2013.

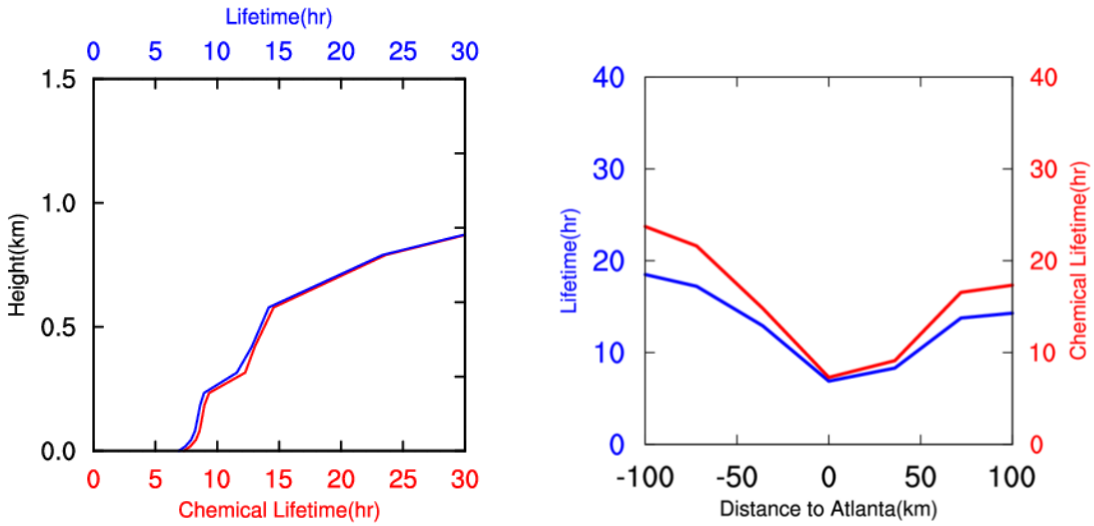

Figure 4.12. Vertical distributions (left) and horizontal distributions (right) of the ozone total lifetime (chemical and dry deposition lifetime) (blue) and chemical lifetime (red) in Atlanta (left) and from city to urban region (right) for the summer of 2013.

CHAPTER 5. CONCLUSIONS AND FUTURE WORKS

5.1 Biased distributions of anthropogenic and biogenic NO_x emissions in the West, Central and East United States

This study investigates the NO_x emissions on the sectoral basis, including onroad, nonroad, EGU, industry, Oil & Gas, aircraft, soil and lightning sources, over the West, Central and East CONUS. The estimated total NO_x emissions over the CONUS are 5.02 Tg N/a in consistent with the prior NAQFC emissions of 5.00 Tg N/a. Better matches between the simulated NO_2 VCDs and satellite observations has been found after we applied the 3SDRI method to derive the posterior source-specific NO_x emissions. We conclude that the distributions of different NO_x sources are biased in the prior estimates. The prior emissions tend to overestimate anthropogenic sources and underestimate natural emissions, especially mobile sources in the West. In the Central, soil NO_x emissions are overestimated, while the contribution from Oil & Gas are underestimated in the prior emissions. The posterior natural contributions in the East are generally consistent with the prior, but mobile sources are overestimated, and Oil & Gas are underestimated. We also analyze the composition of simulated NO_2 VCDs. Natural emissions have large column impacts and are predicted to contribute 30%-60% of the tropospheric NO_2 columns in the summer 2011. The nonlinear relationships between vertical NO_2 columns and NO_x emissions for specific emission sources are consistent at different emission levels. The posterior NO_x emissions provide minor improvements to the simulated MDA8 ozone, suggesting the potential importance of other processes in simulating the MDA8 ozone.

The future work of this study involves applying this source-specific 3SDRI method to smaller region (such as one specific U.S. state) with higher model resolutions and using high resolution satellite observations, such as TROPOMI. High resolution model focuses on a specific region can reduce the error caused by linear regression due to the heterogenous spatial and temporal distribution of different emission sources. TROPOMI has a pixel size of 3.5×5.6 km^2 at nadir since August 2019. Compared to previous satellite instruments, such as OMI used in this study, TROPOMI shows better performance of representing spatial variability (Van Geffen et al., 2020). Therefore, the results of the posterior emissions could be improved with more emission details captured by the satellite.

5.2 Transport dominated nocturnal isoprene and its implications on current model isoprene mechanism

This study explores the nocturnal decay of isoprene and isoprene oxidation processes at Centreville during the 2013 SOAS campaign. We use the REAM with mini-CIM isoprene chemistry mechanism to simulate the chemical and physical processes of isoprene at night. REAM well reproduces the observed diurnal cycles of surface isoprene and related tracer gases. We find that transport processes contribute 51.7% of the nocturnal isoprene removal, with approximately equal contributions from advection and vertical mixing. Ozone oxidation contributes to 24.4% of the total isoprene decay, consuming 0.6 ppb of isoprene, followed by 12.2% NO_3 oxidation and 11.8% OH oxidation contributions. Advection brings isoprene downwind Centreville. Increased isoprene concentrations overnight could bring up the next ozone levels in downwind areas. We also investigate the diurnal cycles of MVK and MACR, the first-generation oxidation products of isoprene,

and the gas and particle phase of isoprene nitrates. The MVK to MACR ratios further validate the importance of transport processes at night. The missing peaks of modeled MVK and MACR in the late afternoon, coinciding with the missing peaks in the diurnal profiles of isoprene nitrates (ISOPN1 and MVKN+MACRN), indicate that the unclarified isoprene oxidation processes in the model mechanism during the transition period from OH-driven to O_3-driven isoprene mechanism. Modeled pINs generally reproduce the diurnal variation of the SOAS Centreville observations but have issues with late afternoon peak and early morning peak, in part related to SOA mechanism in the model using homogeneous uptake coefficients and assuming a bulk lifetime for different species. Better model mechanism of isoprene oxidation from OH-driven to O_3-driven transition period and elucidation of formation and loss of pINs are needed in the future to accurately quantify the impacts of isoprene chemistry on the NO_x budgets and SOA formations.

5.3 Low summertime clean-background ozone in the Southeast

This study defines the clean-background ozone that is transported from distant troposphere and stratosphere and not affected by the emissions of ozone precursors in the study region. We apply the robust linear relationships of O_3-CO-HCHO in the Southeast United States found by Cheng et al. (2018) to estimate the background ozone levels evaluated by SOAS and SENEX observations. We note that model results are in consistent with observations. We find the background ozone is in the range of 10-15 ppbv in the inland areas of the Southeast using the O_3-CO-HCHO method. We also compare to previous estimations of background ozone, including O_3-NO_z, 5th percentile and zero-emission method. The O_3-CO-HCHO method gives the lowest estimates of background ozone near the surface at 10-15 ppbv in the inland SE region, compared to 15-20, 25-30,

and 20-30 ppbv in the zero-emission, O_3-NO_z, and 5th percentile methods, respectively. This background ozone tends to increase from urban centers to rural regions and from the surface to higher altitude due to changing ozone lifetime driven by surface emissions and dry deposition to the surface. Background ozone levels estimated from the zero-emission method ignores the non-linear chemical contributions from different sectors and regions and exclude the portion of ozone produced from natural emissions of ozone precursors. The results of O_3-NO_z method could include the transported ozone of photochemical origin. The effects of anthropogenic emissions are not entirely filtered out in the 5th percentile method. Lower than previous background ozone we derive in this study suggests further incentives to control anthropogenic emissions in ozone nonattainment areas of the Southeast.

The O_3-CO-HCHO method considers the impact of nonlinear chemistry compared to zero-emission method, where the lifetime of background ozone has been longer with zero-anthropogenic emissions and therefore estimate the higher background ozone concentrations. Considering the merits of our method, the clean-background ozone derived from the O_3-CO-HCHO method can be used in the future to estimate the trend of background ozone in the Southeast based on both model simulations and site measurements.

REFERENCES

Aliwell, S. R.; Jones, R. L. Measurements of tropospheric NO_3 at midlatitudes. *J. Geophys. Res.: Atmos*.**1998**, *103*, 5719–5727.

Allen, D. J.; Pickering, K. E.; Pinder, R. W.; Henderson, B. H.; Appell, K. W.; Prados, A.; Vogel, B. Impact of lightning-NO on eastern United States photochemistry during the summer of 2006 as determined using the CMAQ model. *Atmos. Chem. Phys.* **2012**, *12*(4), 1737-1758.

Allen, D. T. Emissions from oil and gas operations in the United States and their air quality implications. *J. Air. Waste. Manag. Assoc.* **2016**, *66*(6), 549-575.

Altshuller, A. P.; Lefohn, A. S. Background ozone in the planetary boundary layer over the United States. *J. Air. Waste. Manag. Assoc*. **1996**, *46*(2), 134-141.

Anderson, D. C.; Loughner, C. P.; Diskin, G.; Weinheimer, A.; Canty, T. P.; Salawitch, R. J.; Dickerson, R. R. Measured and modeled CO and NO_y in DISCOVER-AQ: An evaluation of emissions and chemistry over the eastern US. *Atmos. Environ.* **2014**, *96*, 78-87.

Atkinson, R.; Baulch, D. L.; Cox, R. A.; Crowley, J. N.; Hampson, R. F.; Hynes, R. G.; ...; Subcommittee, I. U. P. A. C. Evaluated kinetic and photochemical data for atmospheric chemistry: Volume II–gas phase reactions of organic species. *Atmos. Chem. Phys.* **2006**, *6*(11), 3625-4055.

Andronache, C.; Chameides, W. L.; Rodgers, M. O.; Martinez, J.; Zimmerman, P.; Greenberg, J. Vertical distribution of isoprene in the lower boundary layer of the rural and urban southern United States. *J. Geophys. Res.: Atmos*.**1994**, *99*(D8), 16989-16999.

Atkinson, R.; Aschmann, S. M. OH radical production from the gasphase reactions of O_3 with a series of alkenes under atmospheric conditions. *Environ. Sci. Technol*. **1993**, *27*, 1357-1363.

Bates, K. H.; Jacob, D. J. A new model mechanism for atmospheric oxidation of isoprene: global effects on oxidants, nitrogen oxides, organic products, and secondary organic aerosol. *Atmos. Chem. Phys*. **2019**, *19*(14), 9613-9640.

Beirle, S.; Platt, U.; Wenig, M.; Wagner, T. Weekly cycle of NO_2 by GOME measurements: A signature of anthropogenic sources. *Atmos. Chem. Phys.* **2003**, *3*(6), 2225-2232.

Beirle, S.; Huntrieser, H.; Wagner, T. Direct satellite observation of lightning-produced NOx. *Atmos. Chem. Phys*. **2010**, *10*, 10965-10986.

Bey, I.; Jacob, D.J.; Yantosca, R.M.; Logan, J.A.; Field, B.D.; Fiore, A.M.; Li, Q.; Liu, H.Y.; Mickley, L.J.; Schultz, M.G. Global modeling of tropospheric chemistry with assimilated meteorology: Model description and evaluation. *J. Geophys. Res.: Atmos*. **2001**, *106*(D19), 23073-23095.

Boersma, K. F.; Eskes, H. J.; Brinksma, E. J. Error analysis for tropospheric NO_2 retrieval from space. *J. Geophys. Res.* **2004**, *109*, D04311.

Boersma, K. F.; Eskes, H. J.; Meijer, E. W.; Kelder, H. M. Estimates of lightning NO_x production from GOME satellite observations. *Atmos. Chem. Phys*. **2005**, *5*(9), 2311-2331.

Boersma, K. F.; Jacob, D. J.; Trainic, M.; Rudich, Y.; De Smedt, I.; Dirksen, R.; Eskes, H. J. Validation of urban NO2 concentrations and their diurnal and seasonal variations observed from the SCIAMACHY and OMI sensors using in situ surface measurements in Israeli cities. *Atmos. Chem. Phys*. **2009**, *9*(12), 3867-3879.

Boersma, K. F.; Eskes, H. J.; Dirksen, R. J.; van der A, R. J.; Veefkind, J. P.; Stammes, P.; Huijnen, V.; Kleipool, Q. L.; Sneep, M.; Claas, J.; Leitao, J.; Richter, A.; Zhou, Y.; Brunner, D. An improved tropospheric NO_2 column retrieval algorithm for the Ozone Monitoring Instrument. *Atmos. Meas. Tech*. **2011**, *4*, 1905-1928.

Boersma, K. F.; Eskes, H.; Richter, A.; De Smedt, I.; Lorente, A.; Beirle, S.; Van Geffen, J.; Peters, E.; Van Roozendael, M.; Wagner, T. QA4ECV NO_2 tropospheric and stratospheric vertical column data from OMI (version 1.1) [data set]. Royal Netherlands Meteorological Institute (KNMI). 2017a. http://doi.org/10.21944/qa4ecv-no2-omi-v1.1.

Brown, S. S.; deGouw, J. A.; Warneke, C.; Ryerson, T. B.; Dubé, W. P.; Atlas, E.; Weber, R. J.; Peltier, R. E.; Neuman, J. A.; Roberts, J. M.; et al. Nocturnal Isoprene Oxidation over the Northeast United States in Summer and its Impact on Reactive Nitrogen Partitioning and Secondary Organic Aerosol. *Atmos. Chem. Phys*. **2009**, *9*, 3027−3042.

Buhr, M.; Sueper, D.; Trainer, M.; Goldan, P.; Kuster, B.; Fehsenfeld, F.; Kok, G.; Shillawski, R.; Schanot, A. Trace gas and aerosol measurements using aircraft data from the North Atlantic Regional Experiment (NARE 1993). *J. Geophys. Res.: Atmos.* **1996**, *101*(D22), 29013-29027.

Canty, T. P.; Hembeck, L.; Vinciguerra, T. P.; Anderson, D. C.; Goldberg, D. L.; Carpenter, S. F.; Allen, D. J.; Loughner, C. P.; Salawitch, R. J.; Dickerson, R. R. Ozone and NOx chemistry in the eastern US: evaluation of CMAQ/CB05 with satellite (OMI) data. *Atmos. Chem. Phys*. **2015**, *15*, 10965–10982.

Cao, P.; Lu, C. C.; Yu, Z. Historical nitrogen fertilizer use in agricultural ecosystems of the contiguous United States during 1850–2015: application rate, timing, and fertilizer types. *Earth Syst. Sci. Data Discuss*. **2018**, *10*, 969.

Cardenas, L. M.; Austin, J. F.; Burgess, R. A.; Clemitshaw, K. C.; Dorling, S.; Penkett, S. A.; Harrison, R. M. Correlations between CO, NO_y, O_3 and non-methane hydrocarbons and their relationships with meteorology during winter 1993 on the North Norfolk Coast, UK. *Atmos. Environ*. **1998**, *32*(19), 3339-3351.

Carlton, A. M.; J. de Gouw, J. L.; Jimenez, J. L.; Ambrose, S.; Brown, K. R.; Baker, C. A.; Brock, R. C.; Cohen, S.; Edgerton, C.; Farkas, D.; Farmer, A. H.; Goldstein, L.; Gratz, A.; Guenther, S.; Hunt, L.; Jaegle, D. A.; Jaffe, J.; Mak, C.; McClure, A.; Nenes, T. K. V.;́ Nguyen, J. R. X. Z. The Southeast Atmosphere Studies (SAS): coordinated investigation and discovery to answer critical questions about fundamental atmospheric processes. *Bull. Am. Meteorol. Soc*. **2017**, *94*, 413.

Carter, W. P.; Atkinson, R. Development and evaluation of a detailed mechanism for the atmospheric reactions of isoprene and NO_x. *Int. J. Chem. Kinet*. **1996**, *28*(7), 497-530.

Castellanos, P.; Boersma, K. F. Reductions in nitrogen oxides over Europe driven by environmental policy and economic recession. *Sci. Rep*. **2012**, *2*, 265, https://doi.org/10.1038/srep00265.

Chen, X.; Hulbert, D.; Shepson, P. B. Measurement of the Organic Nitrate Yield from OH Reaction with Isoprene. *J. Geophys. Res. - Atmos*. **1998**, *103*, 25563−25568.

Cheng, Y.; Wang, Y.; Zhang, Y.; Chen, G.; Crawford, J.H.; Kleb, M.M.; Diskin, G.S.; Weinheimer, A.J. Large biogenic contribution to boundary layer O_3-CO regression slope in summer. *Geophys. Res. Lett*. **2017**, *44*(13), 7061-7068.

Cheng, Y.; Wang, Y.; Zhang, Y.; Crawford, J. H.; Diskin, G. S.; Weinheimer, A. J.; Fried, A. Estimator of surface ozone using formaldehyde and carbon monoxide concentrations over the eastern United States in summer. *J. Geophys. Res.: Atmos*. **2018**, *123*(14), 7642-7655.

Chin, M.; Jacob, D. J.; Munger, J. W.; Parrish, D. D.; Doddridge, B. G. Relationship of ozone and carbon monoxide over North America. *J. Geophys. Res.: Atmos*. **1994**, *99*(D7), 14565-14573.

Choi, Y.; Wang, Y.; Zeng, T.; Martin, R.; Kurosu, T. P.; Chance, K. Evidence of lightning NO_x and convective transport of pollutants in satellite observations over North America. *Geophys. Res. Lett*. **2005**, *32*, DOI: 10.1029/2004GL021436.

Choi, Y.; Wang, Y. H.; Yang, Q.; Cunnold, D.; Zeng, T.; Shim, C.; Luo, M.; Eldering, A.; Bucsela, E.; Gleason, J. Spring to summer northward migration of high O_3 over the western North Atlantic. *Geophys. Res. Lett*. **2008**, *35*(4), doi:10.1029/2007GL032276.

Choi, Y.; Wang, Y.; Zeng, T.; Cunnold, D.; Yang, E.; Martion, R.; Chance, K.; Thouret, V.; Edgerton, E. Springtime transitions of NO_2, CO, and O_3 over North America: Model evaluation and analysis. *J. Geophys. Res.: Atmos*. **2008**, *113*(D20), doi:10.1029/2007JD009632.

Choi, Y.; Kim, H.; Tong, D.; Lee, P. Summertime weekly cycles of observed and modeled NO_x and O_3 concentrations as a function of satellite-derived ozone production sensitivity and land use types over the Continental United States. *Atmos. Chem. Phys*. **2012**, *12*(14), 6291-6307.

Chuong, B.; Stevens, P. S. Measurements of the Kinetics of the OH-Initiated Oxidation of Isoprene. *J. Geophys. Res*. **2002**, *107* (D13), ACH 2-1−ACH 2-12.

Climate Forecast System Reanalysis products; Environmental Modeling Center: College Park, MD, 2019; http://cfs.ncep.noaa.gov/cfsr.

Cooper, O.R.; Moody, J.L.; Parrish, D.D.; Trainer, M.; Holloway, J.S.; Hübler, G.; Fehsenfeld, F.C.; Stohl, A. Trace gas composition of midlatitude cyclones over the western North Atlantic Ocean: A seasonal comparison of O_3 and CO. J. *Geophys. Res.: Atmos*. **2002**, *107*(D7), ACH-2.

Cooper, O.R.; Moody, J.L.; Parrish, D.D.; Trainer, M.; Ryerson, T.B.; Holloway, J.S.; Hübler, G.; Fehsenfeld, F.C.; Evans, M.J. Trace gas composition of midlatitude cyclones over the western North Atlantic Ocean: A conceptual model. *J. Geophys. Res.: Atmos*. **2002**, *107*(D7), ACH-1.

Cooper, O. R.; Gao, R. S.; Tarasick, D.; Leblanc, T.; Sweeney, C. Long-term ozone trends at rural ozone monitoring sites across the United States, 1990–2010. *J. Geophys. Res.: Atmos*. **2012**, *117*(D22).

Cooper, O. R.; Langford, A. O.; Parrish, D. D.; Fahey, D. W. Challenges of a lowered US ozone standard. *Science*. **2015**, *348*(6239), 1096-1097.

Crounse, J. D.; McKinney, K. A.; Kwan, A. J.; Wennberg, P. O. Measurement of gas-phase hydroperoxides by chemical ionization mass spectrometry. *Analytical chemistry*. **2006**, *78*(19), 6726-6732.

Crutzen, P. J.; Zimmermann, P. H. The changing photochemistry of the troposphere. *Tellus.* **1991**, *43*, 136–151.

Cynthia Lin, C. Y.; Jacob, D. J.; Munger, J. W.; Fiore, A. M. Increasing background ozone in surface air over the United States. *Geophys. Res. Lett*. **2000**, *27*(21), 3465-3468.

Dolwick, P.; Akhtar, F.; Baker, K. R.; Possiel, N.; Simon, H.; Tonnesen, G. Comparison of background ozone estimates over the western United States based on two separate model methodologies. *Atmos. Environ*. **2015**, *109*, 282-296.

Duncan, B. N.; Yoshida, Y.; Olson, J. R.; Sillman, S.; Martin, R. V.; Lamsal, L.; Crawford, J. H. Application of OMI observations to a space-based indicator of NO_x and VOC controls on surface ozone formation. *Atmos. Environ*. **2010**, *44*(18), 2213-2223.

Duncan, B. N.; Lamsal, L. N.; Thompson, A. M.; Yoshida, Y.; Lu, Z.; Streets, D. G.; Hurwitz, M. M.; Pickering, K. E. A space-based, high-resolution view of notable changes in urban NO_x pollution around the world (2005–2014). *J. Geophys. Res.* **2016**, *121* (2), 976– 996, https://doi.org/10.1002/2015JD024121.

Dunker, A. M.; Koo, B.; Yarwood, G. Contributions of foreign, domestic and natural emissions to US ozone estimated using the path-integral method in CAMx nested within GEOS-Chem. *Atmos. Chem. Phys*. **2017**, *17*(20), 12553–12571.

Emery, C.; Jung, J.; Downey, N.; Johnson, J.; Jimenez, M.; Yarwood, G.; Morris, R. Regional and global modeling estimates of policy relevant background ozone over the United States. *Atmos. Environ*. **2012**, *47*, 206-217.

Air quality criteria for ozone and related photochemical oxidants. Environmental Protection Agency Office of Research and Development, Washington, D.C., 2006; http://cfpub.epa.gov/ncea/cfm/recordisplay.cfm?deid¼149923.

Fan, J.; Zhang, R. Atmospheric Oxidation Mechanism of Isoprene. *Environ. Chem*. **2004**, *1*, 140−149.

Feiner, P.A.; Brune, W.H.; Miller, D.O., Zhang; L., Cohen, R.C.; Romer, P.S.; Goldstein; A.H., Keutsch, F.N.; Skog, K.M.; Wennberg, P.O.; Nguyen, T.B. Testing atmospheric oxidation in an Alabama forest. *J. Atmos. Sci*. **2016**, *73*(12), 4699-4710.

Fiore, A. M.; Jacob, D. J.; Bey, I.; Yantosca, R. M.; Field, B. D.; Fusco, A. C.; Wilkinson, J. G. Background ozone over the United States in summer: Origin, trend, and contribution to pollution episodes. *J. Geophys. Res.: Atmos*. **2002**, *107*(D15), ACH-11.

Fiore, A.; Jacob, D. J.; Liu, H.; Yantosca, R. M.; Fairlie, T. D.; Li, Q. Variability in surface ozone background over the United States: Implications for air quality policy. *J. Geophys. Res.: Atmos*. **2003**, *108*(D24).

Fiore, A.M.; Oberman, J.T.; Lin, M.Y.; Zhang, L.; Clifton, O.E.; Jacob, D.J.; Naik, V.; Horowitz, L.W.; Pinto, J.P.; Milly, G. Estimating North American background ozone in US surface air with two independent global models: Variability, uncertainties, and recommendations. *Atmos. Environ*. **2014**, *96*, 284-300.

Fisher, J. A.; Jacob, D. J.; Travis, K. R.; Kim, P. S.; Marais, E. A.; Chan Miller, C.; Yu, K.; Zhu, L.; Yantosca, R. M.; Sulprizio, M. P.; Mao, J.; Wennberg, P. O.; Crounse, J. D.; Teng, A. P.; Nguyen, T. B.; St. Clair, J. M.; Cohen, R. C.; Romer, P.; Nault, B. A.; Wooldridge, P. J.; Jimenez, J. L.; Campuzano-Jost, P.; Day, D. A.; Hu, W.; Shepson, P. B.; Xiong, F.; Blake, D. R.; Goldstein, A. H.; Misztal, P. K.; Hanisco, T. F.; Wolfe, G. M.; Ryerson, T. B.; Wisthaler, A.; Mikoviny, T. Organic nitrate chemistry and its implications for nitrogen budgets in an isoprene- and monoterpene-rich atmosphere: constraints from aircraft (SEAC4RS) and ground-based (SOAS) observations in the Southeast US. *Atmos. Chem. Phys.* **2016**, *16*, 5969– 5991, DOI: 10.5194/acp-16-5969-2016.

Fowler, D.; Pilegaard, K.; Sutton, M. A.; Ambus, P.; Raivonen, M.; Duyzer, J.; Simpson, D.; Fagerli, H.; Fuzzi, S.; Schjoerring, J. K.; Granier, C.; Neftel, A.; Isaksen, I. S. A.; Laj, P.; Maione, M.; Monks, P. S.; Burkhardt, J.; Daemmgen, U.; Neirynck, J.; Personne, E.; Wichink-Kruit, R.; Butterbach-Bahl, K.; Flechard, C.; Tuovinen, J. P.; Coyle, M.; Gerosa, G.; Loubet, B.; Altimir, N.; Gruenhage, L.; Ammann, C.; Cieslik, S.; Paoletti, E.; Mikkelsen, T. N.; Ro-Poulsen, H.; Cellier, P.; Cape, J. N.; Horvath, L.; Loreto, F.; Niinemets, U.; Palmer, P. I.; Rinne, J.; Misztal, P.; Nemitz, E.; Nilsson, D.; Pryor, S.; Gallagher, M. W.; Vesala, T.; Skiba, U.; Brueggemann, N.; Zechmeister-Boltenstern, S.; Williams, J.; O'Dowd, C.; Facchini, M. C.; de Leeuw, G.; Flossman, A.; Chaumerliac, N.; Erisman, J. W. Atmospheric composition change: Ecosystems-Atmosphere interactions. *Atmos. Environ.* **2009**, *43*, 5193-5267.

Guenther, A.; Baugh, W.; Davis, K.; Hampton, G.; Harley, P.; Klinger, L.; Vierling, L.; Zimmerman, P.; Allwine, E.; Dilts, S.; Lamb, B.; Westberg, H.; Baldocchi, D.; Geron, C.; Pierce, T. Isoprene fluxes measured by enclosure, relaxed eddy accumulation, surface-layer gradient, mixed-layer gradient, and mass balance techniques. *J. Geophys. Res.* **1996**, *101* (D15), 18555-18567.

Guenther, A. B.; Jiang, X.; Heald, C. L.; Sakulyanontvittaya, T.; Duhl, T.; Emmons, L. K.; Wang, X. The Model of Emissions of Gases and Aerosols from Nature version 2.1 (MEGAN2.1): an extended and updated framework for modeling biogenic emissions. *Geosci. Model Dev*. **2012**, *5* (6) 1471– 1492.

Gu, D. S.; Wang, Y. H.; Smeltzer, C.; Liu, Z. Reduction in NO_x emission trends over China: Regional and seasonal variations. *Environ. Sci. Technol*. **2013**, *47*(22), 12912−12919.

Gu, D.; Wang, Y.; Smeltzer, C.; Boersma, K. F. Anthropogenic emissions of NO_x over China: Reconciling the difference of inverse modeling results using GOME-2 and OMI measurements. *J. Geophys. Res.: Atmos*. **2014**, *119*(12), 7732-7740.

Gu, D.; Wang, Y.; Yin, R.; Zhang, Y.; Smeltzer, C. Inverse modelling of NO_x emissions over eastern China: uncertainties due to chemical non-linearity. *Atmos. Meas. Tech*. **2016**, *9*(10), 5193.

Hansen, D.A.; Edgerton, E.S.; Hartsell, B.E.; Jansen, J.J.; Kandasamy, N.; Hidy, G.M.; Blanchard, C.L. The southeastern aerosol research and characterization study: Part 1— Overview. *J. Air. Waste. Manag. Assoc*. **2003**, *53*(12), 1460-1471.

Henderson, B. H.; Akhtar, F.; Pye, H. O. T.; Napelenok, S. L.; Hutzell, W. T. A database and tool for boundary conditions for regional air quality modeling: description and evaluation. *Geosci. Model Dev*. **2014**, *7*(1), 339-360.

Hidy, G. M.; Blanchard, C. L.; Baumann, K.; Edgerton, E.; Tanenbaum, S.; Shaw, S.; Knipping, E.; Tombach, I.; Jansen, J.; Walters, J. Chemical climatology of the southeastern United States, 1999–2013. *Atmos. Chem. Phys*. **2014**, *14*, 11893– 11914.

Hirsch, A. I.; Munger, J. W.; Jacob, D. J.; Horowitz, L. W.; Goldstein, A. H. Seasonal variation of the ozone production efficiency per unit NO_x at Harvard Forest, Massachusetts. *J. Geophys. Res.: Atmos*. **1996**, *101*(D7), 12659-12666.

Holland, P. W.; Welsch, R. E. Robust Regression Using Iteratively Reweighted Least-Squares. Commun. *Stat. Theory Methods*. **1977**, *A6*, 813–827.

Holloway, J.S.; Jakoubek, R.O.; Parrish, D.D.; Gerbig, C.; Volz-Thomas, A.; Schmitgen, S.; Fried, A.; Wert, B.; Henry, B.; Drummond, J.R. Airborne intercomparison of vacuum ultraviolet fluorescence and tunable diode laser absorption measurements of tropospheric carbon monoxide. *J. Geophys. Res.: Atmos*. **2000**, *105*(D19), 24251-24261.

Honrath, R.E.; Owen, R.C.; Val Martin, M.; Reid, J.S.; Lapina, K.; Fialho, P.; Dziobak, M.P.; Kleissl, J.; Westphal, D.L. Regional and hemispheric impacts of anthropogenic and biomass burning emissions on summertime CO and O_3 in the North Atlantic lower free troposphere. *J. Geophys. Res.: Atmos*. **2004**, *109*(D24).

Hottle, J.R.; Huisman, A.J.; DiGangi, J.P.; Kammrath, A.; Galloway, M.M.; Coens, K.L.; Keutsch, F.N. A laser induced fluorescence-based instrument for in-situ measurements of atmospheric formaldehyde. *Environ. Sci. Technol*. **2009**, *43*(3), 790-795.

Horowitz, L. W.; Fiore, A. M.; Milly, G. P.; Cohen, R. C.; Perring, A.; Wooldridge, P. J.; Hess, P. G.; Emmons, L. K.; Lamarque, J.-F. Observational Constraints on the Chemistry of Isoprene Nitrates over the Eastern United States. *J. Geophys. Res*. **2007**, *112*, D12S08.

Houyoux, M. R.; Vukovich, J. M.; Coats, C. J.; Wheeler, N. J.; Kasibhatla, P. S. Emission inventory development and processing for the Seasonal Model for Regional Air Quality (SMRAQ) project. *J. Geophys. Res.: Atmos*. **2000**, *105*(D7), 9079-9090.

Huang, M.; Carmichael, G. R.; Chai, T.; Pierce, R. B.; Oltmans, S. J.; Jaffe, D. A.; Bowman, K. W.; Kaduwela, A.; Cai, C.; Spak, S. N.; Weinheimer, A. J.; Huey, L. G.; Diskin, G. S. Impacts of transported background pollutants on summertime western US air quality: Model evaluation, sensitivity analysis and data assimilation. *Atmos. Chem. Phys*. **2013**, *13*, 359−391.

Hudman, R. C.; Russell, A. R.; Valin, L. C.; Cohen, R. C. Interannual variability in soil nitric oxide emissions over the United States as viewed from space. *Atmos. Chem. Phys. Discuss*. **2010**, *10*(5), 13029-13053.

Hudman, R. C.; Moore, N. E.; Mebust, A. K.; Martin, R. V.; Russell, A. R.; Valin, L. C.; Cohen, R. C. Steps towards a mechanistic model of global soil nitric oxide emissions: implementation and space based-constraints. *Atmos. Chem. Phys*. **2012**, *12*, 7779-7795.

Huntrieser, H.; Heland, J.; Schlager, H.; Forster, C.; Stohl, A.; Aufmhoff, H.; Arnold, F.; Scheel, H.E.; Campana, M.; Gilge, S.; Eixmann, R. Intercontinental air pollution transport from North America to Europe: Experimental evidence from airborne measurements and surface observations. *J. Geophys. Res.: Atmos*. **2005**, *110*(D1).

Hurst, J. M.; Barket, D. J.; Herrera-Gomez, O.; Couch, T. L.; Shepson, P. B.; Faloona, I.; Tan, D.; Brune, W.; Westberg, H.; Lamb, B.; Biesenthal, T.; Young, V.; Goldstein, A.; Munger, J. W.; Thornberry, T.; Carroll, M. A. Investigation of the nighttime decay of isoprene. *J. Geophys. Res*. **2001**, *106*, 24335−24346.

Jaeglé, L.; Steinberger, L.; Martin, R. V.; Chance, K. Global partitioning of NOx sources using satellite observations: Relative roles of fossil fuel combustion, biomass burning, and soil emissions. *Faraday Discuss*. **2005**, *130*, 407−423.

Jaffe, D.A.; Cooper, O.R.; Fiore, A.M.; Henderson, B.H.; Tonnesen, G.S.; Russell, A.G.; Henze, D.K.; Langford, A.O.; Lin, M.; Moore, T. Scientific assessment of background ozone over the US: Implications for air quality management. *Elementa*. **2018**, *6*(1), 56.

Jenkin, M. E.; Young, J. C.; Rickard, A. R. The MCM v3. 3.1 degradation scheme for isoprene. *Atmos. Chem. Phys*. **2015**, *15*(20), 11433.

Jin, X.; Fiore, A. M.; Murray, L. T.; Valin, L. C.; Lamsal, L. N.; Duncan, B.; Tonnesen, G. S. Evaluating a Space-Based Indicator of Surface Ozone-NO_x-VOC Sensitivity Over Midlatitude Source Regions and Application to Decadal Trends. *J. Geophys. Res.: Atmos*. **2017**, *122*(19).

Jin, X.; Fiore, A.; Boersma, K. F.; Smedt, I. D.; Valin, L. Inferring Changes in Summertime Surface Ozone-NO_x-VOC Chemistry over US Urban Areas from Two Decades of Satellite and Ground-Based Observations. *Environ. Sci. Technol*. **2020**, *54*(11), 6518-6529.

Jordan, A.; Haidacher, S.; Hanel, G.; Hartungen, E.; Mark, L.; Seehauser, H.; Schottkowsky, R.; Sulzer, P.; Mark, T. D. A high resolution and high sensitivity proton-transfer-reaction time-of-flight mass spectrometer (PTR-TOF-MS). *Int. J. Mass. Spectrom*. **2009**, *286*, 122–128.

Kang, D.; Mathur, R.; Pouliot, G. A.; Gilliam, R. C.; Wong, D. C. Significant ground-level ozone attributed to lightning-induced nitrogen oxides during summertime over the Mountain West States. *npj Climate and Atmospheric Science*. **2020**, *3*(1), 1-7.

Kim, S.; Kim S.Y.; Lee, M.; Shim, H.; Wolfe, G.M.; Guenther, A.B.; He, A.; Hong, Y.; Han, J. Impact of isoprene and HONO chemistry on ozone and OVOC formation in a semirural South Korean forest. *Atmos. Chem. Phys*. **2015**, *15*, 4357–4371. doi: 10.5194/acp-15-4357-2015.

Kim S. W.; McDonald, B.C.; Baidar, S.; Brown, S. S.; Dube, B.; Ferrare, R. A.; Frost, G. J.; Harley, R. A.; Holloway, J. S.; Lee, H. J.; McKeen, S. A.; Neuman, J. A.; Nowak, J. B.; Oetjen, H.; Ortega, I.; Pollack, I. B.; Roberts, J. M.; Ryerson, T. B.; Scarino, A. J.; Senff, C. J.; Thalman, R.; Trainer, M.; Volkamer, R.; Wagner, N.; Washenfelder, R. A.; Waxman, E.; Young, C. J. Modeling the weekly cycle of NO_x and CO emissions and their impacts on O_3 in the Los Angeles-South Coast Air Basin during the CalNex 2010 field campaign. *J. Geophys. Res.: Atmos*. **2016**, *121*, 1340-1360.

Kleinman, L. I.; Daum, P. H.; Lee, Y. N.; Nunnermacker, L. J.; Springston, S. R.; Weinstein-Lloyd, J.; Rudolph, J. Ozone production efficiency in an urban area. *J. Geophys. Res.: Atmos.* **2002**, *107*(D23), ACH-23.

Krotkov, N. A.; McLinden, C. A.; Li, C.; Lamsal, L. N.; Celarier, E.A.; Marchenko, S.V.; Swartz, W.H.; Bucsela, E.J.; Joiner, J.; Duncan, B.N.; Boersma, K.F.; Veefkind, J.P.; Levelt, P.F.; Fioletov, V.E.; Dickerson, R.R.; He, H.; Lu, Z.; Streets, D.G. Aura OMI observations of regional SO_2 and NO_2 pollution changes from 2005 to 2015. *Atmos. Chem. Phys*. **2016**, *16*(7), 4605-4629.

Kurten, A.; Rondo, L.; Ehrhart, S.; Curtius, J. Performance of a corona ion source for measurement of sulfuric acid by chemical ionization mass spectrometry. *Atmos. Meas. Tech.* **2011**, *4*(3), 437-443.

Lamsal, L. N.; Martin, R. V.; Padmanabhan, A.; Van Donkelaar, A.; Zhang, Q.; Sioris, C. E.; Newchurch, M. J. Application of satellite observations for timely updates to global anthropogenic NO_x emission inventories. *Geophys. Res. Lett.* **2011**, *38*(5), L05810.

Lee, B. H.; Lopez-Hilfiker, F. D.; Mohr, C.; Kurtén, T.; Worsnop, D. R.; Thornton, J. A. An iodide-adduct high-resolution time-of-flight chemical-ionization mass spectrometer: application to atmospheric inorganic and organic compounds. *Environ. Sci. Technol*. **2014**, *48*, 6309– 6317, DOI: 10.1021/es500362a.

Lee, B. H.; Mohr, C.; Lopez-Hilfiker, F. D.; Lutz, A.; Hallquist, M.; Lee, L.; Romer, P.; Cohen, R. C.; Iyer, S.; Kurten, T.; Hu, W.; Day, D. A.;́ Campuzano-Jost, P.; Jimenez, J. L.; Xu, L.; Ng, N. L.; Guo, H.; Weber, R. J.; Wild, R. J.; Brown, S. S.; Koss, A.; de Gouw, J.; Olson, K.; Goldstein, A. H.; Seco, R.; Kim, S.; McAvey, K.; Shepson, P. B.; Starn, T.; Baumann, K.; Edgerton, E. S.; Liu, J.; Shilling, J. E.; Miller, D. O.; Brune, W.; Schobesberger, S.; D'Ambro, E. L.; Thornton, J. A. Highly functionalized organic nitrates in the southeast United States: Contribution to secondary organic aerosol and reactive nitrogen budgets. *Proc. Natl. Acad. Sci. U. S. A.* **2016**, *113* (6), 1516−1521.

Lefohn, A. S.; Emery, C.; Shadwick, D.; Wernli, H.; Jung, J.; Oltmans, S. J. Estimates of background surface ozone concentrations in the United States based on model-derived source apportionment. *Atmos. Environ*. **2014**, *84*, 275-288.

Lelieveld, J.; Dentener, F. J. What controls tropospheric ozone?. *J. Geophys. Res.: Atmos*. **2000**, *105*(D3), 3531-3551.

Levelt, P. F.; van den Oord, G. H. J.; Dobber, M. R.; Malkki, A.; Visser, H.; de Vries, J.; Stammes, P.; Lundell, J. O. V.; Saari, H. The ozone monitoring instrument. IEEE Trans. *Geosci. Remote Sens*. **2006**, *44*(5), 1093-1101.

Li, J.; Wang, Y. Inferring the anthropogenic NOx emission trend over the United States during 2003-2017 from satellite observations: was there a flattening of the emission trend after the Great Recession? *Atmos. Chem. Phys*. **2019**, *19*, 15339-15352.

Li, J.; Wang, Y.; Qu, H. Dependence of summertime surface ozone on NO_x and VOC emissions over the United States: Peak time and value, *Geophys. Res. Lett.* **2019**, *46*, https://doi.org/10.1029/2018GL081823.

Li, J.; Wang, Y.; Zhang, R.; Smeltzer, C.; Weinheimer, A.; Herman, J.; Boersma, K. F.; Celarier, E. A.; Long, R. W.; Szykman, J. J.; Delgado, R. Comprehensive evaluations of diurnal NO_2 measurements during DISCOVER-AQ 2011: Effects of resolution dependent representation of NO_x emissions. *Atmos. Chem. Phys. Discuss*. **2021**, 1-58.

Lin, M.; Fiore, A.M.; Horowitz, L.W.; Cooper, O.R.; Naik, V.; Holloway, J.; Johnson, B.J.; Middlebrook, A.M.; Oltmans, S.J.; Pollack, I.B.; Ryerson, T.B. Transport of Asian ozone pollution into surface air over the western United States in spring. *J. Geophys. Res.: Atmos*. **2012**, *117*(D21).

Lin, M.; Fiore, A. M.; Horowitz, L. W.; Langford, A. O.; Oltmans, S. J.; Tarasick, D.; Rieder, H. E. Climate variability modulates western US ozone air quality in spring via deep stratospheric intrusions. *Nat. Commun*. **2015**, *6*(7105).

Lin, M.; Horowitz, L. W.; Payton, R.; Fiore, A. M.; Tonnesen, G. US surface ozone trends and extremes from 1980 to 2014: quantifying the roles of rising Asian emissions, domestic controls, wildfires, and climate. *Atmos. Chem. Phys*. **2017**, *17*(4).

Lin, J. T.; McElroy, M. B. Impacts of boundary layer mixing on pollutant vertical profiles in the lower troposphere: Implications to satellite remote sensing. *Atmos. Environ.* **2010**, *44*(14), 1726-1739.

Lin, J. T. Satellite constraint for emissions of nitrogen oxides from anthropogenic, lightning and soil sources over East China on a high-resolution grid. *Atmos. Chem. Phys*. **2012**, *12*(6), 2881-2898.

Liu, S.C.; Trainer, M.; Fehsenfeld, F.C.; Parrish, D.D.; Williams, E.J.; Fahey, D.W.; Hübler, G.; Murphy, P.C. Ozone production in the rural troposphere and the implications for regional and global ozone distributions. *J. Geophys. Res.: Atmos*. **1987**, *92*(D4), 4191-4207.

Liu, Y. J.; Herdlinger-Blatt, I.; McKinney, K. A.; Martin, S. T. Production of methyl vinyl ketone and methacrolein via the hydroperoxyl pathway of isoprene oxidation. *Atmos. Chem. Phys*. **2013**, *13*(11), 5715−5730.

Liu, X. A more accurate method using MOVES (Motor Vehicle Emission Simulator) to estimate emission burden for regional-level analysis. *J. Air. Waste. Manag. Assoc*. **2015**, *65*(7), 837-843.

Liu, Z.; Wang, Y.; Gu, D.; Zhao, C.; Huey, L. G.; Stickel, R.; Liao, J.; Shao, M.; Zhu, T.; Zeng, L.; Amoroso, A.; Costabile, F.; Chang, C. C.; Liu, S. C. Summertime photochemistry during CAREBeijing-2007: RO_x budgets and O3 formation. *Atmos. Chem. Phys*. **2012**, *12*(16) 7737– 7752.

Liu, Z.; Wang, Y. H.; Gu, D. S.; Zhao, C.; Huey, L. G.; Stickel, R.; Liao, J.; Shao, M.; Zhu, T.; Zeng, L. M.; Liu, S. C.; Chang, C. C.; Amoroso, A.; Costabile, F. Evidence of reactive aromatics as a major source of peroxy acetyl nitrate over China. *Environ. Sci. Technol*. **2010**, *44* (18) 7017– 7022.

Liu, Z.; Wang, Y. H.; Vrekoussis, M.; Richter, A.; Wittrock, F.; Burrows, J. P.; Shao, M.; Chang, C. C.; Liu, S. C.; Wang, H. L., Exploring the missing source of glyoxal (CHOCHO) over China. *Geophys. Res. Lett*. **2012**, *39*.

Liu, Z.; Wang, Y.; Costabile, F.; Amoroso, A.; Zhao, C.; Huey, L.G.; Stickel, R.; Liao, J.; Zhu, T. Evidence of aerosols as a media for rapid daytime HONO production over China. *Environ. Sci. Technol*. **2014**, *48*(24), 14386-14391.

Lockwood, A. L.; Shepson, P. B.; Fiddler, M. N.; Alaghmand, M. Isoprene nitrates: Preparation, separation, identification, yields, and atmospheric chemistry. *Atmos. Chem. Phys*. **2010**, *10*, 6169– 6178.

Logan, J. A.; Prather, M. J.; Wofsy, S. C.; McElroy, M. B. Tropospheric chemistry: A global perspective. *J. Geophys. Res.: Oceans*. **1981**, *86*(C8), 7210-7254.

Lopez-Hilfiker, F. D.; Mohr, C.; Ehn, M.; Rubach, F.; Kleist, E.; Wildt, J.; Mentel, T. F.; Lutz, A.; Hallquist, M.; Worsnop, D.; Thornton, J. A. A novel method for online analysis of gas and particle composition: Description and evaluation of a Filter Inlet for Gases and AEROsols (FIGAERO). *Atmos. Meas. Tech*. **2014**, *7*(4), 983−1001.

Lorente, A.; Boersma, K. F.; Yu, H.; Dörner, S.; Hilboll, A.; Richter, A.; Liu, M.; Lamsal, L. N.; Barkley, M.; De Smedt, I.; Van Roozendael, M.; Wang, Y.; Wagner, T.; Beirle, S.; Lin, J.-T.; Krotkov, N.; Stammes, P.; Wang, P.; Eskes, H. J.; Krol, M. Structural uncertainty in air mass factor calculation for NO_2 and HCHO satellite retrievals. *Atmos. Meas. Tech*. **2017**, *10*, 759-782.

Lorente, A.; Boersma, K. F.; Eskes, H. J.; Veefkind, J. P.; van Geffen, J. H. G. M.; de Zeeuw, M. B.; Denier van der Gon, H. A. C.; Beirle, S.; Krol, M. C. Quantification of nitrogen oxides emissions from build-up of pollution over Paris with TROPOMI. *Sci. Rep*. **2019**, *9*, 20033, https://doi.org/10.1038/s41598-019-56428-5, 2019.

Luo, C.; Wang,Y.; Koshak,W. J. Development of a self-consistent lightning NOx simulation in large-scale 3-D models. *J. Geophys. Res.: Atmos*. **2017**, *122*(5), 3141-3154.

Makar, P. A.; Fuentes, J. D.; Wang, D.; Staebler, R. M.; Wiebe, H. A. Chemical processing of biogenic hydrocarbons within and above a temperate deciduous forest. *J. Geophys. Res*. **1999**, *104*, 3581−3603.

Mao, H.; Talbot, R. O_3 and CO in New England: Temporal variations and relationships. *J. Geophys. Res.: Atmos*. **2004**, *109*(D21).

Mao, J.; Ren, X.; Brune, W.; Olson, J.; Crawford, J.; Fried, A.; Huey, L.; Cohen, R.; Heikes, B.; Singh, H. Airborne measurement of OH reactivity during INTEX-B. *Atmos. Chem. Phys*. **2009**, *9*, 163– 173.

Mao, J.; Paulot, F.; Jacob, D. J.; Cohen, R. C.; Crounse, J. D.; Wennberg, P. O.; Keller, C. A.; Hudman, R. C.; Barkley, M. P.; Horowitz, L. W. Ozone and Organic Nitrates over the Eastern United States: Sensitivity to Isoprene Chemistry. *J. Geophys. Res. Atmos*. **2013**, *118*, 11256−11268.

Martin, R. V.; Jacob, D. J.; Chance, K.; Kurosu, T. P.; Palmer, P. I.; Evans, M. J. Global inventory of nitrogen oxide emissions constrained by space-based observations of NO_2 columns. *J. Geophys. Res*. **2003**, *108*(D17), 4537.

Mijling, B.; Ding, J.; Koukouli, M. E.; Liu, F.; Li, Q.; Mao, H.; Theys, N. Cleaning up the air: effectiveness of air quality policy for SO_2 and NO_x emissions in China. *Atmos. Chem. Phys*. **2017**, *17*(3), 1775-1789.

Millet, D. B.; Baasandorj, M.; Hu, L.; Mitroo, D.; Turner, J.; Williams, B. J. Nighttime chemistry and morning isoprene can drive daytime ozone downwind of a major deciduous forest. *Environ. Sci. Technol*. **2016**, *50*(8) 4335– 4342.

Monks, P. S.; Archibald, A. T.; Colette, A.; Cooper, O.; Coyle, M.; Derwent, R.; Fowler, D.; Granier, C.; Law, K. S.; Mills, G. E.; Stevenson, D. S.; Tarasova, O.; Thouret, V.; von Schneidemesser, E.; Sommariva, R.; Wild, O.; Williams, M. L.

Tropospheric ozone and its precursors from the urban to the global scale from air quality to short-lived climate forcer. *Atmos. Chem. Phys*. **2015**, *15*(15), 8889-8973.

Montzka, S. A.; Trainer, M.; Goldan, P. D.; Kuster, W. C.; Fehsenfeld, F. C. Isoprene and its oxidation products, methyl vinyl ketone and methacrolein, in the rural troposphere. *J. Geophys. Res.: Atmos*. **1993**, *98*, 1101– 1111.

National Ambient Air Quality Standards for Ozone; U.S. Environmental Protection Agency: Triangle Park, NC, 2015; https://www.govinfo.gov/content/pkg/FR-2020-08-14/pdf/2020-15453.pdf.

Ng, N. L.; Kwan, A. J.; Surratt, J. D.; Chan, A. W. H.; Chhabra, P. S.; Sorooshian, A.; Pye, H. O. T.; Crounse, J. D.; Wennberg, P. O.; Flagan, R. C.; et al. Secondary Organic Aerosol (SOA) Formation from Reaction of Isoprene with Nitrate Radicals (NO_3). *Atmos. Chem. Phys*. **2008**, *8*, 4117−4140.

Nguyen, T. B.; Crounse, J. D.; Teng, A. P.; St. Clair, J. M.; Paulot, F.; Wolfe, G. M.; Wennberg, P. O. Rapid deposition of oxidized biogenic compounds to a temperate forest. *Proc. Natl. Acad. Sci.* **2015**, *112*, E392−E401.

Ninneman, M.; Demerjian, K. L.; Schwab, J. J. Ozone production efficiencies at rural New York state locations: Relationship to oxides of nitrogen concentrations. *J. Geophys. Res.: Atmos.* **2019**, *124*, 2363–2376.

Non-EGU Emissions Reductions Cost and Potential; EPA-HQ-OAR-2009-0491; U.S. Environmental Protection Agency Office of Air and Radiation: Washington, DC, 2010; https://www.epa.gov/sites/production/files/2017-06/documents/epa-hq-oar-2009-0491-0044.pdf.

Oltmans, S. J.; Lefohn, A. S.; Harris, J. M.; Shadwick, D. S. Background ozone levels of air entering the west coast of the U.S. and assessment of longer-term changes. *Atmos. Environ*. **2008**, *42*, DOI: 10.1016/j.atmosenv.2008.03.034, 6020– 6038.

Orville, R. E. Development of the National Lightning Detection Network. *B. Am, Meteorol. Soc*. **2008**, *89*, 180-190.

Ott, L. E.; Pickering, K. E.; Stenchikov, G. L.; Huntrieser, H.; Schumann, U. Effects of lightning NOx production during the 21 July European Lightning Nitrogen

Oxides Project storm studied with a three-dimensional cloud-scale chemical transport model. *J. Geophys. Res.: Atmos*. **2007**, *112*, D05307.

Pai, S. J.; Heald, C. L.; Pierce, J. R.; Farina, S. C.; Marais, E. A.; Jimenez, J. L.; Campuzano-Jost, P.; Nault, B. A.; Middlebrook, A. M.; Coe, H.; Shilling, J. E.; Bahreini, R.; Dingle, J. H.; Vu, K. An evaluation of global organic aerosol schemes using airborne observations. *Atmos. Chem. Phys*. **2020**, *20*, 2637–2665.

Parrish, D. D.; Holloway, J. S.; Trainer, M.; Murphy, P. C.; Fehsenfeld, F. C.; Forbes, G. L. Export of North American ozone pollution to the north Atlantic Ocean. *Science*. **1993**, *259*(5100), 1436-1439.

Parrish, D.D.; Trainer, M.; Holloway, J.S.; Yee, J.E.; Warshawsky, M.S.; Fehsenfeld, F.C.; Forbes, G.L.; Moody, J.L. Relationships between ozone and carbon monoxide at surface sites in the North Atlantic region. *J. Geophys. Res.: Atmos*. **1998**, *103*(D11), 13357-13376.

Parrish, D. D.; Young, L. M.; Newman, M. H.; Aikin, K. C.; Ryerson, T. B. Ozone designvalues in Southern California's air basins: Temporal evolution and U.S. back-ground contribution. *J. Geophys. Res.: Atmos*. **2017**, *122*, 11166–11182.

Parrish, D. D.; Ennis, C. A. Estimating background contributions and US anthropogenic enhancements to maximum ozone concentrations in the northern US. *Atmos. Chem. Phys*. **2019**, *19*(19), 12587-12605.

Paulot, F.; Crounse, J. D.; Kjaergaard, H. G.; Kroll, J. H.; Seinfeld, J. H.; Wennberg, P. O. Isoprene photooxidation: New insights into the production of acids and organic nitrates. *Atmos. Chem. Phys*. **2009**, *9*(4) 1479– 1501.

Paulson, S. E.; Seinfeld, J. H. Development and evaluation of a photooxidation mechanism for isoprene. *J. Geophys. Res*. **1992**, *97*, 20703– 20715.

Platt, U.; Le Bras, G.; Poulet, G.; Burrow, J. P.; Moortgart, G. Peroxy radicals from night-time reaction of NO3 with organic compounds. *Nature*. **1990**, *348*, 147-149.

Pollack, I.B.; Lerner, B.M.; Ryerson, T.B. Evaluation of ultraviolet light-emitting diodes for detection of atmospheric NO_2 by photolysis-chemiluminescence. *J. Atmos. Chem*. **2010**, *65*(2-3), 111-125.

Pickering, K. E.; Wang, Y.; Tao, W. K.; Price, C.; Müller, J. F. Vertical distributions of lightning NO_x for use in regional and global chemical transport models. *J. Geophys. Res.: Atmos.* **1998**, *103*(D23), 31203-31216.

Pickering, K. E.; Bucsela, E.; Allen, D.; Ring, A.; Holzworth, R.; Krotkov, N. Estimates of lightning NO_x production based on OMI NO_2 observations over the Gulf of Mexico. *J. Geophys. Res.: Atmos*. **2016**, *121*(14), 8668-8691.

Piletic, I. R.; Edney, E. O.; Bartolotti, L. J. Barrierless Reactions with Loose Transition States Govern the Yields and Lifetimes of Organic Nitrates Derived from Isoprene. *J. Phys. Chem. A.* **2017**, *121*(43), 8306-8321.

Qu, H.; Wang, Y.; Zhang, R.; Li, J. Extending ozone-precursor relationships in China from peak concentration to peak time. *J. Geophys. Res*. **2020**, *125*, e2020JD033670, https://doi.org/10.1029/2020JD033670.

Qu, Z.; Henze, D. K.; Capps, S. L.; Wang, Y.; Xu, X.; Wang, J.; Keller, M. Monthly top-down NOx emissions for China (2005–2012): A hybrid inversion method and trend analysis. *J. Geophys. Res.: Atmos*. **2017**, *122*(8), 4600-4625.

Ridley, B.; Ott, L.; Pickering, K.; Emmons, L.; Montzka, D.; Weinheimer, A.; Knapp, D.; Grahek, F.; Li, L.; Heymsfield, G.; McGill, M.; Kucera, P.; Mahoney, M. J.; Baumgardner, D.; Schultz, M.; Brasseur, G. Florida thunderstorms: A faucet of reactive nitrogen to the upper troposphere. *J. Geophys. Res.: Atmos*. **2004**, *10*9, D17305.

Rollins, A. W.; Kiendler-Scharr, A.; Fry, J. L.; Brauers, T.; Brown, S. S.; Dorn, H.-P.; Dube´, W. P.; Fuchs, H.; Mensah, A.; Mentel, T. F.; Rohrer, F.; Tillmann, R.; Wegener, R.; Wooldridge, P. J.; Cohen, R. C. Isoprene oxidation by nitrate radical: alkyl nitrate and secondary organic aerosol yields. *Atmos. Chem. Phys*. **2009**, *9*, 6685–6703.

Russell, A. R.; Valin, L. C.; Cohen, R. C. Trends in OMI NO_2 observations over the United States: effects of emission control technology and the economic recession. *Atmos. Chem. Phys*. **2012**, *12*(24), 12197-12209.

Ruckstuhl, A. Introduction to nonlinear regression; Zurcher Hochschule fur Angewandte Wissenschaften: Winterthur, Switzerland, 2010.

Ryerson, T.B.; Huey, L.G.; Knapp, K.; Neuman, J.A.; Parrish, D.D.; Sueper, D.T.; Fehsenfeld, F.C. Design and initial characterization of an inlet for gas-phase NO_y measurements from aircraft. *J. Geophys. Res.: Atmos*. **1999**, *104*(D5), 5483-5492.

Schumann, U.; Huntrieser, H. The global lightning-induced nitrogen oxides source. *Atmos. Chem. Phys*. **2007**, *7*(14), 3823-3907.

Sharkey, T. D.; Singsaas, E. L. Why plants emit isoprene. *Nature*. **1995**, *374*(6525), 769-769.

Sharma, S.; Sharma, P.; Khare, M. Photo-chemical transport modelling of tropospheric ozone: A review. *Atmos. Environ*. **2017**, *159*, 34-54.

Starn, T. K.; Shepson, P. B.; Bertman, S. B.; Riemer, D. D.; Zika, R. G.; Olszyna, K. Nighttime Isoprene Chemistry at an Urban-Impacted Forest Site. *J. Geophys. Res. - Atmos*. **1998**, *103*, 22437−22447.

Stavrakou, T.; Müller, J. F.; Boersma, K. F.; De Smedt, I.; van der A, R. J. Assessing the distribution and growth rates of NO_x emission sources by inverting a 10-year record of NO_2 satellite columns. *Geophys. Res. Lett*. **2008**, *35*, L10801.

Sillman, S.; Logan, J. A.; Wofsy, S. C. The sensitivity of ozone to nitrogen oxides and hydrocarbons in regional ozone episodes. *J. Geophys. Res. Atmos*. **1990**, *95*(D2), 1837-1851.

Sillman, S.; Carroll, M. A.; Thornberry, T.; Lamb, B. K.; Westberg, H.; Brune, W. H.; Faloona, I.; Tan, D.; Shepson, P. B.; Sumner, A. L.; et al. Loss of Isoprene and Sources of Nighttime OH Radicals at a Rural Site in the United States: Results from Photochemical Models. *J. Geophys. Res.: Atmos*. **2002**, *107*, ACH-2− 1-ACH 2-14.

Simon, H.; Reff, A.; Wells, B.; Xing, J.; Frank, N. Ozone trends across the United States over a period of decreasing NO_x and VOC emissions. *Environ. Sci. Technol*. **2015**, *49*(1), 186-195.

Sinha, V.; Williams, J.; Crowley, J. N.; Lelieveld, J. The comparative reactivity method - a new tool to measure total OH reactivity in ambient air. *Atmos. Chem. Phys*. **2008**, *8*, 2213–2227.

Souri, A. H.; Choi, Y.; Jeon, W.; Li, X.; Pan, S.; Diao, L.; Westenbarger, D. A. Constraining NO_x emissions using satellite NO_2 measurements during 2013 DISCOVER-AQ Texas campaign. *Atmos. Environ*. **2016**, *131*, 371-381.

Souri, A. H.; Choi, Y.; Jeon, W.; Woo, J. H.; Zhang, Q.; Kurokawa, J. I. Remote sensing evidence of decadal changes in major tropospheric ozone precursors over East Asia. *J. Geophys. Res.: Atmos*. **2017**, *122*(4), 2474-2492.

Spiess, A. N.; Neumeyer, N. An evaluation of R^2 as an inadequate measure for nonlinear models in pharmacological and biochemical research: a Monte Carlo approach. *BMC pharmacology*. **2010**, *10*(1), 1-11.

Starn, T. K.; Shepson, P. B.; Bertman, S. B.; Riemer, D. D.; Zika, R. G.; Olszyna, K. Nighttime Isoprene Chemistry at an Urban-Impacted Forest Site. *J. Geophys. Res. - Atmos*. **1998**, *103*, 22437−22447.

Streets, D. G.; Bond, T. C.; Carmichael, G. R.; Fernandes, S. D.; Fu, Q.; He, D.; Klimont, Z.; Nelson, S. M.; Tsai, N. Y.; Wang, M. Q.; Woo, J.-H.; Yarber, K. F. An inventory of gaseous and primary aerosol emissions in Asia in the year 2000. *J. Geophys. Res*. **2003**, *108* (D21), 8809, doi: 10.1029/2002JD003093.

Stroud, C. A.; Roberts, J. M.; Williams, E. J.; Hereid, D.; Angevine, W. M.; Fehsenfeld, F. C.; Wisthaler, A.; Hansel, A.; artinez- Harder, M.; Harder, H.; et al. Nighttime Isoprene Trends at an Urban Forested Site during the 1999 Southern Oxidant Study. *J. Geophys. Res*. **2002**, *107*, ACH 7-1−ACH 7-14.

Technical Guidance on the Use of MOVES2010 for Emission Inventory Preparation in State Implementation Plans and Transportation Conformity; EPA-420-B-10-023; U.S. Environmental Protection Agency Public Information Services: Ann Arbor, MI, 2015; www.epa.gov/otaq/models/moves/documents/420b15007.pdf.

Technical Support Document (TSD) Preparation of Emissions Inventories for the Version 6.3, 2011 Emissions Modeling Platform; U.S. Environmental Protection Agency Office of Air Quality Planning and Standards Air Quality Assessment Division Emissions Inventory and Analysis Group Research: Triangle Park, NC, 2016; https://www.epa.gov/sites/production/files/2016-09/documents/2011v6_3_2017_emismod_tsd_aug2016_final.pdf

Tong, D. Q.; Lamsal, L.; Pan, L.; Ding, C.; Kim, H.; Lee, P.; Stajner, I. Long-term NO_x trends over large cities in the United States during the great recession:

Comparison of satellite retrievals, ground observations, and emission inventories. *Atmos. Environ*. **2015**, *107*, 70-84.

Trainer, M.; Williams, E. J.; Parrish, D. D.; Buhr, M. P.; Allwine, E. J.; Westberg, H. H.; Fehsenfeld, F. C.; Liu, S. C. Models and observations of the impact of natural hydrocarbons on rural ozone. *Nature.* **1987**, 3*29* (6141) 705– 707 DOI: 10.1038/329705a0

Trainer, M.; Parrish, D. D.; Buhr, M. P.; Norton, R. B.; Fehsenfeld, F. C.; Anlauf, K. G.; Bottenheim, J. W.; Tang, Y. Z.; Wiebe, H. A.; Roberts, J. M.; et al. Correlation of ozone with NO_y in photochemically aged air. *J. Geophys. Res.: Atmos*. **1993**, *98* (D2), 2917−2925.

Travis, K. R.; Jacob, D. J.; Fisher, J. A.; Kim, P. S.; Marais, E. A.; Zhu, L.; Yu, K.; Miller, C. C.; Yantosca, R. M.; Sulprizio, M. P.; Thompson, A. M.; Wennberg, P. O.; Crounse, J. D.; St. Clair, J. M.; Cohen, R. C.; Laugher, J. L.; Dibb, J. E.; Hall, S. R.; Ullmann, K.; Wolfe, G. M.; Pollack, I. B.; Peischl, J.; Neuman, J. A.; Zhou, X. NO_x emissions, isoprene oxidation pathways, vertical mixing, and implications for surface ozone in the Southeast United States. *Atmos. Chem. Phys*. **2016**, *2016*, 1–32.

Tuazon, E. C.; Atkinson, R. A product study of the gas-phase reaction of Isoprene with the OH radical in the presence of NO_x. *Int. J. Chem. Kinet*. **1990**, *22*(12), 1221-1236.

Van Geffen, J.; Boersma, K. F.; Eskes, H.; Sneep, M.; Ter Linden, M.; Zara, M.; Veefkind, J. P. S5P TROPOMI NO_2 slant column retrieval: method, stability, uncertainties and comparisons with OMI. *Atmos. Meas. Tech.* **2020**, *13*(3), 1315-1335.

Vingarzan, R. A review of surface ozone background levels and trends. *Atmos. Environ*. **2004**, *38*(21), 3431-3442.

Vinken, G. C. M.; Boersma, K. F.; Maasakkers, J. D.; Adon, M.; Martin, R. V. Worldwide biogenic soil NO_x emissions inferred from OMI NO_2 observations. *Atmos. Chem. Phys*. **2014**, *14*(18), 10363-10381.

von Kuhlmann, R.; Lawrence, M. G.; Poschl, U.; Crutzen, P. J. Sensitivities in Global Scale Modeling of Isoprene. *Atmos. Chem. Phys*. **2004**, *4*, 1−17.

Wang, Y.; Jacob, D. J. Anthropogenic forcing on tropospheric ozone and OH since preindustrial times. *J. Geophys. Res.: Atmos.* **1998**, *103*(D23), 31123-31135.

Wang, Y.; Jacob, D. J.; Logan, J. A. Global simulation of tropospheric O_3-NO_x-hydrocarbon chemistry: 3. Origin of tropospheric ozone and effects of nonmethane hydrocarbons. *J. Geophys. Res.: Atmos*. **1998**, *103*(D9), 10757-10767.

Wang, Y.; McElroy, M. B.; Martin, R. V.; Streets, D. G.; Zhang, Q.; Fu, T. M. Seasonal variability of NO_x emissions over east China constrained by satellite observations: Implications for combustion and microbial sources. *J. Geophys. Res.: Atmos*. **2007**, *112*, D06301.

Washenfelder, R. A.; Attwood, A. R.; Brock, C. A.; Guo, H.; Xu, L.; Weber, R. J.; Ng, N. L.; Allen, H. M.; Ayres, B. R.; Baumann, K.; Cohen, R. C.; Draper, D. C.; Duffey, K. C.; Edgerton, E.; Fry, J. L.; Hu, W. W.; Jimenez, J. L.; Palm, B. B.; Romer, P.; Stone, E. A.; Wooldridge, P. J.; Brown, S. S. Biomass burning dominates brown carbon absorption in the rural southeastern United States. *Geophys. Res. Lett*. **2015**, *42*, 653−664.

Wennberg, P. O.; Bates, K. H.; Crounse, J. D.; Dodson, L. G.; McVay, R. C.; Mertens, L. A.; Nguyen, T. B.; Praske, E.; Schwantes, R. H.; Smarte, M. D. Gas-Phase Reactions of Isoprene and Its Major Oxidation Products. *Chem. Rev*. **2018**, *118*, 3337– 3390, DOI: 10.1021/acs.chemrev.7b00439.

Williams, J. E.; Boersma, K. F.; Sager, P. L.; Verstraeten, W. W. The high-resolution version of TM5-MP for optimized satellite retrievals: description and validation. *Geosci. Model. Dev*. **2017**, *10*(2), 721-750.

Wilson, R.C.; Fleming, Z.L.; Monks, P.S.; Clain, G.; Henne, S.; Konovalov, I.B.; Szopa, S.; Menut, L. Have primary emission reduction measures reduced ozone across Europe? An analysis of European rural background ozone trends 1996–2005. *Atmos. Chem. Phys*. **2012**, *12*(1), 437-454.

Wu, S. L.; Duncan, B. N.; Jacob, D. J.; Fiore, A. M.; Wild, O. Chemical nonlinearities in relating intercontinental ozone pollution to anthropogenic emissions. *Geophys. Res. Lett*. **2009**, *36*(L05), 806, DOI: 10.1029/2008GL036607.

Xiong, F.; McAvey, K. M.; Pratt, K. A.; Groff, C. J.; Hostetler, M. A.; Lipton, M. A.; Starn, T. K.; Seeley, J. V.; Bertman, S. B.; Teng, A. P.; Crounse, J. D.; Nguyen, T. B.; Wennberg, P. O.; Misztal, P. K.; Goldstein, A. H.; Guenther, A. B.; Koss, A. R.; Olson, K. F.; de Gouw, J. A.; Baumann, K.; Edgerton, E. S.; Feiner, P. A.; Zhang, L.; Miller, D. O.; Brune, W. H.; Shepson, P. B. Observation of isoprene hydroxynitrates in the southeastern United States and implications for the fate of

NOx. *Atmos. Chem. Phys*. **2015**, *15*(19) 11257– 11272 DOI: 10.5194/acp-15-11257-2015.

Xu, L.; Guo, H.; Boyd, C. M.; Klein, M.; Bougiatioti, A.; Cerully, K. M.; Hite, J. R.; Isaacman-VanWertz, G.; Kreisberg, N. M.; Knote, C.Effects of anthropogenic emissions on aerosol formation from isoprene and monoterpenes in the southeastern United States. *Proc. Natl. Acad. Sci. U. S. A.* **2015**, *112* (1) 37– 42 DOI: 10.1073/pnas.1417609112.

Yienger, J. J.; Levy, H. Empirical model of global soil-biogenic NO_x emissions. *J. Geophys. Res.: Atmos*. **1995**, *100*(D6), 11447-11464.

Zeng, T.; Wang, Y.; Chance, K.; Browell, E. V.; Ridley, B. A.; Atlas, E. L. Widespread persistent near-surface ozone depletion at northern high latitudes in spring. *Geophys. Res. Lett*. **2003**, *30*, 2298, DOI: DOI: 10.1029/2003GL018587.

Zhang, L.; Jiang, H.; Lu, X.; Jin, J. Comparison analysis of global carbon monoxide concentration derived from SCIAMACHY, AIRS, and MOPITT. *Int. J. Remote Sens.* **2016**, *37*(21), 5155-5175.

Zhang, L.; Jacob, D. J.; Downey, N. V.; Wood, D. A.; Blewitt, D.; Carouge, C. C.; van Donkelaar, A.; Jones, D. B.; Murray, L. T.; Wang, Y. Improved estimate of the policy-relevant background ozone in the United States using the GEOS-Chem global model with 1/2×2/3 horizontal resolution over North America. *Atmos. Environ*. **2011**, *45*(37), 6769-6776.

Zhang, R., Y.; Wang, Q.; He, L.; Chen, Y.; Zhang, H.; Qu, C.; Smeltzer; Li, J.; Alvarado, L.; Vrekoussis, M. Enhanced trans-Himalaya pollution transport to the Tibetan Plateau by cut-off low systems. *Atmos. Chem. Phys*. **2017**, *17*(4), 3083- 3095.

Zhang, R.; Wang, Y.; Smeltzer, C.; Qu, H.; Koshak, W.; Boersma, K. F. Reconciling the differences between OMI-based and EPA AQS in situ NO_2 trends. *Atmos. Meas. Tech*. **2018**, 1-26.

Zhang, Y.; Wang, Y. Climate-driven ground-level ozone extreme in the fall over the Southeast United States. *Proc. Natl. Acad. Sci*. **2016**, *113*(36), 10025-10030.

Zhang, Y.; Wang, Y.; Chen, G.; Smeltzer, C.; Crawford, J.; Olson, J.; Szykman, J.; Weinheimer, A.J.; Knapp, D.J.; Montzka, D.D.; Wisthaler, A. Large vertical gradient of reactive nitrogen oxides in the boundary layer: Modeling analysis of

DISCOVER-AQ 2011 observations. *J. Geophys. Res.: Atmos*. **2016**, *121*(4), 1922-1934.

Zhao, C.; Wang, Y. Assimilated inversion of NO_x emissions over East Asia using OMI NO2 column measurements. *Geophys. Res. Lett*. **2009**, *36*(6), L06805.

Zhao, C.; Wang, Y.; Choi, Y.; Zeng, T. Summertime impact of convective transport and lightning NO_x production over North America: modeling dependence on meteorological simulations. *Atmos. Chem. Phys*. **2009**, *9*(13), 4315-4327.

Zhao, C.; Wang, Y.; Zeng, T. East China plains: A "basin" of ozone pollution, *Environ. Sci. Technol*. **2009**, *43*(6), 1911-1915, doi:10.1021/es8027764.

Zhao, C.; Wang, Y.; Yang, Q.; Fu, R.; Cunnold, D.; Choi, Y. Impact of East Asian summer monsoon on the air quality over China: View from space. *J. Geophys. Res.: Atmos.* **2010**, *115*(D9).

2011 National Emissions Inventory, version 2 Technical Support Document; U.S. Environmental Protection Agency Office of Air Quality Planning and Standards Air Quality Assessment Division Emissions Inventory and Analysis Group Research: Triangle Park, NC, 2015; https://www.epa.gov/sites/production/files/2015-10/documents/nei2011v2_tsd_14aug2015.pdf.

2014 National Emissions Inventory, version 2 Technical Support Document; U.S. Environmental Protection Agency Office of Air Quality Planning and Standards Air Quality Assessment Division Emissions Inventory and Analysis Group Research: Triangle Park, NC, 2015; https://www.epa.gov/sites/production/files/2018-07/documents/nei2014v2_tsd_05jul2018.pdf.